Politecnico di Torino

POLITECNICO DI TORINO

Master's degree in Environmental and Land Engineering – Climate Change

Academic year 2024/2025
March 2025 Graduation Session

Improving GPR data processing and interpretation on glaciers through attribute analysis

Supervisors:
Prof. Chiara Colombero
Prof. Farbod Khosro Anjom

Candidate:
Alessandra Pizzuti De Saraka

Abstract

Ground Penetrating Radar (GPR) is often used to map the internal structure of glaciers. Due to the high resistivity of ice, the signal does not undergo strong attenuation phenomena and provides a representation of the ice body in the form of a radargram where ice is mostly electromagnetic transparent.
Nevertheless, while travelling inside the glacier, the electromagnetic wave encounters several materials with different degrees of conductivity which cause the attenuation of the signal; this behavior is represented as a series of hyperbolas and scattering events more or less marked on the GPR display. However, the origin of these patterns is open to interpretation and not always obvious when analyzing the reflection amplitude alone.
In order to better investigate the nature of the facies portrayed in the radargrams, we evaluated a series of attributes, which are mostly employed in seismic investigation and GPR surveys in the archaeological domain, in glaciology: more precisely on Indren and Rutor glaciers, located in the Aosta Valley Autonomous Region, Italy.
Through the study of the results obtained from the simple GPR assessment, subsequently coupled with the attribute analysis focused on the instantaneous- and frequency-related signal properties, it was possible to better identify fractures and cavities excavated by water, a peculiar thermal effect in the proximity of the bedrock, different types of ice constituting the glacier, and other common features of the glacial exploration otherwise hardly detectable by carrying out a simple GPR survey.
This research can be beneficial in identifying potentially dangerous elements, such as fractures and cavities filled with water, forming as a result of a warming climate, threatening the “good health” of the glacier and consequently the surrounding valleys.

Index

List of figures

List of tables

1 Introduction

The scope of this present thesis work is to explore the glacial environment in the western Italian Alps through the use of attribute elements, usually applied to reflection seismic surveys, as a dedicated technique adopted to offer support and to enhance the outcomes derived from a ground penetrating radar (GPR) investigation.

A GPR scan is a geophysical methodology involving high frequency electromagnetic waves sent down into the subsoil by a transmitter antenna, which can be dragged on the surface by an operator, mounted on an airborne vehicle or carried onto drones (Unmanned aerial vehicles – UAVs). The antenna acts as a source of electromagnetic pulses and, when the signal encounters either an object or a medium with different electromagnetic properties, part of it is reflected back and "captured" by a receiver antenna, able to sample the signal, store the data, and transmit the results directly to the display of the device (or an external computer) in order to check the quality of the outcomes. What is obtained is a series of traces represented one after the other in a bidimensional matrix called *radargram*. As this radargram is not easily readable, the results are then processed with specific software or detailed algorithms implemented in Matlab or Python to increase the signal-to-noise ratio of the acquired data.
When aiming to a better comprehension of the features portrayed on the GPR image, a technique relatively new in glaciology may provide support: GPR attribute analysis. An attribute can be considered as a parameter derived from the amplitude of reflection of the GPR signal through a computation.
Attributes have been used since 1970s in reflection seismic to strengthen the assessment of studies conducted in the petroleum industry. At the beginning, attributes such as instantaneous frequency, amplitude, and phase were utilized; since then the range available has expanded to volume- and surface-based ones. Considering that GPR and seismic applications derive from the same wave theory, the attribute analysis can be applied to seismic as well as ground penetrating radar studies. (Zhao et al., 2013).
As a matter of fact, a relatively spread area of use of the aforementioned geophysical technique is archaeology. GPR attribute interpretation is employed to maximize the results obtained from GPR records and help identify cultural remains buried underground thanks to the properties characterizing the archaeological finds, which differ from the features of the surrounding environment: this variations are then reflected in the attributes behavior.

Nevertheless, the focus of this research is on the glacial domain. Recent evaluations of attribute responses applied on GPR radargrams acquired on glaciers or permafrost have been performed by several groups of scientists around the world. Successful attempts of GPR attributes interpretation have been carried out aiming to glaciers characterization, ice facies distribution, drainage network identification in ice masses, cold and warm ice detection. In the literature, it is possible to find examples in this direction written by Santin et al. (2023), Forte et al. (2021), Church et al. (2021), Forte et al. (2020), and Zhao et al. (2016).
GPR analysis in glaciology, integrated with attributes assessment, is a useful methodology to identify potentially dangerous situations related to the melting of glaciers following global warming. In point of fact, climate change in the Alpine region has left a mark in the higher number of rainfall events and wetter snowfalls (contributing in a denser snow cover), together with air temperature increase (Maggioni et al., 2009); therefore, the presence of water infiltrating in channels and crevasses in a glacier might lead to the formation of cavities at the interface with the bedrock, slowly filling up with water. If overpressure is generated, these gaps are brought to collapse causing the material to reach the surrounding valleys. Also, due to the melting process, the walls of the glacier and the bedrock may undergo a loss of tension and give rise to mass movement and avalanches. These worrying phenomena are expected to be more frequent in temperate glaciers[1] rather than in cold ice masses (Godio, 2017).
Hence, it is necessary to state that an accurate GPR analysis reinforced with the study of attributes such as instantaneous- and frequency-related ones have the power to provide useful preventive information regarding the health of a glacier.

The main objective of this thesis is therefore to improve GPR data processing and interpretation on glaciers through attribute analysis to better highlight the inner features of the ice bodies and provide valuable insight concerning the interface between frozen material and bedrock.
To comprehend the behavior of glaciers, it is essential to give an overview on the glacier system and its main characteristics as primary step, proceeding then with the description of the context surrounding the two glaciers of interest, i.e. Indren and Rutor Glaciers, both located in the Aosta Valley.

[1] glaciers where the temperature is in the proximity of 0°C, being the pressure melting point at atmospheric pressure, with the exception of a shallow superficial layer (~15 cm) where the ice is influenced by the seasonal temperature fluctuations [24].

Subsequently, we will focus on the details behind a GPR survey and the attribute analysis by offering an explanation of the main functions of the ground penetrating radar device, the theory behind it, and the different types of attributes available in the literature.
The results are then going to be presented starting from the explanation of the equipment utilized in the GPR campaigns on the two glaciers, moving on to the technical parameters connected to the survey, such as central frequencies of the antennas, number of profiles, period of acquisition, number of samples, etc. Finally, the profiles returning the most interesting results in terms of features detected are unveiled for each glacier.
It is also meaningful to draw the final conclusions regarding the analysis carried on in the present work and provide considerations concerning future perspectives of attribute computations for glacial applications.

2 Glaciers overview and site description

2.1 Introduction

The present research was conducted by analyzing GPR lines collected on two Italian glaciers, the Indren and Rutor Glaciers, respectively in July 2020 and July 2024, both located in the western section of the Alpine arch (more precisely Pennine and Graian Alps) situated inside the borders of the Aosta Valley Autonomous Region (Regione Autonoma Valle D'Aosta – RAVA). In this area, the largest glaciated region of Italy, 36,15% of the total, is located (Smiraglia et al., 2015) .

For the purpose of giving a better overview of the distribution of the Italian glaciers over the territory, the following table is proposed.

Table 1 - Distribution of the Italian glaciers (Smiraglia et al., 2015)

Region or Province	Number of glaciers	Cumulative area value (km^2)	Region contribution to the total area (percentage with respect to the whole Italian coverage)	Region contribution to the total census (percentage with respect to the total number of Italian glaciers)
PIEDMONT	107	28.92	8%	12%
AOSTA VALLEY Autonomous Region	192	133.73	36%	21%
LOMBARDY	230	87.71	24%	25%
TRENTINO (Autonomous Province of Trento)	115	30.96	8%	13%
SOUTH TYROL (Autonomous Province of Bolzano)	212	85.12	23%	23%
VENETO	38	3.23	1%	4%
FRIULI-VENEZIA GIULIA	7	0.19	0%	1%
ABRUZZO	2	0.04	0%	0%
ITALY	903	369.90	100%	100%

The U.S. Geological Survey (USGS) defines a glacier as "a large, perennial accumulation of crystalline ice, snow, rock, sediment, and often liquid water that originates on land and moves down slope under the influence of its own weight and gravity" [1].

As described by Kappenberger [2], glaciers are classified on an international level inside the World Glacier Inventory (WGI) with more than 130,000 glaciers according to parameters such as area, length, orientation, elevation, geographic location [3]. However, concerning the Alpine domain, it is more appropriate to classify the glaciers in line with the Italian inventory where they are subdivided into three main groups:

- Mountain glaciers, characterized by an accumulation zone of discrete size and no actual snout;

- Alpine or valley glaciers where the accumulation zone is of large dimensions and a prolonged terminus is visible;
- Himalayan glaciers, formed by different basins converging together in only one flow often covered by moraine debris.

In the second half of the 20th century, a large number of Alpine glaciers had the typical shape of a valley glacial mass; nowadays the majority have turned to a mountain-type of glacier [2].

The glacier system is in continuous movement with snow accumulating over the winter period and undergoing melting processes in summer. Remarkable effects of the motion of glaciers are the formation of crevasses, cracks in the ice opening due to traction forces, and the schistose aspect, related instead to compression forces. Crevasses originate in different positions and are of several types: they are *marginal* if they create on the sides, *transverse* if they form "perpendicular to direction of ice flow", *longitudinal* when crevasses are oriented along the valley (parallel to the flow), and *frontal* if located at the glacier front. Also, *seracs* can form following the crevasse formation when large blocks of ice detach (Fedele, s.d.) [4].

To better understand the behavior of a glacier, a mass balance evaluation is to be assessed. The winter period is when the highest volume of snow accumulates and becomes ice in the accumulation zone located above the equilibrium-line altitude (ELA)[2]; in summer, the ice mass undergoes processes such as melting and sublimation in the ablation area below the ELA. Therefore, the mass balance is performed by subtracting snow accumulation and ice loss over a year: a result equal to zero indicates a good health of the glacier as the ice body does not change its size and ice, together with debris, is correctly transferred from the accumulation zone to the ablation zone [5] where the sediments will then deposit to form the moraines. A variation in the mass balance is reflected in the modification of the glacier profile (Calmanti et al., 2007).

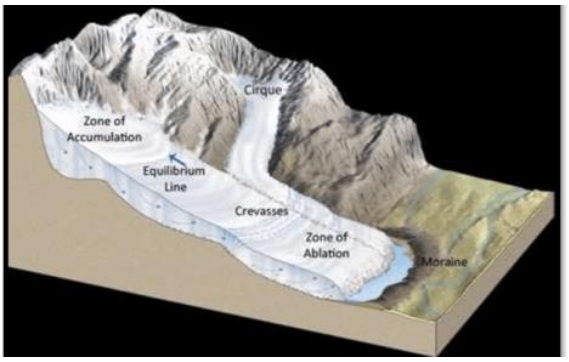

Figure 1 - Anatomy of a valley glacier [6]

[2] ELA: "marks the area or zone on a glacier separating the accumulation zone from the ablation zone and represents where annual accumulation and ablation are equal" [27].

However, as a consequence of the global rise in temperatures, images acquired by satellites since 1976 have shown a shrinkage in glacier thickness of around 14 meters [7].
As a general overview, the figures below show the loss of glacier mass over the world in 2023[3].

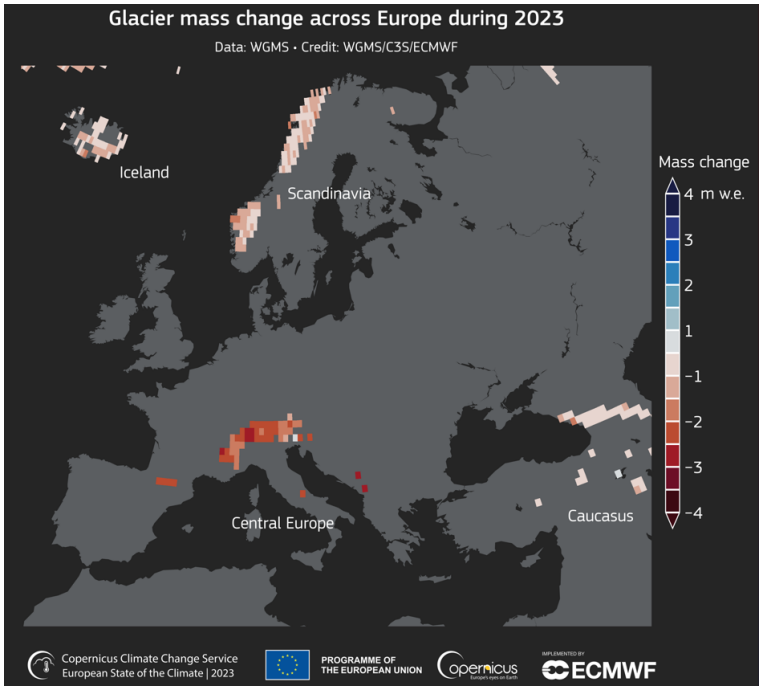

Figure 2 - Change in glacier mass over the year 2023 [8]

When observing the situation in Central Europe between 1976 and 2023, an ever-growing trend towards a reduction of the glacier areas was recorded.

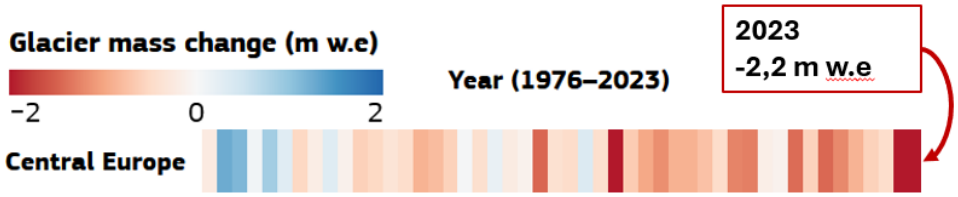

Figure 3 - Glacier mass variation between 1976 and 2023 in Central Europe. Data last updated in April 2024 [7]

Glacier retreat is a well-known aspect directly connected to climate change and global warming. In the Alps, the reduction of the ice mass is particularly severe; moreover, according to Calmanti et al. (2007), the majority of the Alpine glaciers in Piedmont and Aosta Valley considered in their research, have faced a negative fluctuation of the average terminus in the second half of the 20th century.

[3] m w.e: meters water equivalent. A certain loss of ice corresponds to a loss of the same meters of water. Positive values are related to ice gain, negative values to glacier mass loss [7]

Table 2 - Latitude, longitude, glacier length, average slope, orientation (aspect), number of sampled years, average annual terminus fluctuation and its standard deviation (Calmanti et al., 2007)

Glacier	Lat	Lon	L [m]	Slope [deg]	Asp [deg]	N	$\overline{\delta X^j}$ [m/yr]	σ^j [m/yr]
Agnello	45°08′	6°54′	900	20	45	9	−5.3	10.7
Basei	45°28′	7°07′	900	30	0	14	−1.0	1.5
Bessanese	45°18′	7°07′	2300	15	135	12	−6.1	11.8
Breuil	45°43′	6°49′	1000	25	90	9	−3.7	7.2
Chavannes	45°44′	6°49′	1300	15	90	10	−7.0	6.5
Ciamarella	45°19′	7°08′	900	18	90	13	−1.4	5.6
Ciardoney	45°31′	7°24′	1950	8	90	12	−1.3	6.9
Clapier	44°07′	7°25′	360	16	45	25	−1.0	2.7
Estellette	45°46′	6°49′	1250	24	135	6	5.5	7.4
Fond Orientale	45°28′	7°05′	2150	15	315	13	−3.9	10.5
Fourneaux	45°06′	6°50′	600	15	315	7	−1.1	14.1
Galambra	45°06′	6°52′	850	20	45	8	−4.7	10.7
Gelas	44°07′	7°23′	170	18	0	21	−0.7	2.5
Gliairetta Vaud	45°30′	7°00′	3575	9	90	6	−7.5	12.0
Grande di Verra	45°55′	7°45′	5250	18	90	26	−11.6	7.8
Indren	45°53′	7°51′	2500	21	90	14	−5.6	4.4
Lauson	45°33′	7°16′	1000	15	45	11	−3.6	3.7
Lavassey	45°29′	7°06′	1950	22	135	14	−7.6	8.1
Maledia	44°07′	7°24′	130	18	45	26	−1.5	3.2
Martellot	45°23′	7°10′	800	38	135	12	−1.8	6.8
Money	45°31′	7°20′	2600	25	45	8	−7.8	10.4
Netscho	45°49′	7°52′	300	23	315	11	−2.2	2.5
Nord Andolla	46°06′	8°03′	600	30	135	14	−4.8	7.1
Osand Sett.	46°25′	8°18′	4330	7	90	19	−4.0	7.0
Peirabroc	44°07′	7°25′	154	13	90	29	−1.2	1.8
Pera Ciaval	45°14′	7°06′	250	1	135	3	−2.2	11.6
Piode	45°54′	7°53′	2250	31	135	17	−7.9	17.8
Rocciamelone	45°12′	7°05′	1000	1	45	5	−0.4	1.8
Rutor	45°30′	7°00′	8375	6	315	23	−2.7	5.3
Sengie Setten	45°32′	7°24′	1050	32	45	6	−5.5	10.5
Soches-Tsantel	45°29′	7°04′	3500	12	45	14	−5.8	6.1
Tza de Tzan	45°59′	7°34′	5900	15	90	10	−8.4	15.8
Vaudaletta	45°31′	7°08′	400	20	315	5	−10.2	15.2

As a matter of fact, since the Little Ice Age, which ended approximately in the 19th century, it appears that various valley glaciers have undergone a general retreat [9] leading to ice and rock avalanches caused by the unloading of the glacier (and the subsequent stress relief in the bedrock), the formation of proglacial lakes, which can become a source of danger for flooding events, and the accumulation of water inside the glacier (Godio, 2017). Of particular interest is the latest aforementioned phenomenon: as described by Godio (2017), the water resulting from the melting of the glacier will flow inside the drainage network of the ice body, infiltrating downwards, moving vertically and horizontally on the bedrock. As a result of the excavation phenomena of water, the formation of cavities occurs. These cavities will then be filled with the same water resulting from ice thawing which can cause an isolated collapse of the chamber or fractures in the marginal walls of the glaciers if a substantial amount of water culminates in a pressure buildup.

Geophysical surveys, such as the application of the GPR technique, in the glacial environment are essential to monitor the condition of potentially dangerous features, such as the formation of cavities and the amount of inner

water, and to deliver useful information regarding snow and ice density and thickness, the presence of moraines, the morphology of the bedrock, and the overall motion of the glacier which results from the coexistence of basal movement and the deformation of internal ice (Church et al., 2021).
All details pertaining to the methodologies employed and further information with respect to the orientation of the lines shall be provided in the following chapters.

2.2 Glaciers of the Aosta Valley

The Aosta Valley Autonomous Region is a typically Alpine territory with mountains reaching an average altitude of 2100 m, several peaks are above 4000 m, and more than 50% of the Region has an elevation above 1500 m.
As previously mentioned, the Aosta Valley is the vastest glacierized territory in Italy with a glacier cover of around 3,4% of the regional area, acting as climate indicators [10].
The glaciers maximum expansion in volume and length took place between 1818 and 1860 as a consequence of a cold climate with abundant snow precipitations and cool summers which prevented high ablation. This glacier growth is visible through the presence of deposited moraine materials [11].
According to *Geoportale Catasto Ghiacciai* [12], the number of glaciers registered in the Region in 1975 amounted to 297, covering an area of 188 km^2, later on it decreased to 209 bodies in 2005 with 135 km^2 of surface, and down to 184 in 2012 with 120 km^2 latest registered in 2019. When looking back at more ancient times, Calmanti et al. (2007) already provided a documentation involving a number of glaciers located in Piedmont and Aosta Valley where an overall shrinkage phenomenon was observed over a period of 70 years in the 20^{th} century.
The Aosta Valley takes great advantage from the glaciers as they provide water not only for drinkable purposes, but also for hydropower production and for field irrigation. The territory is highly dependent on the presence of glaciers and their moving nature: hydrogeologic dangerous situations might arise due to the natural hazards such as avalanches and floods, together with a variable temporal and spatial distribution of water.

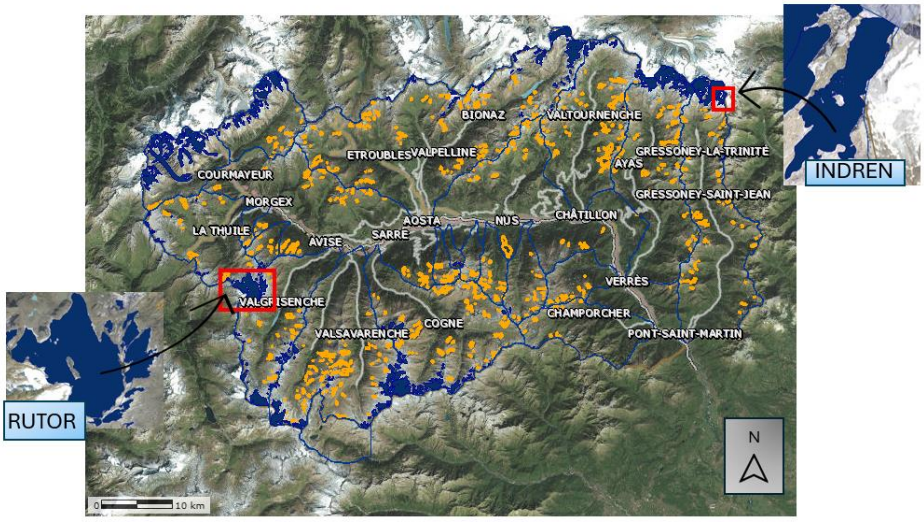

Figure 4 - Distribution of glaciers in the Aosta Valley with highlight on Indren and Rutor (topics of study in this thesis): in orange are highlighted the rock glaciers [13]

2.2.1 Site description

2.2.1.1 The Indren glacier

The Indren glacier is located in the northeastern area of the region, in the mountain sector of the Pennine Alps. More precisely, it belongs to the Lys basin in the Monte Rosa massif (coordinates in WGS84: 45,898446 N, 7,860071 E). Its highest elevation reaches 4215 m (Piramide di Vincent – EN: Vincent Pyramid) [14].

Indren is a mountain glacier with simple basin outline, facing south (Figure 6 a), with a surface of 1 km^2 (Viani et al., 2020). The slope appears to be in the range of 0 to 35°, making Indren of rather gentle gradient (Figure 6 b). It is a temperate glacier (Maggioni et al., 2009).

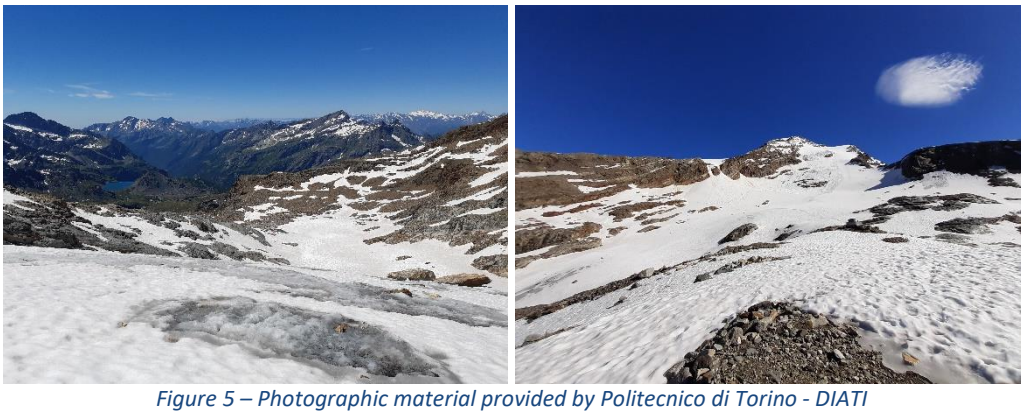

Figure 5 – Photographic material provided by Politecnico di Torino - DIATI

Indren has undergone a significant glacier retreat in the last century (about 500 m between 1927 and 2013) losing 45% of its surface (Colombo et al., 2019), resulting in the formation of hydrological systems and proglacial lakes. This

shrinking phenomenon releases plenty of nitrogen and organic carbon (CO) during the summer season, the source of which is probably linked with the industrial activities of the polluted Padana Plain (Colombo et al., 2020).
In Figure 6 c, the loss in surface is visible from the two perimeters registered around 200 years apart. For the sake of simplicity, only two periods have been selected on the portal: the first time span available covering 40 years from 1820 to 1860, and 2019 (the most recent period accessible). However, other series are present in case a more detailed perimeter fluctuation is to be assessed.
Beside snow accumulation resulting from snowfall, drifting snow and avalanches also contribute to the seasonal snowpack (Maggioni et al., 2009).

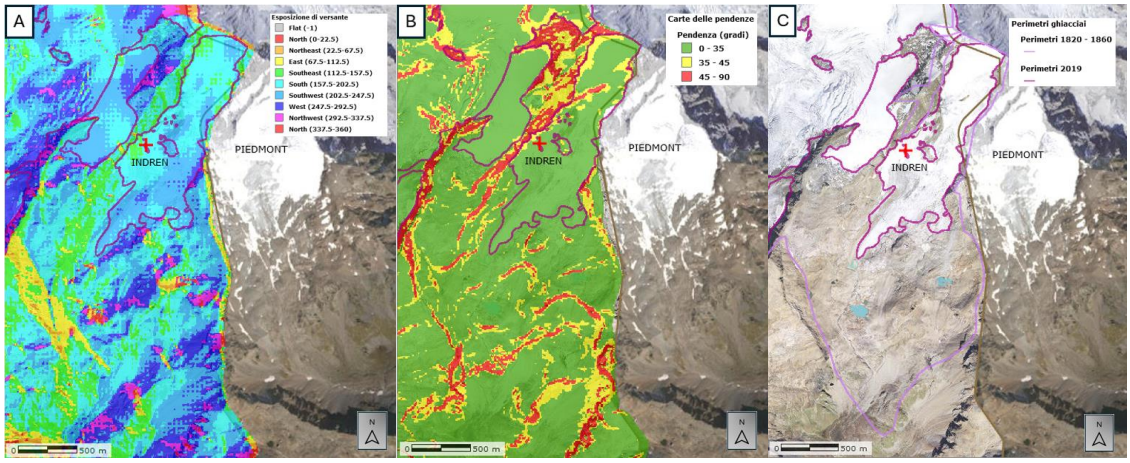

Figure 6 – Indren glacier - Maps derived from the DTM, available on Geoportale Valle d'Aosta: (a) slope exposure, (b) slope gradient, (c) perimeter decrease. The background image is for all three figures an aerial photograph dating back to 2012.

The climate in the area is characterized by wet, Mediterranean air currents coming from south/southeast and a mean annual air temperature of -2.3°C (Tognetto et al., 2021).

2.2.1.2 The Rutor glacier

The Rutor glacier is situated in the western part of the Aosta Valley (coordinates in WGS84: 45,646287 N, 7,002949 E); it belongs to the Graian Alps, and is included in the Doire de la Thuile basin.
It is still considered a valley glacier with its highest peak reaching 3486 m (Testa del Rutor – EN: Head of Rutor) [14]. Geographically, it is flanked to the northwest by Valley of La Thuile and to the southeast by Valgrisenche.
The glacier faces northwest (Figure 7 a); it is the third largest glacier (after Miage and Lys glaciers) in the Italian region by area and has a flat surface morphology (Viani et al., 2020) - Figure 7 b.
Since the Little Ice Age, where Rutor reached its maximum in extent (1820), it has undergone glacier retreat resulting in the formation of lakes inside moraine

terraces (located at an elevation spanning between 2000 and 2900 m) (Vergnano et al., 2023). The glacier maximum was 27% larger than the conditions it had in 1991 (Orombelli, 2005).

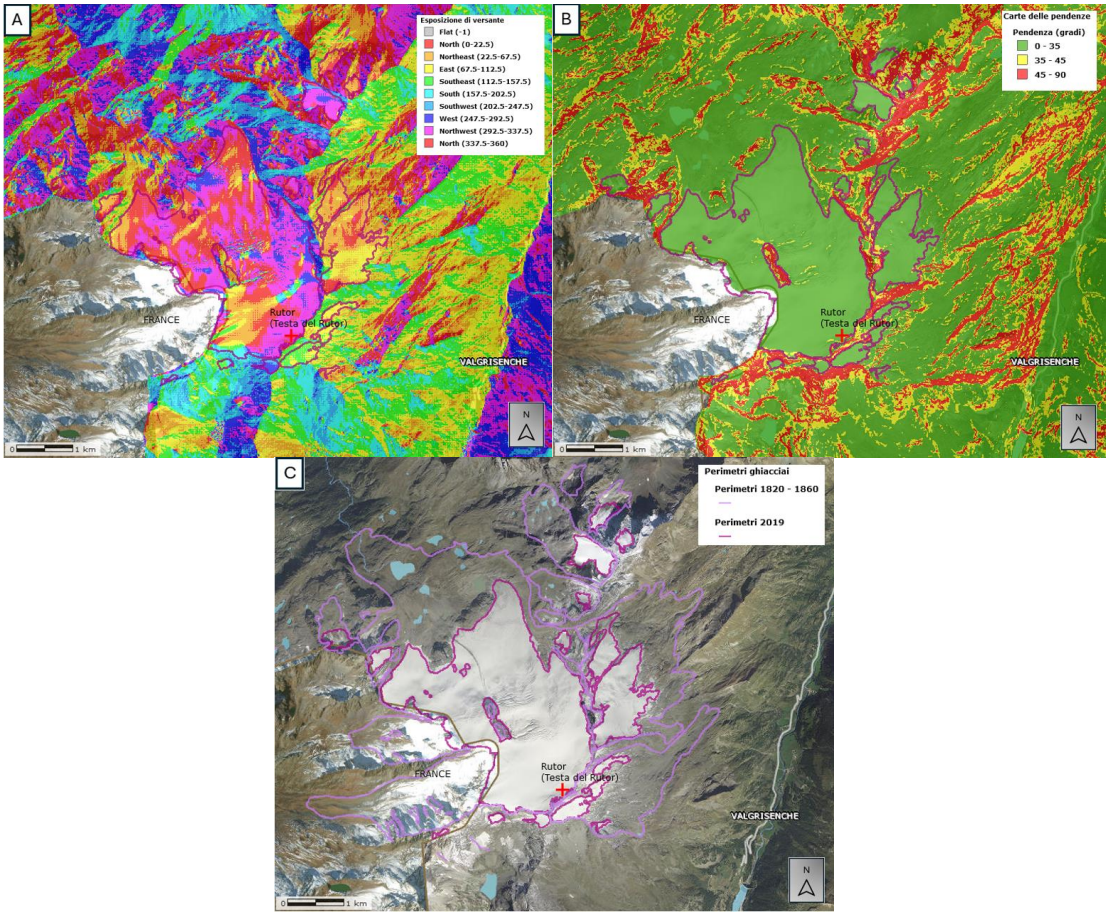

Figure 7 – Rutor glacier - Maps derived from the DTM, available on Geoportale Valle d'Aosta: (a) slope exposure, (b) slope gradient, (c) perimeter decrease. The background image is for all three figures an aerial photograph dating back to 2012.

Currently, it spans an area of about 9 km^2 but a glacier recession of 4 km^2 has been registered since 1865 (Godio & Franco, 2024) - Figure 7 c.

Figure 8 - Rutor glacier (Godio & Franco, 2024)

In 1931, the glacier tongue called Grand Assaly (south) separated from Rutor main body; in 1934, the front no longer reached Lake Seracchi and the whole glacier is now formed by six units (two located on the French territory) referred to as "Ghiacciaio Flambeau", "Ghiacciaio del Rutor", "Grand Assaly meridionale", "Grand Assaly settentrionale", "Glacier de L'Avernet", and "Glacier du Grand" [14]. Due to its "external" position, the Rutor glacier is subjected to higher snow accumulation, coming from Atlantic perturbations, compared to more "internal" glaciers. Nevertheless, its mass balance was still negative in the hydrologic year 2022-2023 [15].

As a final noteworthy consideration for the development of this work, it may be required to also evaluate the solar radiation on the two ice bodies. A glacier fully in shade might be characterized by colder ice on the surface, resulting in a more transparent response on the GPR radargram. Conversely, in case of a surface widely exposed to the solar radiation, the layer on the top is more likely to be composed by snow, possibly undergoing melting processes, thus showing high scattering in the GPR image.
In Figure 9, it is evident that both glaciers are hit by a great amount of light over the year: Indren is evidently more exposed compared to Rutor, which exhibits on the other hand several minor areas partially in shade. Despite the lower KWH/m^2 of solar radiation received by Rutor, we can assess to a good extent the strong impact of energy coming from the Sun.

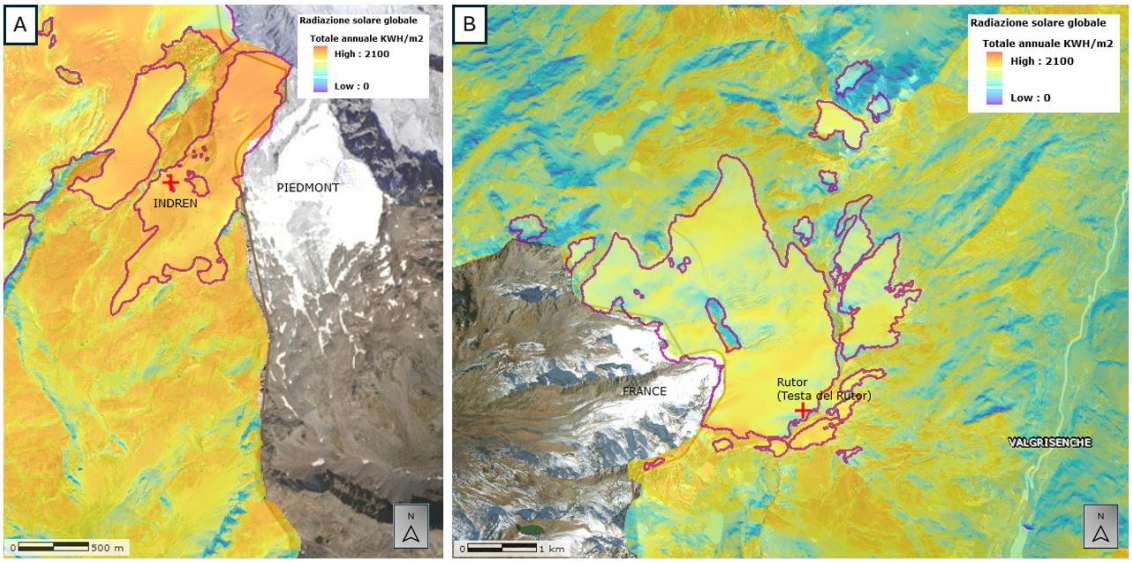

Figure 9 - Annual solar radiation on Indren (a) and Rutor (b). Maps derived from DTM, available on Geoportale Valle d'Aosta. Note the different scales. The background image is for all three figures an aerial photograph dating back to 2012.

3 Ground Penetrating Radar analysis and processing

Ground Penetrating Radar, commonly called simply GPR, is a high-resolution, non-invasive, geophysical methodology exploiting the energy reflected back by objects and structures lying underneath the ground, with the main purpose of imaging and characterizing the subsoil (Abdulrazzaq et al., 2021; Forte et al., 2021; Zhao et al., 2016). GPR is used in a widespread range of applications: starting from civil engineering, where it is capable of detecting underground facilities and different layers in pavements as well as bridge decks [16]; for military purposes to identify the presence of inexplosive devices [17]; in geology and hydrogeology to study depositional environments and groundwater characterization [18], together with the analysis of hydrocarbon reservoirs as reported by Forte et al. (2012). Moreover, ground penetrating radar has proven to be effective in revealing and mapping archaeological finds providing information related to the depth at which they are buried, the shape of the artifacts and the size (Zhao et al., 2013). Another common field of application, which is the primary objective of this thesis, is glaciology: as a matter of fact, GPR is employed to assess the thickness of ice, of the snow layer on top of the glacier, the amount of water flowing inside the body or hold in cavities, the presence of crevasses and seracs, the temperature of ice according to its transparency to the electromagnetic wave, the morphology of the bedrock, and surely the technique is used for an overall detection of the state and health of the glacier together with any possible dangerous condition (Godio, 2017). Mass balance estimations and studies on permafrost are also a feasible option. What is exploited in GPR surveys on ice bodies is the strong contrast in dielectric permittivity between frozen and unfrozen wet materials which enables the detection of the boundaries between materials with different properties and varying amounts of liquid and frozen water. In addition, GPR in glaciology takes advantage of the low conductivity characterizing ice which makes it appear on the radargram as a transparent facies. (Forte et al., 2021).

3.1 Ground Penetrating Radar: general overview

The Ground Penetrating Radar (GPR) is a device employed in underground investigation making use of high frequency electromagnetic waves (10 MHz to 1 GHz (Forte et al., 2021), although in the literature ranges spanning up to 6 GHz are mentioned (Zhao et al., 2016)).

The GPR tool consists of a transmitter and a receiver being dragged on the ground: the electromagnetic pulse is sent down in the medium; consequently, when the signal encounters a different material with different electrical

permittivity, part of the energy is reflected back and acquired by the same antenna (monostatic antennas) or a different one (bistatic antennas) (Baker et al., 2007).
What is registered are the travel-times and the amplitude of reflection of the traces (Santin et al., 2023).

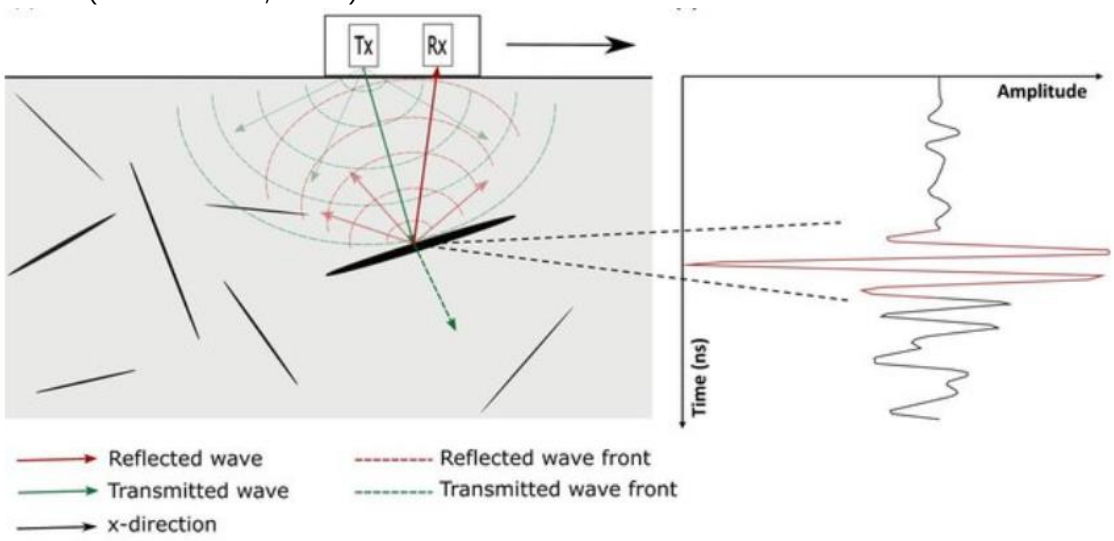

Figure 10 - Scheme of GPR configuration (Molron et al., 2020)

The antenna configurations and frequencies are multiple and the results can be obtained at different depths or scales (Zhao et al., 2016). The spacing of the antennas also plays an important role in the quality of the final results as it depends on the type of material in which the signal is travelling and dictates the distance among transmitter, receiver, and target in the subsoil: a longer trajectory travelled by the pulse of energy in a material with high attenuation leads to a non-negligible signal loss. On the other extreme, if the two antennas are too close, aliasing phenomena[4] may occur (Baker et al., 2007). In case of GPR surveys carried out on the snow, the typical offset between the two antennas is set to 6 cm [19].
Despite the majority of GPR surveys being performed as described above, the possibility of mounting GPR systems on aerial platforms is also an option, providing in this case a more rapid solution for glacier monitoring (Forte et al., 2021) and overcoming site accessibility problems. However, concerning airborne GPR surveying, it must be taken into account that several drawbacks are present: the electromagnetic signal is attenuated in air (the further from the surface, the higher the attenuation), investigation depths and resolution reduce, the vehicle produces noise in the data acquired. A valid solution to

[4] Aliasing phenomenon: it occurs when two different analog signals become indiscernible once sampled and it is due to the fact that when sampling an analog signal to obtain a digital one, if the sampling period is too wide, several signals might correspond to that sampling when returning back to the continuous signal.

mitigate these drawbacks are Unmanned Aerial Vehicles (UAVs), such as drones, which fly at lower altitudes.
The GPR technique is fast for data acquisition and processing (Zhao et al., 2016), non-invasive and results in a high resolution subsurface imaging (Forte et al., 2021) even though the level of resolution and the penetration depth are dependent on the tradeoff between conductivity of the medium crossed by the electromagnetic wave and frequency of the antenna. In fact, materials such as highly conductive water (with dissolved salts), will limit the propagation of the signal travelling downwards in the ground [20]. On the other hand, frozen materials (ice, firn, permafrost) exhibit low electrical conductivity (and high resistivity), enabling the signal to travel deeper due to the low attenuation (Forte et al., 2021). Moreover, higher frequencies of the antenna lead to higher resolution, decreasing however in penetration depth. In fact, the central frequency determines the resolution as it depends on the wavelength of the electromagnetic wave: frequency and wavelength are inversely proportional leading to a better vertical resolution in case of higher frequency and lower λ. Therefore, the accepted vertical resolution is often considered as one quarter of the wavelength (Baker et al., 2007). It is necessary to choose the optimum operating frequency according to the site characteristics.

3.2 Methodology

For the purpose of this research, the Matlab environment was employed to process the GPR datasets collected on the two glaciers.
As already mentioned in the previous paragraph, the equipment registers traces of reflection amplitude which are function of time. In order to better understand the mode of operation of a GPR survey, it is necessary to specify the two important acquisition parameters to take into consideration: length of the recording, i.e. the total time needed to record the traces, and the sampling in space, that is how many traces the operator plans to acquire along the profile. The former is evaluated according to the two-way travel time (TWT), i.e. the time taken by the signal to travel down and then come up to the receiver, through the following formula:

$$\mathrm{TWT} = \frac{2 \cdot \mathrm{z}}{\mathrm{v}} \quad (3.1)$$

Where z is the depth of the target, and v is the velocity of the electromagnetic wave travelling through the ice layers and is computed as follows:

$$v = \frac{c}{\sqrt{\varepsilon_r}} \quad (3.2)$$

With c equal to the velocity of the electromagnetic wave in the free space ($3 \cdot 10^8$m/s), and ε_r is the relative electrical permittivity of the material (also known as dielectric constant, the ratio of the permittivity of the material and the permittivity of vacuum).
The latter (the sampling in space) is linked to the Shannon-Nyquist sampling theorem whereby the distance between subsequent traces Δx is related to the dominant wavelength λ according to the following equation:

$$\Delta x \leq \frac{\lambda}{2} = \frac{c}{2 \cdot f_{max} \cdot \sqrt{\varepsilon_r}} \quad (3.3)$$

Note that the maximum frequency f_{max} is higher than the antenna central frequency f_c by 1.5 times.
Concerning the sampling rate, i.e. the distance between one sample and following one in the GPR trace (how many samples we want to take in time), the Shannon sampling theorem is applied:

$$\Delta t \leq \frac{1}{6 \cdot f_{max}} \quad (3.4)$$

to improve the resolution and to avoid aliasing phenomena.

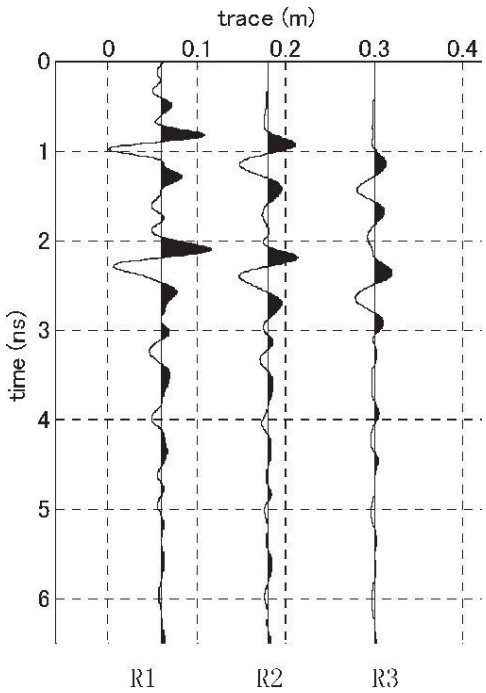

Figure 11 – Set of traces in a GPR profile (Feng et al., 2009)

Once having set length of recording, sampling in space, and sampling rate, the radargram is computed by the software. It is possible to transform the time on the y-axis to depth (depth conversion):

$$z = \frac{TWT \cdot v}{2} \quad (3.5)$$

In this study carried out on glaciers, the value of permittivity is that related to ice $\varepsilon_{r,ice}$ ranging between 3 and 4, considered equal to 3.2: with such value, the velocity results equal to 17 m/ns, which is indeed the typical velocity for pure ice even if local variations are present, especially when caused by free water (Forte et al., 2021).

Table 3 - Electrical permittivities and related EM velocities for different media of the glacial environment

	ε_r [-]	v [m/ns]
Air	1	0.30
Ice	3.2	0.17
Freshwater	80	0.03
Dry sediments	3÷5	0.1÷0.15
Wet sediments	20÷30	0.05÷0.07
Bedrock	4÷8	0.12÷0.15

It is important to mention that by increasing the permittivity of the material, the velocity of propagation of the electromagnetic wave decreases as in formula (3.2); besides, when the water content rises, the permittivity of the material follows relationship (3.6) from G.C. Topp et al. (1980) and written similarly as reported in Tabbagh et al.(2013)[5]:

$$\varepsilon_r = a + b \cdot \theta_v + c \cdot \theta_v^2 - d \cdot \theta_v^3 \quad (3.6)$$

θ_v = volumetric water content

a, b, c, and d (respectively equal to 3.03, 9.3, 146, and 76.7) are constant coefficients accounting for experimental measurements on soils with a different water content. More precisely, 3.03 is relative to the permittivity of the dry soil.

Therefore, the behavior of the relative permittivity follows the curve reported in Figure 12: by increasing the water content, the permittivity will raise as well, in contrast to the behavior of the velocity of propagation of the EM radiation.

[5] (Tabbagh et al., 2013; Topp et al., 1980)

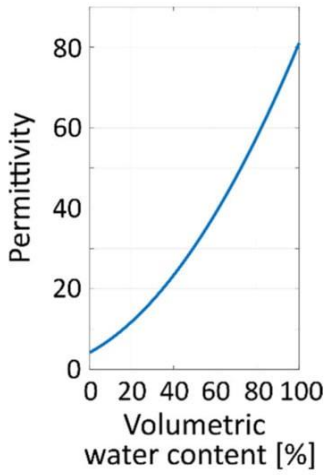

Figure 12 - Relationship among electrical permittivity, water content (Fediuk et al., 2022)

As already stated, on glaciers, the investigation depth is strictly influenced on the propagation of the electromagnetic wave in the ice body and depends on the level of heterogeneities and discontinuities inside the medium. What we expect to see in the radargram are a series of scattering phenomena related to the roughness of the ground, crevasses, and seracs inside the glacier which increase the difficulty of setting apart the interface between bedrock and ice body. Also, energy attenuation is caused by the reflection at the separation surface between snow and air.

3.3 Data processing and filtering

From the raw data we moved to the final radargram by performing a processing sequence including several steps which aim at refining the image and the signal-to-noise ratio (Forte et al., 2021):

1. Move start time → the delay of the first reflection is removed so that the air-ground interface is located at time equal to zero;
2. Background removal → the constant events (horizontal stripes) are removed by subtracting the average trace;
3. Stationary traces removal → all horizontal traces at the beginning and end of the radargram, due to the operator standing still, are removed;
4. Band-pass filter → all low and high frequencies not centered around the central frequency of the antenna are removed (low and high frequency noise is removed);
5. Geometrical spreading recovery → correction of the traces to address the problem of amplitude attenuation with depth;

6. Stationary traces removal → this time all stationary traces inside the radargram, due to the irregular dragging of the device on the surface, are removed;
7. Time cut → the longest times, providing no information, are cut.

4 Attribute analysis

The GPR attribute analysis is implemented in order to obtain a better display of the internal features of the glaciers, to assess what material is able to originate scattering phenomena (Forte et al., 2021), to improve boundaries imaging, to visualize hidden features (Santin et al., 2023), to maximize radar traces among others (Zhao et al., 2013).
The attributes coupled with classic GPR surveys share the same approach of seismic attributes (Forte et al., 2021) enhancing certain features linked to phase continuity or frequency content (Santin et al., 2023).
Despite being GPR attribute analysis already established in fields such as archaeology (Zhao et al., 2013) and hydrocarbon reservoir investigation (Forte et al., 2012), the integration of this methodology is still relative new in glaciology. Nevertheless, several cases have been proven efficient in identifying varying features such as debris within the glacier material, warm and cold ice zones having a different amount of water and heat regime (Gutgesell & Forte, 2024).
In the literature, attributes are grouped according to different approaches: Forte et al. (2012) classifies the GPR attributes in appendix A as instantaneous, amplitude-, frequency-, coherency-, and texture-related attributes. Other existing subdivisions are performed based on time, phase, amplitude, and frequency [21], or are related to physical features (physical attributes directly connected to wave propagation, lithology) subsequently divided into sub-classes grouped further into instantaneous and wavelet attributes, and geometrical properties such as dip attributes (Subrahmanyam & Rao, s.d.).
In this study, we are going to adhere to Forte's classification and add an overview of several other examples of possible GPR attributes with their features.

4.1 Instantaneous attributes

Instantaneous attributes derive from the complex signal theory (Zhao et al., 2013); as reported in Forte et al. (2012), where the appendix gives a clear overview of the most relevant GPR attributes families, they are quantified for each trace and computed through the Hilbert transform. They have been employed in several fields of application, glaciology included, since the 1970s.
The two main instantaneous attributes are instantaneous amplitude (also known as trace envelope) and instantaneous phase.

4.1.1 Instantaneous amplitude

This attribute, also known as reflection strength or signal envelope for the sake of this research, has origin from the GPR signal which is a complex function

where the imaginary part y(t) is derived from the real one through the Hilbert transform. Therefore, from a complex signal such as:

$$A(t)e^{j\varphi(t)} \quad (4.1)$$

A(t) is the instantaneous amplitude (Zhao et al., 2013), computed as:

$$A(t) = \sqrt{x^2(t) + y^2(t)} \quad (4.2)$$

being x(t) the real part (Forte et al., 2012).
As the name suggests, it is sensitive to the amplitude and it is never negative (Forte et al., 2012). Moreover, it is the amplitude envelope of the GPR trace, calculated sample by sample to give information about the acoustic impedance contrast, i.e. reflectivity, between strata showing instantaneous amplitude variations possibly linked with boundaries, different depositional environments, changes in lithology, and unconformities (Subrahmanyam & Rao, s.d.; Zhao et al., 2013).

4.1.2 Time derivative of instantaneous amplitude

The time derivative of instantaneous amplitude is often computed thanks to its ability to improve the resolution, making the whole image easier to interpret, and to detect rapid amplitude variations which lead to accentuated sharp interfaces, discontinuities, and reflections, with scattering phenomena (potentially given by pebbles and rocks) resulting more evident (Forte et al., 2012; Subrahmanyam & Rao, s.d.; Zhao et al., 2016).

$$A' = \frac{dA(t)}{dt} \quad (4.3)$$

As the name suggests, it originates from the instantaneous amplitude.

4.1.3 Instantaneous phase

Often classified also as a phase-related attribute, as reported by Abdulrazzaq et al. (2021), the instantaneous phase is "the orientation angle of the amplitude vector at a particular time and relates to the propagation phase of the seismic wavefront", being the wave front a line of constant phase.
Starting from the complex signal reported in (4.1), φ(t) is the instantaneous phase, obtained as:

$$\varphi(t) = arctan\frac{y(t)}{x(t)} \quad (4.4)$$

The instantaneous phase is sensitive mostly to phase and to a lesser extent to bandwidth as well. It gives the propagation phase of the wavefronts (Forte et al., 2012).
It is independent of the amplitude of the signal (Gutgesell & Forte, 2024).
The instantaneous phase is measured in degrees and ranges from -π to + π; it describes the geometry, it displays discontinuities, however not in the best way possible, faults, sequence boundaries, it shows lateral continuity better, and it can be employed for bedding visualization. If this attribute is characterized by the continuity of the phase, the properties of the material through which the electromagnetic wave is traveling are homogeneous and isotropic (Abdulrazzaq et al., 2021; Subrahmanyam & Rao, s.d.).
From the instantaneous phase, other attributes are derived, such as its cosine and instantaneous frequency.

4.1.4 Cosine of instantaneous phase

Unlike instantaneous phase, the cosine does not show any +/- 180° discontinuity, contributing in making it smooth. The data produced can be further processed and what is highlighted by this attribute is the spatial continuity of the events, also accentuating lateral discontinuities of the reflectors (Forte et al., 2012; Zhao et al., 2013).
Same as instantaneous phase, it provides a decent visualization of the bedding (Subrahmanyam and Rao, s.d.).

4.1.5 Instantaneous frequency

The instantaneous frequency is a seismic attributes which can be exploited in GPR surveys as well; in signaling theory, it makes reference to the frequency of a monocomponent signal at a specific time [22]. It is defined as the first derivative of the phase with respect to time, i.e. the time rate of change of the phase [23] and expresses the seismic wavelet amplitude spectrum mean frequency (Subrahmanyam and Rao, s.d.).

$$IF = \omega(t) = \frac{1}{2\pi}\frac{d\varphi(t)}{dt} \quad (4.5)$$

The instantaneous frequency is affected by the bandwidth of the signal and the dominant component of the spectral content is marked out by this attribute for each time sample (Forte et al., 2012).
In the literature, it is also common to find the instantaneous frequency described among the frequency related attributes (Gutgesell & Forte, 2024).
It is able to provide information about the presence of hydrocarbons by showing a low frequency anomaly, the thickness of the bedding where higher

frequencies highlight sharp interfaces, and other parameters such as the sand/shale ratio (Subrahmanyam and Rao, s.d.).

4.1.6 Instantaneous bandwidth

According to the literature, there are multiple ways to calculate this attribute: it can either be obtained by the module of the first time derivative of the instantaneous frequency

$$IB = \left|\frac{d\omega(t)}{dt}\right| \quad (4.6)$$

or by computing the rate of change of the instantaneous amplitude as absolute value of the ratio between the first derivative of the instantaneous amplitude and the instantaneous amplitude itself (Barnes 1993; Cohen and Lee 1990)

$$IB = \left|\frac{A'(t)}{A(t)}\right| \quad (4.7)$$

According to Barnes (1993), another form of equation 4.7 is

$$IB = \left[\frac{1}{2\pi}\frac{A'(t)}{A(t)}\right]^2 \quad (4.8)$$

In both cases, the radargrams portray the same behavior.
The instantaneous bandwidth is employed in seismic and GPR surveys because it is capable of providing a good representation of the bed and acts sample by sample to return data bandwidth (Subrahmanyam and Rao, s.d.).
Same as the dominant frequency, this attribute returns lower values in the presence of conductive materials such as water. As a matter of fact, the instantaneous bandwidth can also be grouped into the frequency-related attributes.

4.2 Frequency-related attributes

As the time of recording increases, the high frequency content of the GPR dataset is characterized by a decreasing trend in response to the low-pass filtering effect of the media in the subsurface: the higher the conductivity of the materials, the stronger the attenuation. Therefore, it is possible to exploit the frequency variations depending on time and depth to assess the changes in the electrical properties of the materials under investigation; as a matter of fact, this applies especially in the glacier domain where the main cause for the

spectral shifting effect is linked to the change of state of ice turning into water: the presence of water leads to higher loss (Gutgesell & Forte, 2024; Zhao et al., 2016).
These variations in the frequency content are evaluated along one trace, among traces belonging to the same 2D profile or for a data volume and, to obtain frequency-related attributes, the short-time Fourier transform or wavelet analysis are used (Forte et al., 2012).
One of the most popular frequency-related attribute is the dominant frequency.

4.2.1 Dominant frequency

As reported in Zhao et al. (2013), the dominant frequency is the frequency with the highest amplitude within a specified time window; in other words, it is the frequency where the majority of the energy is concentrated.
The amount of water in the different layers of materials will lead to a quick frequency change always assessed along one trace, among traces of the same profile or in a volume. Also, the different types of materials and the thickness of the layers in the investigated area result in a gradual variation of frequency (Zhao et al., 2013).
To compute the dominant frequency several steps are followed: after having set the sampling frequency and the window size, a portion of the traces related to the window chosen is extracted; subsequently, the Fourier transform of the segment is calculated to obtain the signal spectrum of that window and, considering that the spectrum has a symmetric shape, only half of it is used. At this point the dominant frequency is identified.
According to the literature, one way to describe the dominant frequency is that reported in Barnes (1993) relating the attribute to the "square root of the second moment of the power spectrum".
Same as the instantaneous bandwidth, the values of frequency shrink in correspondence of water-filled materials or zones.

4.3 Amplitude-related attributes

As explained inside appendix A of Forte et al. (2012), from the original trace amplitude values it is possible to obtain a few attributes, among which root mean square amplitude RMS and energy can be listed. Also, the amplitude range oscillates in an approximately symmetrical way around the zero value.
Amplitude-related attributes have the ability to help detect the variation of the frozen material in the subsurface (Zhao et al., 2016).
It is important to mention that instantaneous amplitude and its derivative are often interpreted as amplitude-related attributes: as a matter of fact, in the

following chapters they are going to be essential in identifying the presence of pure ice and water.

4.3.1 RMS amplitude

It is calculated as follows and gives information about the changes in the electromagnetic impedance among the below-ground layers. The variation in permittivity of the materials leads to high electromagnetic impedance contrast which provides in turn higher value of RMS amplitude (Abdulrazzaq et al., 2021).

$$RMS = \sqrt{\frac{a_1^2 + a_2^2 + \cdots + a_n^2}{n}} \quad (4.9)$$

The amplitude value is represented by the letter a and n is the number of samples within a time interval; the number of samples defines what is the specified window chosen to compute this attribute.

4.3.2 Energy

$$E(n) = \frac{\sum_i^n a_i^2}{n} \quad (4.10)$$

The energy is calculated for a generic trace and once again a is the amplitude and n is the number of samples.
This attribute can only be positive, same as the instantaneous amplitude, and is often employed to highlight irregular amplitude reflections (Forte et al., 2012).

4.4 Composite attributes - Sweetness

Sweetness is a composite attribute because it combines instantaneous amplitude and instantaneous frequency, as the formula portrays (Abdulrazzaq et al., 2021):

$$Sweetness = \frac{A}{\sqrt{IF}} \quad (4.11)$$

It provides essential information for channels and boundaries detection in areas with materials characterized by different physical features and high electromagnetic impedance contrast, i.e. high amplitude in the radargram. The values of sweetness are higher in case of water percolation than for the ice-

bedrock contact; also, in the literature it is stated that with dead ice[6], the values of sweetness tend to rise due to the different composition compared to the surrounding materials. (Forte et al., 2021; Santin et al., 2023)

4.5 Other attributes

Into this category we have grouped textural and coherency attributes in order to give the reader a rapid overview of their features without going into details, considering they were not applied in this study, but might be useful for future tests and applications.

4.5.1 Texture attributes

Textural attributes aim at quantifying mutually related elements according to their texture, such as shape, pattern, continuity, connection. They are the representation of the statistical relationship among data using windows, centered on each individual sample, which are to be designed based on the global scale of textures detected in the dataset (Forte et al., 2012; Gutgesell & Forte, 2024).
Examples of texture attributes are entropy, contrast, and homogeneity attributes.

4.5.2 Coherency attributes

Once again, Forte et al. (2012) gives us a clear understanding of what this group of attributes consists in.
In order to discriminate lateral discontinuities, low coherence values, estimated through normalized cross-correlation, are those coming to help.
The patterns employed in the coherency analysis are of several kinds, such as diagonal, inline, crossline traces, etc., and the higher the number of traces, the more stable the results at the expense of the level of detail of the analysis.
A fixed window or a coherency cube can be used to estimate these attributes and the parameters to consider for lateral coherency are amplitude-, phase-, bandwidth-, or waveform-related.

The most common attributes working best and widely employed in glaciology are instantaneous amplitude, cosine of instantaneous phase, instantaneous bandwidth, dominant frequency, and sweetness. In the literature, other attributes such as energy play some role in the study of internal features of glaciers; however, we focused on those aforementioned, as well as the time derivative of instantaneous amplitude for a better highlight of the bedrock in certain profiles.

[6] Dead ice: portion of a glacier no longer flowing [25].

5 Results

As previously mentioned, several attributes were considered in this study with the main purpose of better understanding the internal facies of glaciers and to detect interfaces between different materials. In fact, we started from the reflection amplitude radargrams, obtained after processing the GPR datasets, and we moved on to the implementation of codes to evaluate the attributes of interest for the purpose of applying them on the processed data and extract the new matrices, one for each attribute analyzed.

Therefore, for GPR attribute analysis it is important to evaluate the 2D radargrams obtained after the computation in the Matlab environment.

In all matrices of traces, scattering phenomena are clearly visible and related either to the water content or to the amount of debris inside the ice, as well as the frequency of the antenna, as stated by Björnsson et al. (1996) and Pettersson (2005)[7]. To give an example, in the previous chapters the high conductivity of water was addressed, presenting it as a feature causing a disturbing effect in the signal, portrayed on the GPR section as a remarkable scattering and accompanied by a decrease in the high frequency components (this behavior is to be noticed in the dominant frequency attribute) (Forte et al., 2020). A similar trend should be highlighted by the instantaneous bandwidth, whereas the composite attribute of sweetness is more likely to present higher values relative to areas with water percolation. Also, the presence of water is characterized by a strong amplitude increase in the reflection between two materials when one is filled with unfrozen water (Forte et al., 2021).

Other types of attributes, such as the cosine of the instantaneous phase, will show a more chaotic trend at the interface ice-bedrock.

In the following table, several features of a number of GPR facies related to the glacial environment are shown, together with their response in the attribute analysis related to dominant frequency (DF), cosine of instantaneous phase (PH), and sweetness (SW).

[7] (Björnsson et al., 1996; Pettersson, 2005)

Table 4 - Characteristics of GPR facies according to the reflection amplitude, scattering, layering, and attribute signature (Santin et al., 2023)

GPR FACIES	*REFLECTION AMPLITUDE*	*SCATTERING*	*LAYERING*	*Attributes signature*
Clean ice	Very low (transparent)	No (or very localized)	No, except for shear zones	High DF; discontinuous PH; low SW
Dirty ice	Medium and discontinuous	Moderate	Local, quite continuous	Medium DF; locally continuous PH; medium SW
Basal debris with ice	High	Variable	Low to absent	Medium to low DF; locally continuous PH; high SW
Dead ice	High	High, locally variable	Only local	Medium DF; locally continuous PH; highest SW

The next paragraphs will explain the different features detected by each attribute evaluated on the Indren glacier firstly and on the Rutor glacier afterwards.

5.1 Equipment employed and period of acquisition

The datasets analyzed in this research were collected during two campaigns on the two glaciers in June 2020 (Indren) and July 2024 (Rutor).

Table 5 - Indren and Rutor survey characteristics

	Indren	Rutor
Antenna central freq. f_c	200 MHz	200 MHz
Maximum freq. f_{max}	300 MHz	300 MHz
Sampling rate Δt	0.56 ns	0.56 ns

On both glaciers the device was dragged on the surface mostly covered by snow (snow cover > 3 m on some areas of the Rutor Glacier).

Figure 13 - GPR device (Indren glacier). Photographic material provided by Politecnico di Torino - DIATI

5.1.1 Indren Glacier

The geophysical survey was conducted on the glacier on July, 9 2020 operating a 200 MHz antenna and recording data along 12 profiles oriented according to Figure 14.

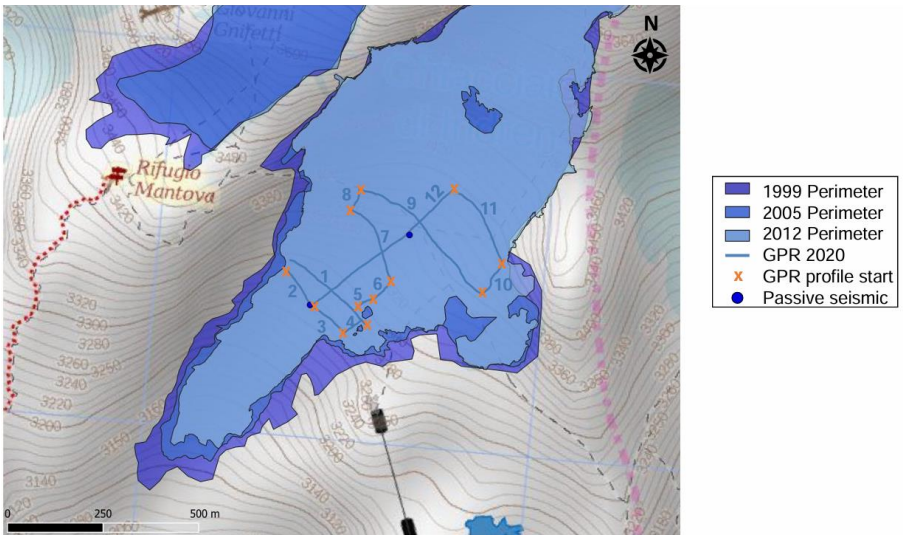

Figure 14 - Perimeters of Indren in 1999, 2005, and 2012 along with GPR profiles

For purely informational purposes, it should be noted that passive seismic measurements were also integral part of the survey despite not being addressed in this study.
Below are some key parameters for the survey.

Table 6 - GPR acquisition parameters (Indren Glacier, June 2020)

Profile denomination	N° of traces	Acquisition window [ns]	Samples
Profile 1	33265	800	2048
Profile 2	11032	800	2048
Profile 3	12459	800	2048
Profile 4	10455	800	2048
Profile 5	14005	800	2048
Profile 6	15594	800	2048
Profile 7	26231	800	2048
Profile 8	11719	800	2048
Profile 9	37211	800	2048
Profile 10	25726	800	2048
Profile 11	20771	800	2048
Profile 12	39654	800	2048

Only seven lines[8] out of twelve are going to be analyzed in the following paragraphs because they resulted more representative of the purpose of this research, i.e. the improvement of GPR processing through attribute analysis. In particular, the focus will be on lines 1, 2 and 3, 9, 10, 11, and 12.
Once processed, other profiles such as n° 4, 5, and 6 were characterized by noise, small depth of investigation, and little information for us to further investigate.

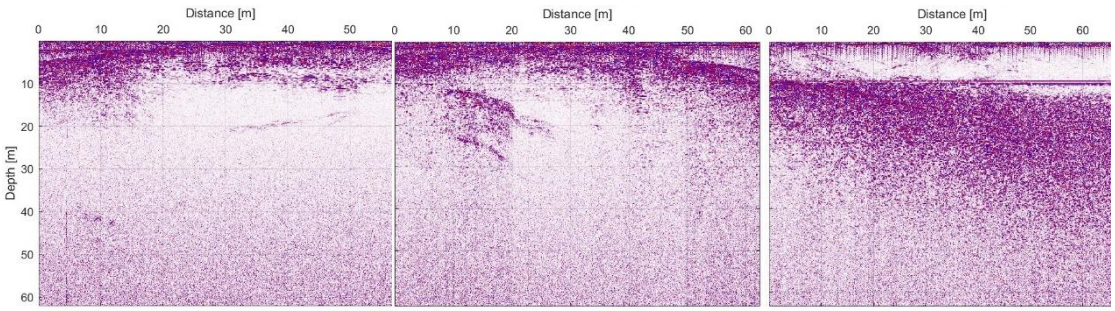

Figure 15 – Processed profiles 4,5,6 (reflection amplitude)

A few hyperbolas are visible in line 6 in the ice just below the surface, probably due to crevasses, and part of the bottom is slightly noticeable between 5 and 6. Nevertheless, it is not possible to understand what occurs below 20 m.
A more interesting profile despite the shallow depth is number 10, which is going to be described in details further on in chapter 5.

5.1.2 Rutor Glacier

Two different GPR antennas were used to carry out the survey (July 2024): a 200-MHz antenna for a higher resolution but shallower investigation and a 40-MHz antenna for a deeper characterization with lower resolution. However, the processed radargrams acquired with the 40-MHz antenna did not return any notable outcome and have therefore been neglected.
The GPR traces were georeferenced with a GPS receiver (Ublox EVK-7) placed on the GPR antenna and synchronized with the GPR control unit.
Six profiles of the 200 MHz antenna survey were processed; their orientation is reported Figure 16.

[8] It should be noted that the terms *line* and *profile* are used as synonym in this study.

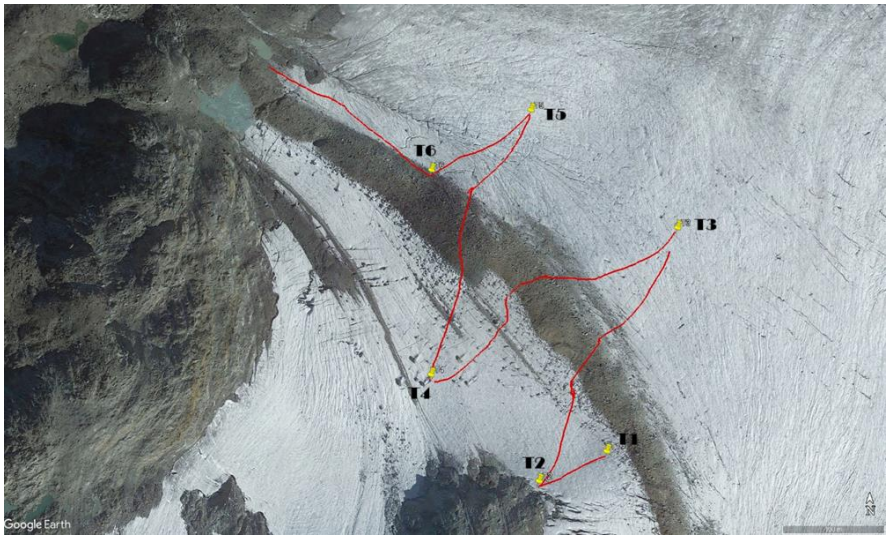

Figure 16 - GPR traces profiles (200 MHz). Symbols T1 to T6 identify the starting point for every line (Godio & Franco, 2024)

Table 7 - GPR acquisition parameters (Rutor, July 2024) with 200 MHz antenna (Godio & Franco, 2024)

Profile denomination	N° of traces	Acquisition window [ns]	Samples
Rut_24_Lid_1_200	805	700	1196
Rut_24_Lid_2_200	3673	700	1196
Rut_24_Lid_3_200	3920	1200	1435
Rut_24_Lid_4_200	3296	1200	1435
Rut_24_Lid_5_200	939	1200	1435
Rut_24_Lid_6_200	1884	1200	1435

All lines have been analyzed trying different attributes.

5.2 Attribute analysis results – Indren Glacier

The 12 profiles recorded on the Indren glacier follow the orientation reported in Figure 17, which integrates the aerial photography in Figure 14.

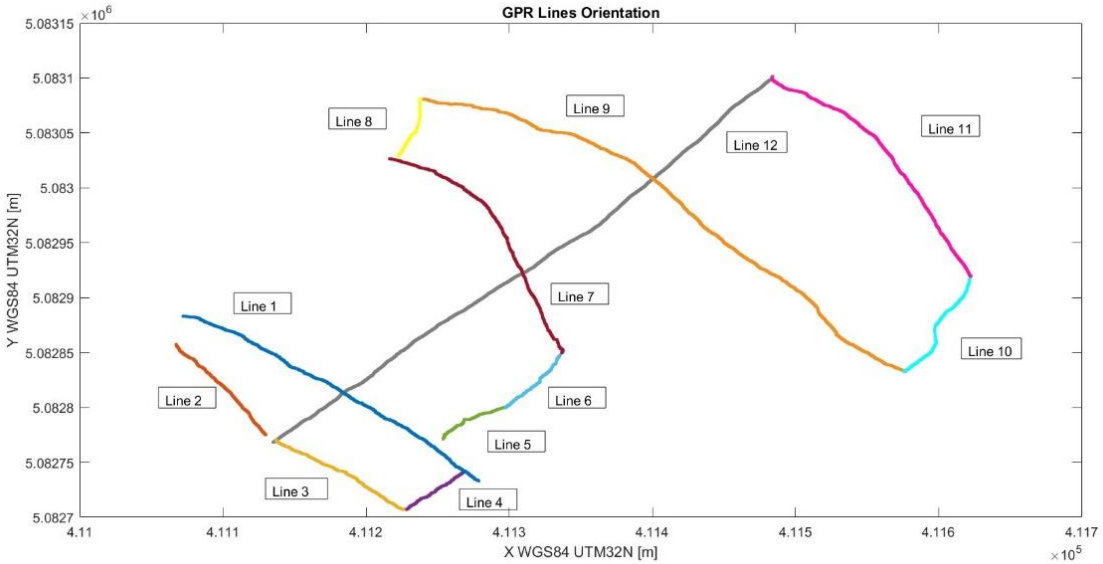

Figure 17 - Indren GPR profiles orientation

As previously declared in paragraph 5.1.1, we focused on the results obtained for lines 1, 2 and 3, 9, 10, 11, 12.

Table 8 - Orientation of Indren profiles

Profile	Orientation
1	Southeast- Northwest
2 and 3	Southeast- Northwest
9	Southeast- Northwest
10	Southwest-Northeast
11	Southeast- Northwest
12	Southwest-Northeast

For all Indren profiles, the attributes providing significant information are cosine of instantaneous phase here coupled with the instantaneous amplitude for a better understanding of the signal characteristics, instantaneous bandwidth, dominant frequency in some cases, and the composite attribute of sweetness. Moreover, the time derivative of instantaneous amplitude was included for a better delineation of the glacier bed.

Therefore, after an overview of the main features already highlighted by the reflection amplitude section, the study will proceed on the attribute analysis.

5.2.1 Profile 1

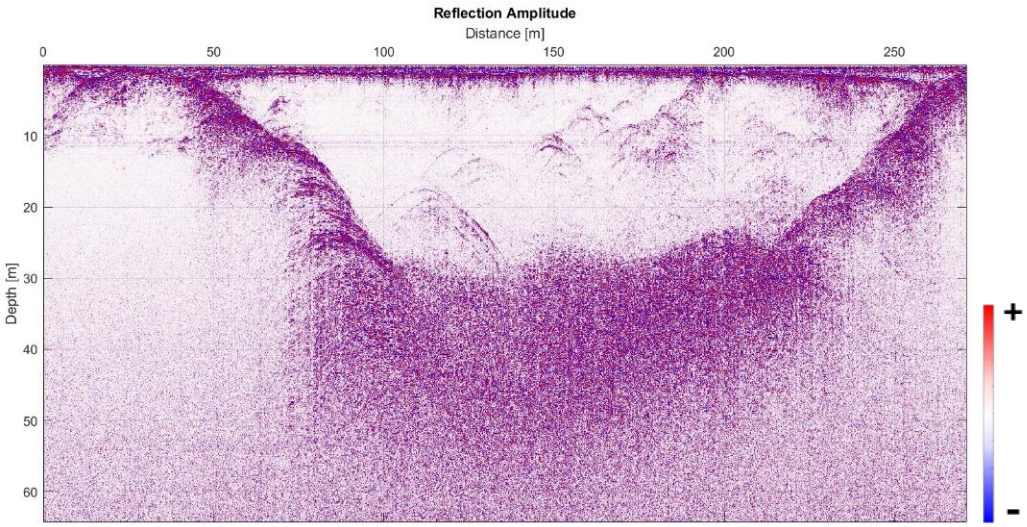

Figure 18 – Reflection amplitude - Profile 1 (Indren)

Profile 1 is characterized by an evident scattering at the top of the radargram, most likely related to the wet snow cover. The higher the scattering, the larger the amount of liquid water inside; therefore, the wet snow pack is a good hypothesis to justify the disturbance on top of the image and it will be verified through the attribute analysis.

As a matter of fact, following the raise in temperatures, the snow cover becomes wetter and its density increases (Maggioni et al., 2009). Moreover, the solar radiation of the summer period will likely contribute to the fusion of the top layer.

Being Indren a temperate and "wet-based" glacier (Colombo et al., 2019), a certain amount of free water is expected to be identified, justifying the attenuation of the electromagnetic wave, translated into a disturbed pattern in the display.

Further diffuse scattering is visible on the left side and on the right side of the GPR section: the bedrock with its pebbles, sediments, and debris lead to high values of reflection amplitude and appear particularly evident at the beginning and at the end of the line, with a rather steep slope after 30 m distance.

Several diffraction hyperbolas are noticed starting from the top, down to a depth of 30 m: they might indicate the presence of crevasses, where water manages to infiltrate contributing in a loss of the signal, cavities full of air, cavities full of water or hyperbolas given by the presence of rocks and pebbles.

Finally, at the bottom of the image, the signal was strongly attenuated close to the bedrock, depriving of a smooth delineation of the full underlying rock.

The attributes interpretation is going to provide more information to help assess the nature of the glacier features.

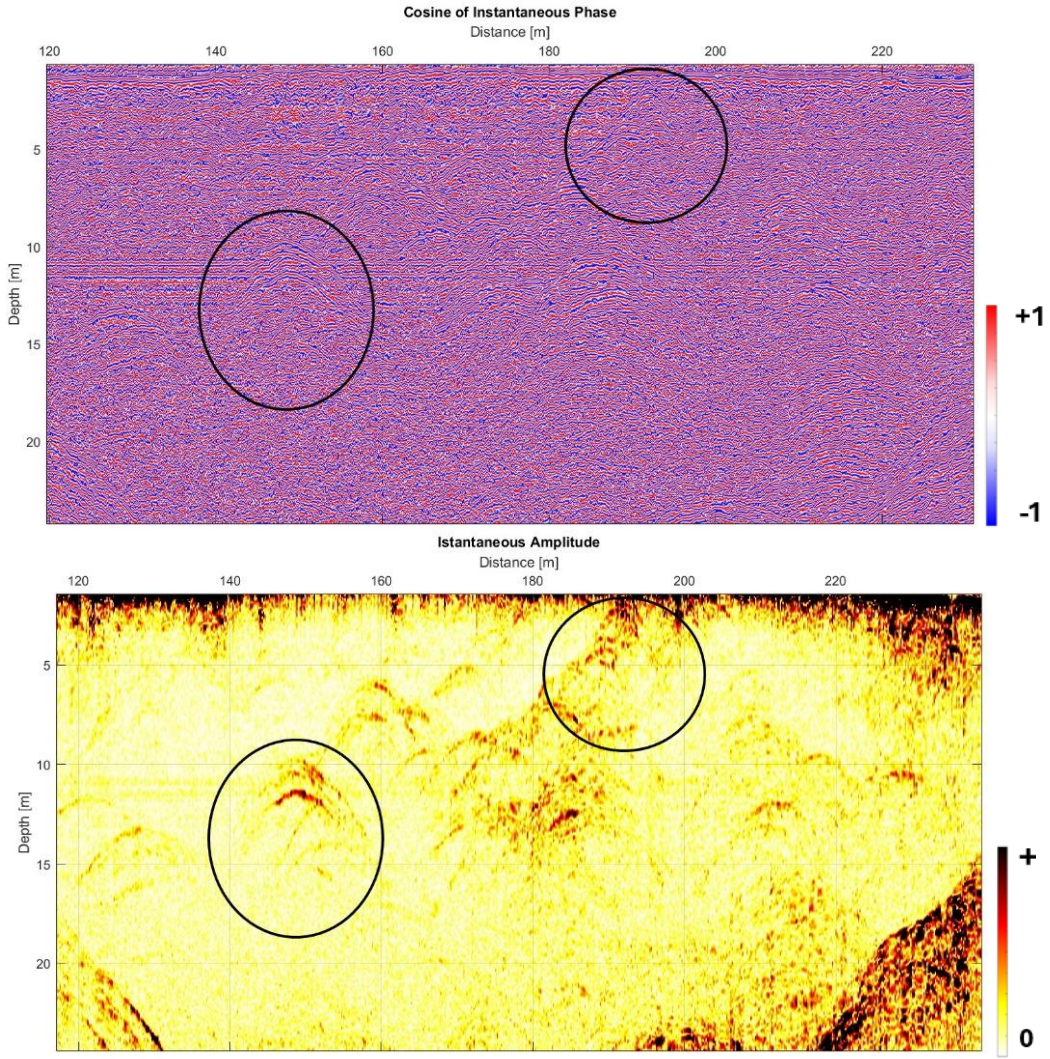

Figure 19 - Cosine of instantaneous phase (above) and corresponding instantaneous amplitude section (below), hyperbolas close-up – Profile 1 (Indren)

On the cosine of instantaneous phase display, the hyperbolas are clearly visible, characterized by a more chaotic signature with respect to the areas of clean ice. Nevertheless, the image presents a large amount of hyperbolas (for the sake of simplicity only two, the most evident ones, have been highlighted) which find a match on the corresponding instantaneous amplitude section, where more details concerning the composition of the material are offered. As a matter of fact, the vertical series of hyperbolas close to the surface are represented in darker shades, standing for a more disturbed signal: this peculiarity appears when the material contains a certain amount of water. Considering the position of the artifacts and the scattering associated, it is very likely that several crevasses with percolating water are detected.

About the wider hyperbolas deeper down into the glacier, they might be other fractures or cavities with air, not yet fully wet, due to the little amount of diffuse scattering shown.

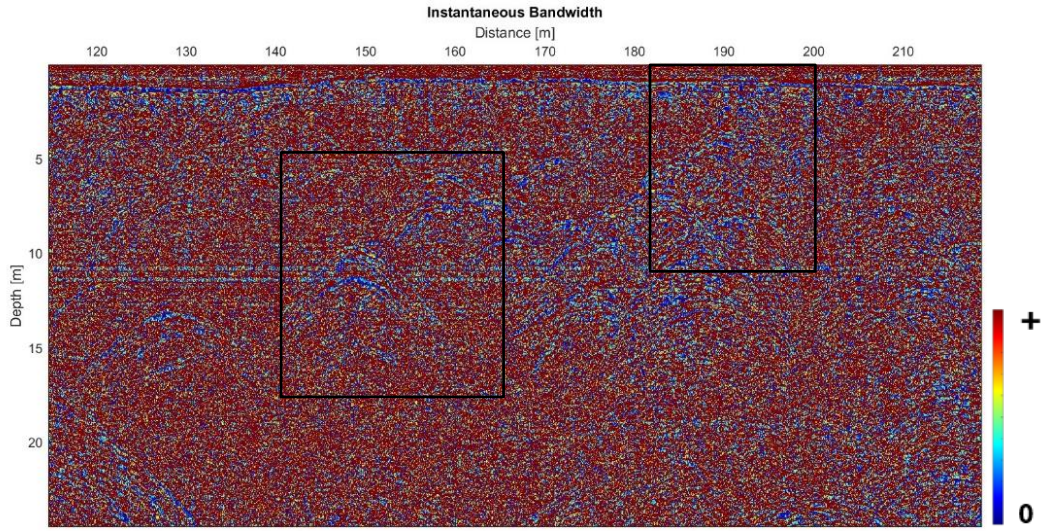

Figure 20 - Instantaneous bandwidth: close-up on the hyperbolas – Profile 1 (Indren)

From the literature, we know that in the instantaneous bandwidth display the areas filled with water tend to show decreased values as a consequence of the absorption by the filtering water of the high frequency components (Forte et al., 2021). We can therefore assess there is a certain measure of liquid percolating down the crevasses and several cavities mostly characterized by air.

Moving on to the bedrock, the picking is performed manually on the GPR section with a specific Matlab code, following the visible interface between ice and rock.

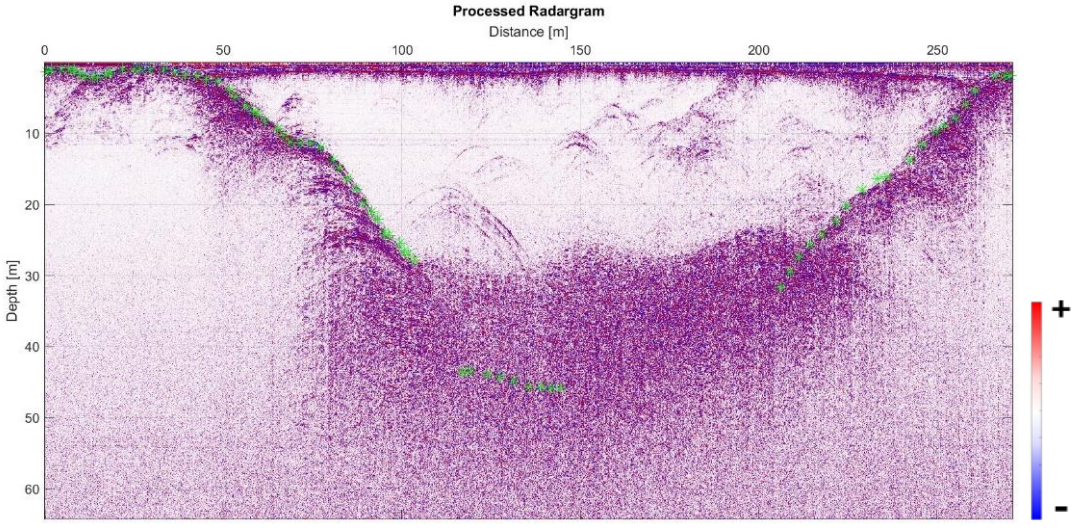

Figure 21 - Bedrock delineation on the GPR section – Profile 1 (Indren)

However, starting from a depth of 30 m, broad scattering influences the identification.
The cause can be related to dirty ice, but for the very confusing pattern of significant thickness (about 20 meters), it is most likely linked once again to the

presence of free water, accordingly to what stated by Santin et al. (2023), which can be explained under three main hypothesis:

1) water percolating through the fractures reaches the bedrock where it excavates cavities and then fills them up (Godio, 2017);
2) an exceptional heat transfer originating from the interaction of the ice with the rocky bottom characterized by a diverse response to stress and deformation (Gutgesell & Forte, 2024);
3) the geothermal heat from underneath the bedrock (Gutgesell & Forte 2024 in Fig.7)

Therefore, it is worth assuming that even in the presence of cold ice, i.e. when the temperature of the glacier is significantly lower than the melting temperature, a shallow layer of ice in the proximity of the interface with the bedrock can reach the melting point [24].

Alpine glaciers are however temperate glaciers with small volumes of water from melting processing free to travel inside the fractures.

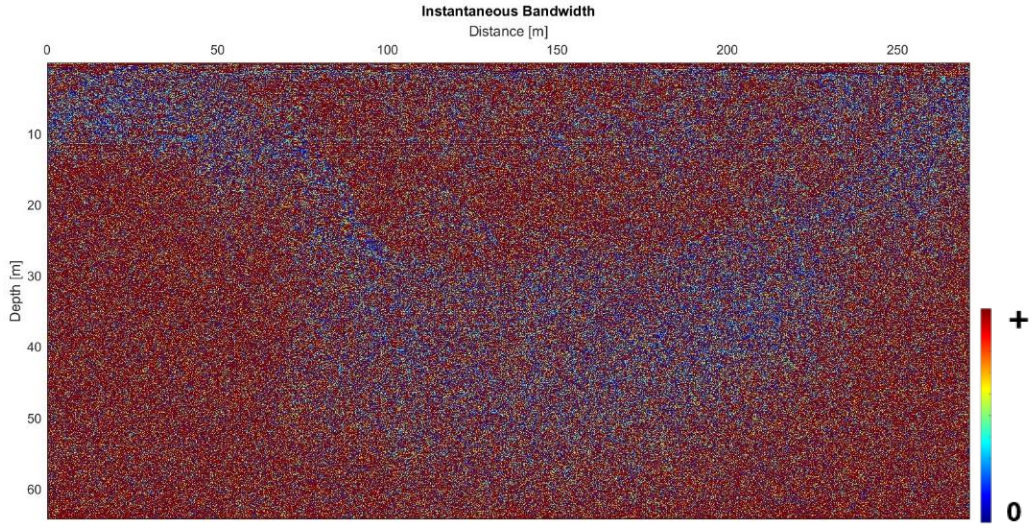

Figure 22 - Instantaneous bandwidth: visible diffuse scattering is present on the bottom – Profile 1 (Indren)

The hypothesis of water seems to be confirmed by the instantaneous bandwidth where very low values are depicted around the area 30 meter-deep.

The sweetness composite attribute offers other hints to support this theory.

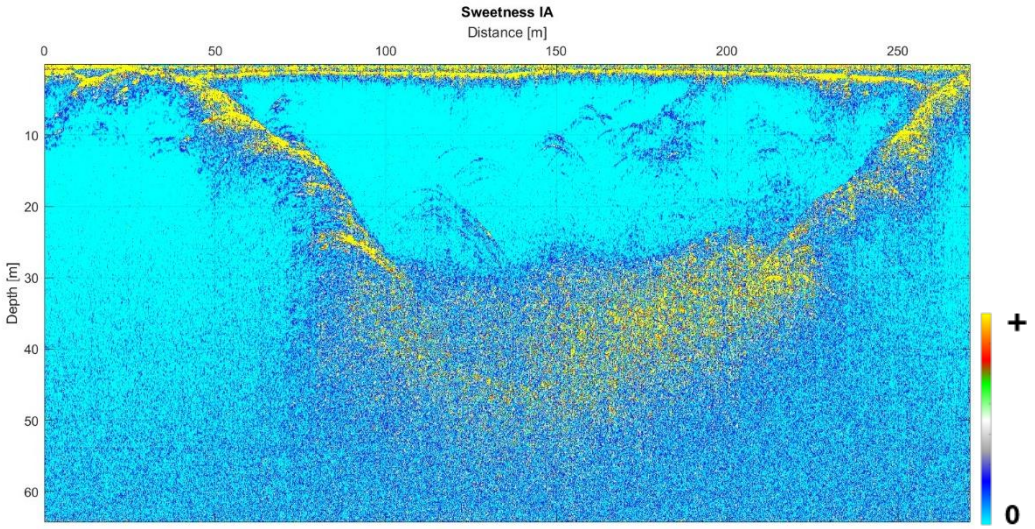

Figure 23 - Sweetness composite attribute - Profile 1 (Indren)

The sweetness attribute is able to enhance the signature of different reflection amplitude zones (Santin et al., 2023), wherever zones with high amplitude and low frequencies are crossed by the signal, the sweetness value will be high. Therefore, the layers of sediments and rocks constituting the bedrock will appear in this case with high sweetness and showing remarkable scattering in the reflection amplitude section.
However, in accordance to what mentioned before and in line with Forte et Al. (2021), high values of sweetness are correlated with the presence of water: this could demonstrate the wet nature of the snow cover, also supported by the summer season, and the free percolating water accumulating on the bedrock. In contrast, the water content inside the fractures is just minimal.
Moreover, it is worth mentioning that part of the high scattering close to the bedrock can be the result of a thermal anomaly forming because of the heat birthing from the friction between ice and the geological material of the bottom. This thermal energy can propagate and warm the cold ice in the upper layers of the glacier. Also, geothermal heat can play a role in the melting process near the bed (Gutgesell & Forte, 2024). This peculiarity will be mentioned again further on in the thesis as it could explain the majority of the features extracted from the attribute analysis.
Therefore, we can state that the high sweetness values all over the bedrock are given by this thermal anomaly and in the lower part, where the signal is more disturbed, some water is present, either from the difference in temperatures, or percolating from the drainage system.

To improve the quality of the bedrock in the zone of scattering, another attribute has been employed.

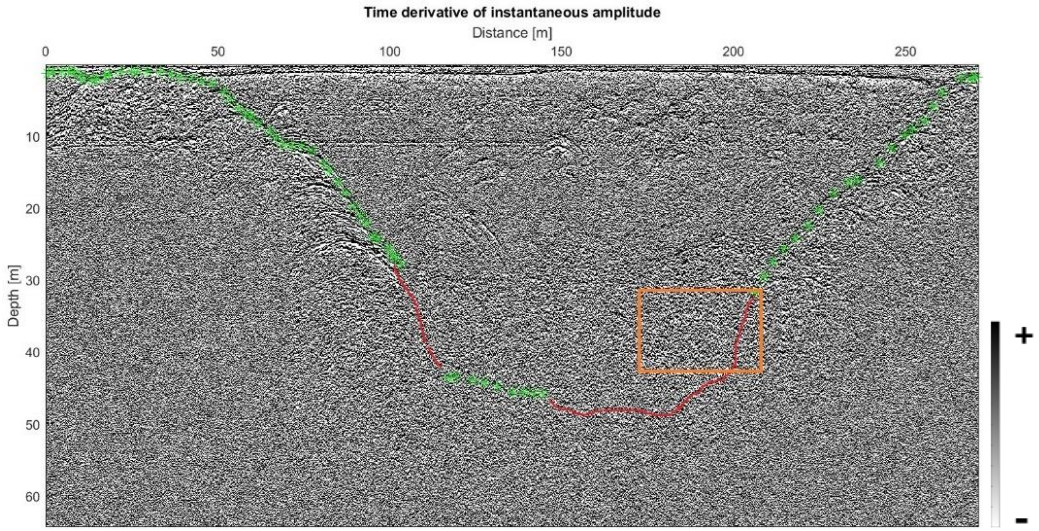

Figure 24 - Time derivative of instantaneous amplitude with bedrock picking. In red are the assumed parts – Profile 1 (Indren)

The original picking was overlapped to the attribute display. In order to better identify the rest of the glacier bed, the time derivative of instantaneous amplitude has been implemented on Matlab. The result provides a more depictable interface: in red are the lines following the trace of the bedrock continuation; in orange is highlighted an evident hyperbola possibly linked to the presence of a cavity with water. Explanation that seems to be supported by the high sweetness around that area.

Below, the attention is focused on the left side of the bedrock, whose outline returned a sharp mark on the cosine of instantaneous phase.

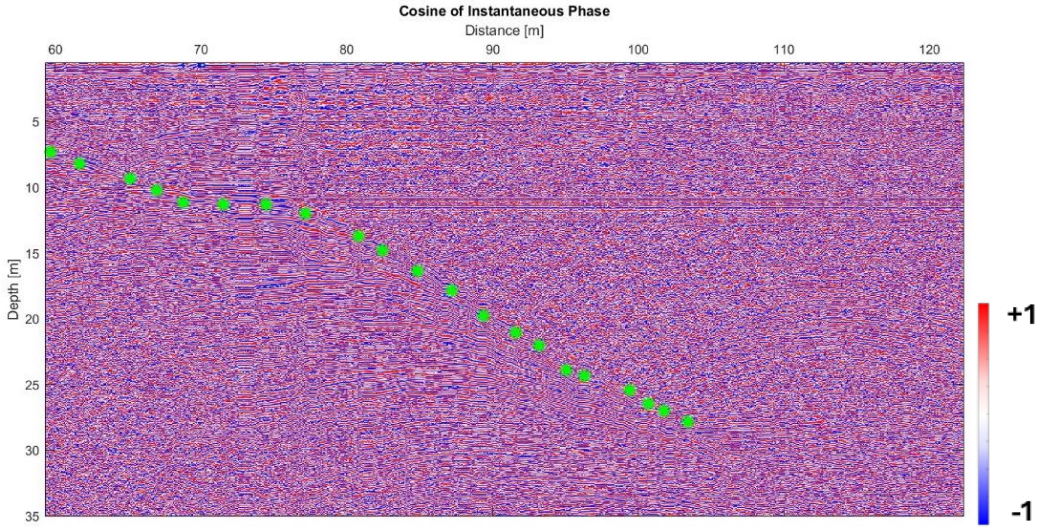

Figure 25 - Cosine of instantaneous phase. Bedrock close-up – Profile 1 (Indren)

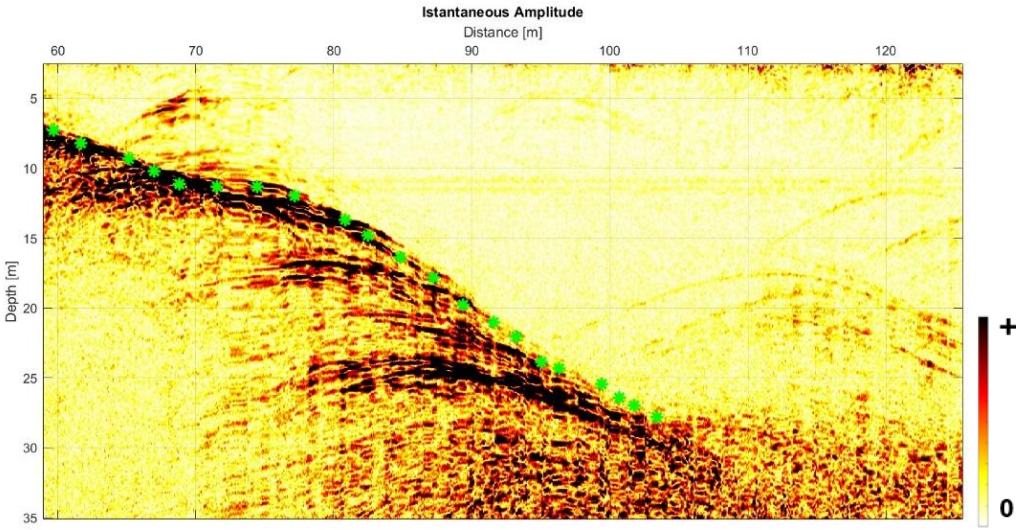

Figure 26 - Instantaneous *amplitude section. Bedrock close-up – Profile 1 (Indren)*

Part of the interface between ice and bottom of the glacier is evident on the cosine of instantaneous phase display. For a better understanding, the comparison with instantaneous amplitude is reported. In particular, through the close-up analysis of the left side, the difference in the behavior of the signal is noted: it appears as minimally disturbed where ice is transparent (probably pure ice) and noisy where the rocks and debris of the bedrock are.

5.2.2 Profiles 2 and 3

Profiles 2 and 3 are two consecutive lines displaying a continuous pattern.

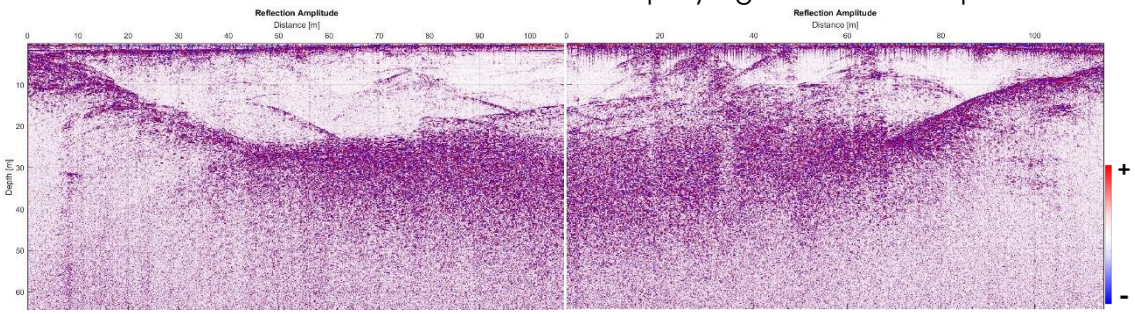

Figure 27 –Amplitude of reflection- Profiles 2 and 3 (Indren)

The snow layer is imaged throughout both profiles and has a thickness of about 2 meters.

If we look at the two sections as a whole, the beginning and the terminal part of the reflection amplitude radargrams are characterized by a well-delineated bedrock, as a result of the cold ice allowing the penetration of the electromagnetic wave inside the body. On the other hand, the central part is blurred, with a lot of scattering, preventing the observer from the ability to pick the bottom properly. As a matter of fact, several isolated hyperbolas in the proximity of the bedrock are depicted by the signal, suggesting the movement

of a certain quantity of free water excavating englacial cavities. Moreover, evident fractures open at the surface of the glacier and spread downwards, opening paths for water to infiltrate and disturb the EM wave.
The analysis will begin with the study of the diffraction hyperbolas and their characterization before focusing the attention on the bedrock picking and reconstruction.

The series of hyperbolas located near the surface of the glacier are highlighted by the cosine of instantaneous phase of profile 3 quite well.
The transition from glacial feature (cavities or crevasses) to cold and clean ice is noticeable before and after the black rectangle.
Once again, for a better understanding, the cosine attribute is compared with the instantaneous amplitude, which offers an improved version of the reflection amplitude in terms of level of scattering.
As a matter of fact, the vertical hyperbolas on the first display correspond precisely to the features portrayed on the second image.

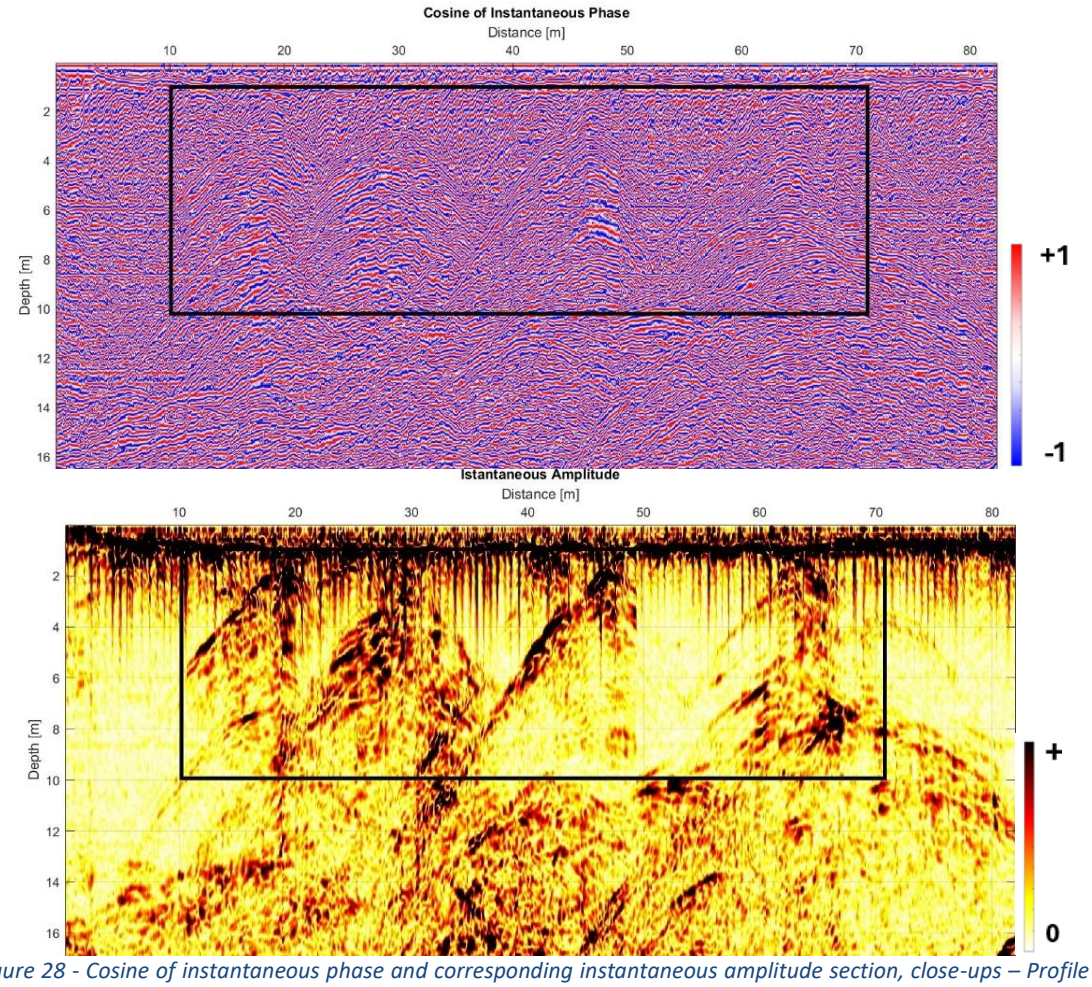

Figure 28 - Cosine of instantaneous phase and corresponding instantaneous amplitude section, close-ups – Profile 3 (Indren)

It is evident that the melting snow on top provides water to the fractures increasing the disturbance around the hyperbolas. Also, due to their vertical shape and similar width, they are most likely crevasses.
Therefore, multiple paths open at the top of the glacier, providing a way for water to infiltrate, flow inside the channels and give birth to a drainage system.

Concerning englacial cavities, they are visible on profile 2:

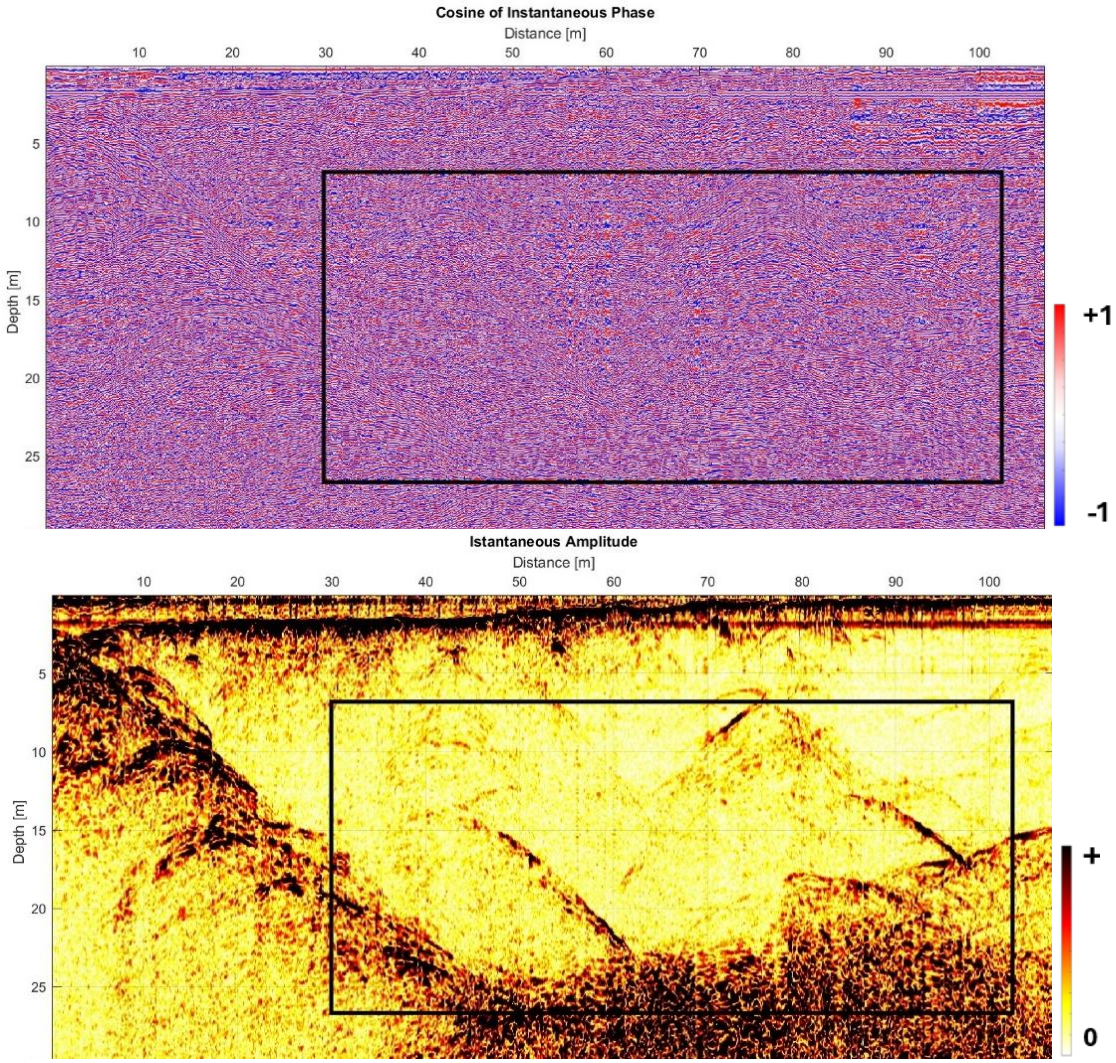

Figure 29 - Cosine of instantaneous phase and corresponding instantaneous amplitude section, close-ups – Profile 2 (Indren)

In this case, the cosine of instantaneous phase did not return a clear pattern for the identification of the cavities. Nevertheless, the instantaneous amplitude suggests once again the hypothesis of cavities excavated by the water flowing on the bedrock, which are here filled with air as the image is not characterized by a high level of scattering.

Certainly, as shown by instantaneous bandwidth and sweetness, free water and temperature differences in the layers depicted by the GPR survey are abundantly present.

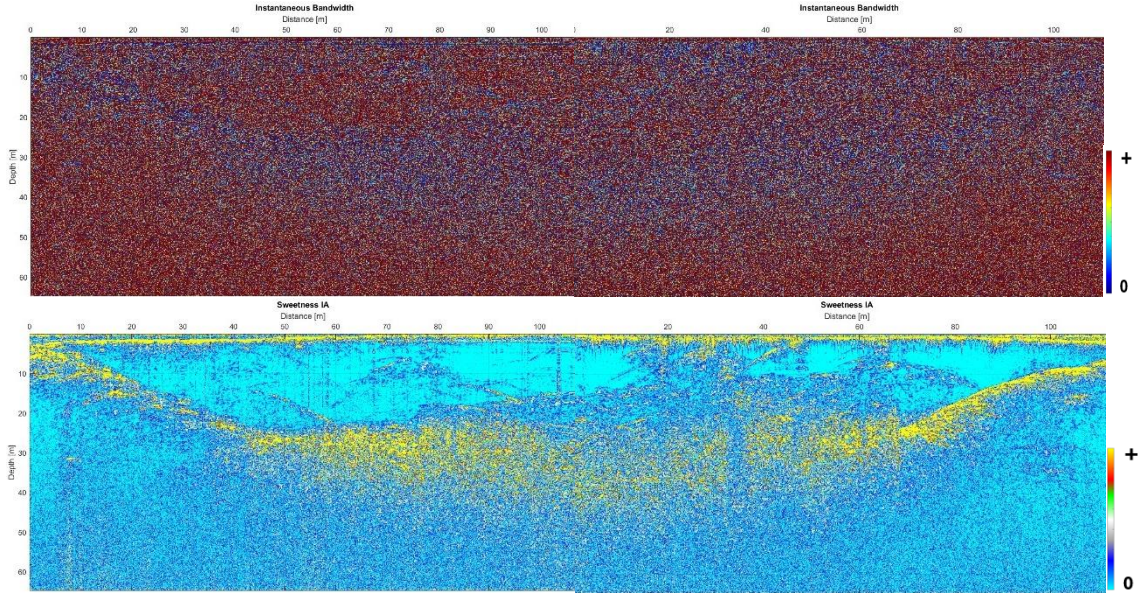

Figure 30 – Instantaneous bandwidth (top) and sweetness (bottom) – Profiles 2 and 3 (Indren)

The anticorrelation between instantaneous bandwidth and sweetness is correctly followed: the frequencies decrease in case of water and the sweetness attribute increases accordingly. As a matter of fact, clean ice has the lowest values in the displays below, whereas they start rising in the areas where we previously hypothesized a certain amount of free water can flow in the drainage system of the glacier. We can state it is mostly located along the snow cover on top and in the proximity of the bedrock, where we should also take into account the thermal effect occurring in the medium below the ice, which could be another source of water by melting the shallow layer of ice immediately on top of the bedrock with an upward heat transfer.
In this regard, the high sweetness near the hyperbolas are given by the meltwater infiltrating from the surface, whereas the scattering on the bottom is due to the presence of the rocks in the bedrock and their temperature, together contributing in turning the cold ice into a warmer medium.

As far as it concerns the picking of the bottom, it can be improved with the time derivative of instantaneous amplitude, which allowed us to assume the missing part of the glacier bed according to the signature on the attribute display.
It is also worth mentioning how well this latest attribute manages to identify the interfaces between the cold ice body and the fractures in the form of sharply marked hyperbolas.

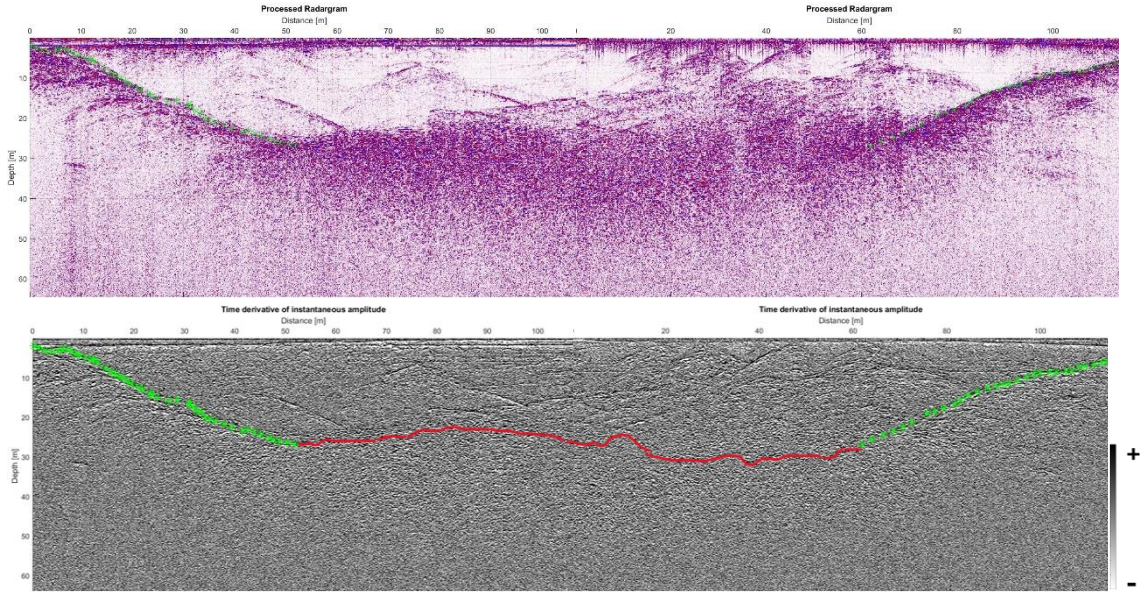

Figure 31 - Bedrock picking on reflection amplitude (top) and time derivative of instantaneous amplitude (bottom). The red line is the assumed bedrock - Profiles 2 and 3 (Indren)

5.2.3 Profile 9

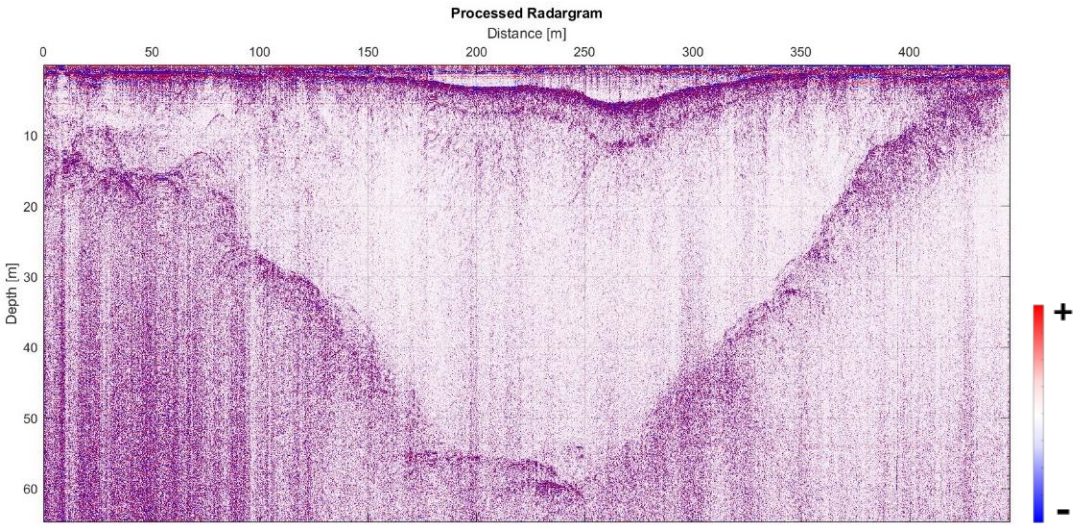

Figure 32 – Reflection amplitude - Profile 9 (Indren)

Profile 9 already provides a good interpretation when processing the GPR signal. The investigation of the reflection amplitude radargram brings to life several interesting features, such as the sharp bedrock, snow accumulations, evident diffraction hyperbolas along the glacier bed, above it, and below the snow pack on the surface.

As a matter of fact, a few vertical diffraction hyperbolas are slightly evident on the left side of the GPR section, suggesting a column-like shape, possibly indicating the existence of crevasses.

The attributes may give us more information regarding this hypothesis.

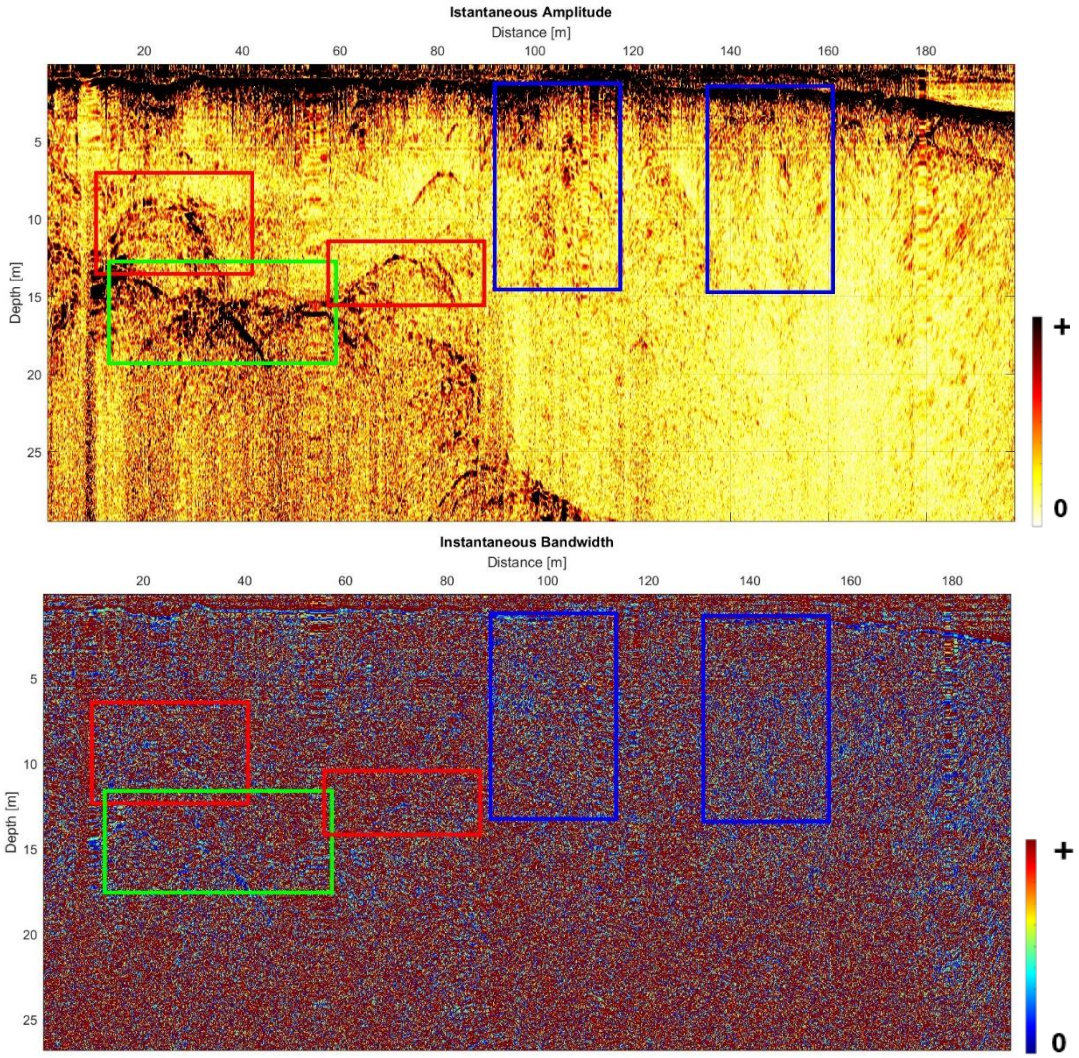

Figure 33 - Instantaneous amplitude (top) and bandwidth (bottom) close up on the hyperbolas - Profile 9 (Indren)

The first comparison takes into consideration instantaneous amplitude and instantaneous bandwidth.
Several hyperbolas are visible:

- inside the red rectangles are cavities: they are located close to the bedrock and contain mostly air;
- the green rectangle highlights pebbles and rocks forming the bedrock;
- the blue rectangle identifies a series of hyperbolas linked to fractures or crevasses near the surface with water infiltration.

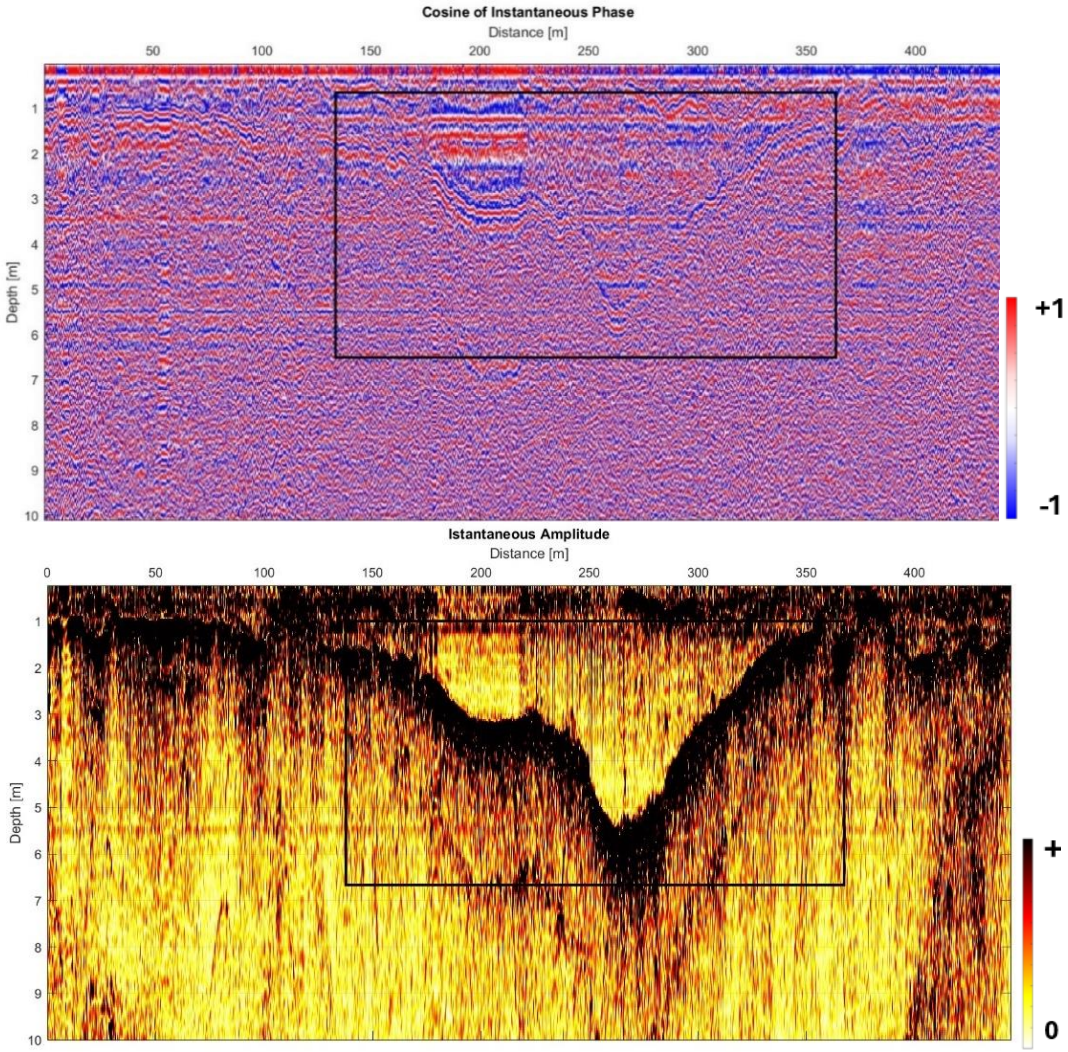

Figure 34 - Cosine of instantaneous phase and corresponding instantaneous amplitude section, top close-ups – Profile 9 (Indren)

The cosine of instantaneous phase was analyzed as it provided a good interpretation for the peculiar signature seen at the top-center of the radargram.
Glaciers are often characterized by mounds of material deposited on the ice body, such as snow or debris, following mass movements. This concave shape is typical of sow accumulation.

About the bedrock, it was already picked to a good extent by the reflection amplitude display. However, several attributes also manage to offer a good representation and were therefore assessed.

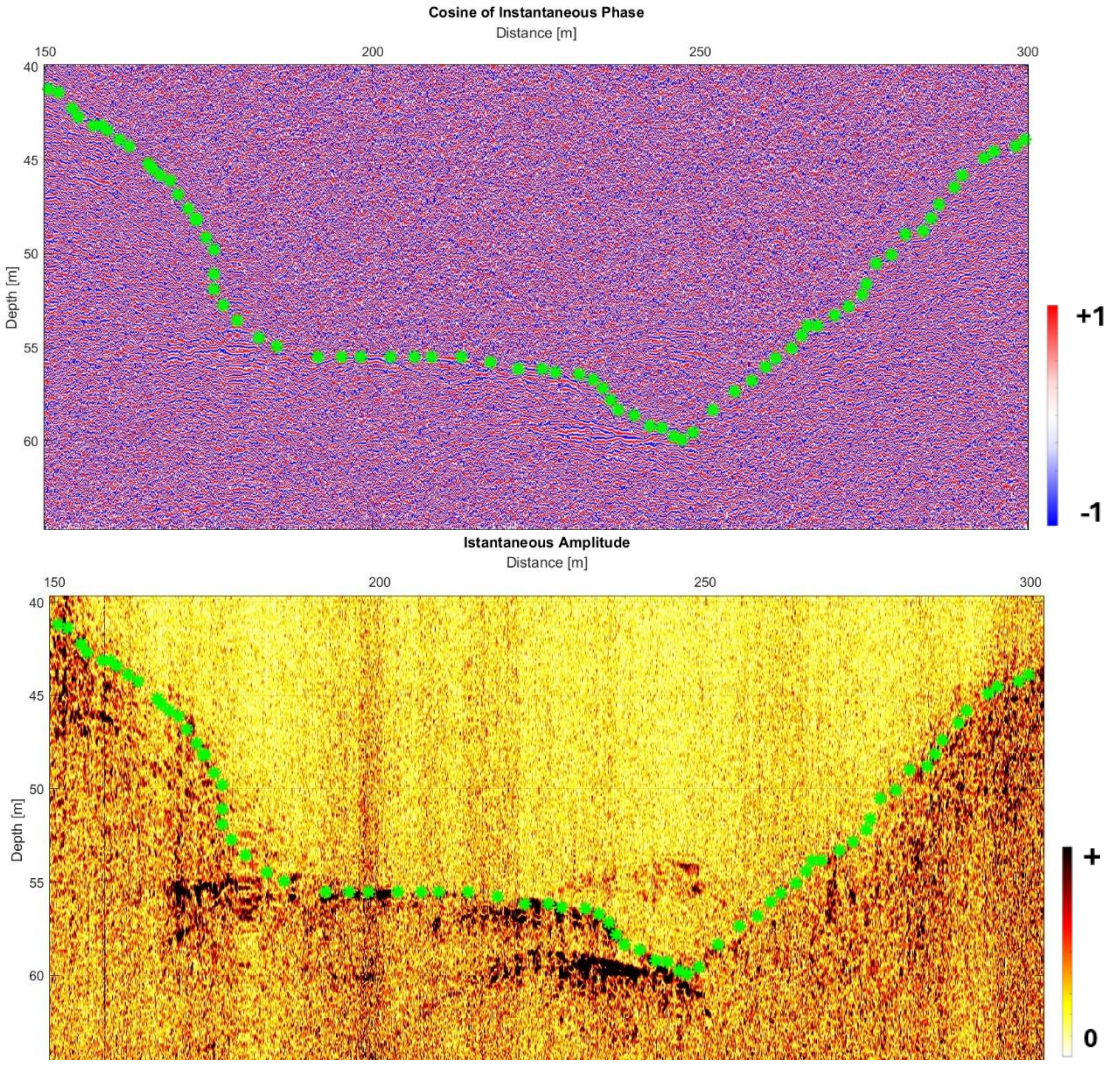

Figure 35 - Cosine of instantaneous phase and corresponding instantaneous amplitude section, bedrock close-ups - Profile 9 (Indren)

The cosine of instantaneous phase was able to return a good outline of the bedrock, which is made of pebbles and we know it presents a thermal gradient with respect to the ice above: this is observed in the diffuse scattering near the bottom and by the shrinking of the frequencies in the instantaneous bandwidth and dominant frequency radargrams shown in the following page.
Once again, it is possible that this behavior is linked to the thermal effect for the interaction of the warmer bottom with the overlying colder ice or to the shallow layer of ice reaching the melting point at the interface with the bedrock, as explained previously.

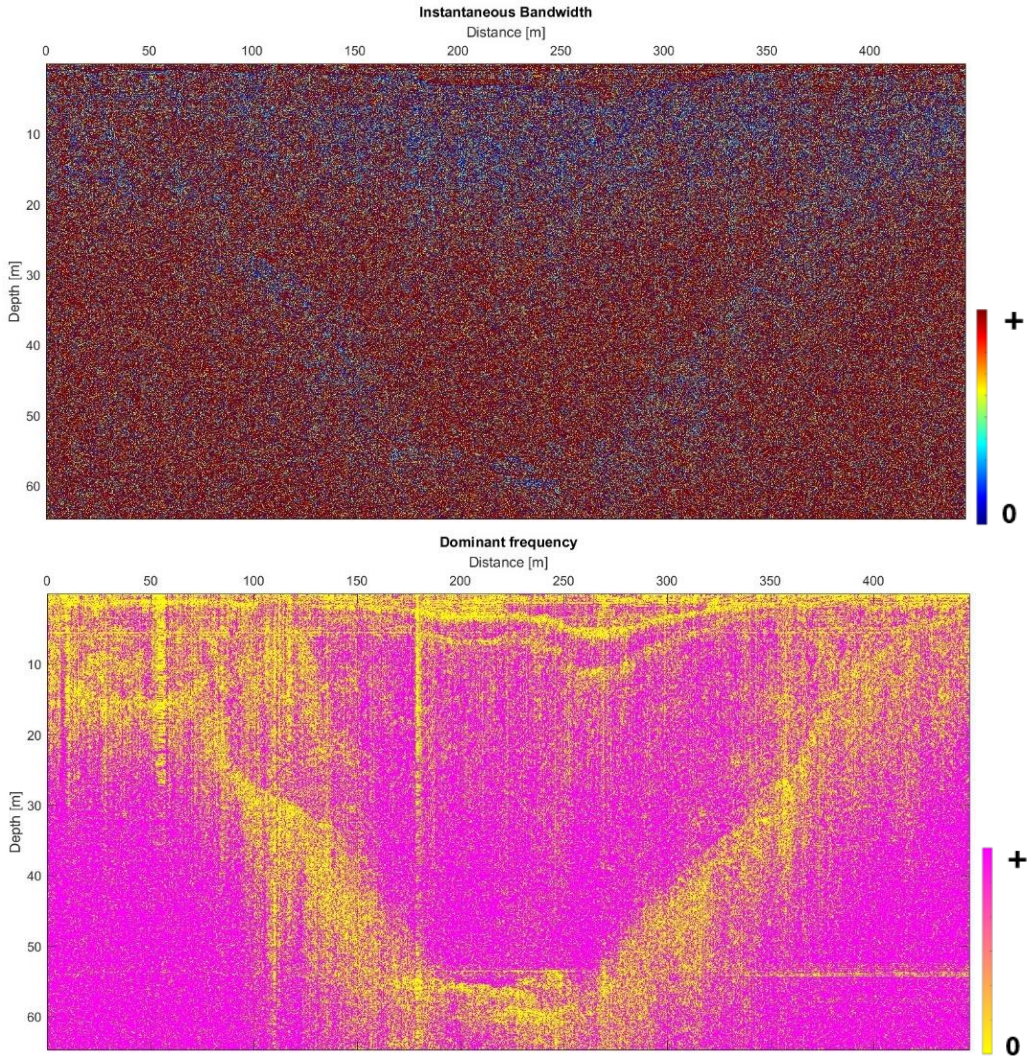

Figure 36 - Instantaneous bandwidth (top) and dominant frequency attributes (bottom) - Profile 9 (Indren)

The sweetness display (Figure 37) confirms the theory of a peculiar warmer interface with a likely presence of a low water content as the values increase slightly along the glacier bed profile. Whereas the warm snow cover causes a higher rise of sweetness for its wet nature.
Some random noise is highlighted in the dominant frequency display in the form of vertical yellow stripes.

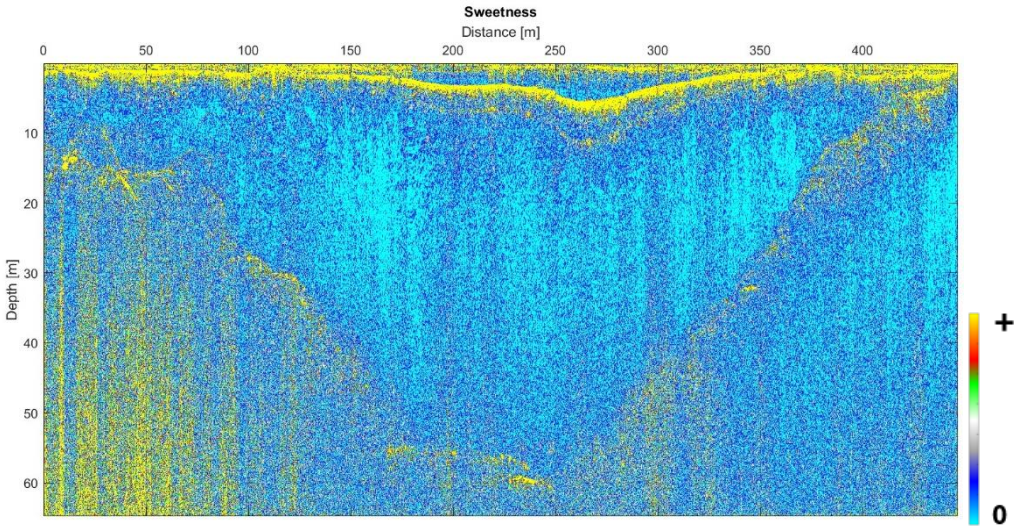

Figure 37 - Sweetness composite attribute - Profile 9 (Indren)

5.2.4 Profile 10

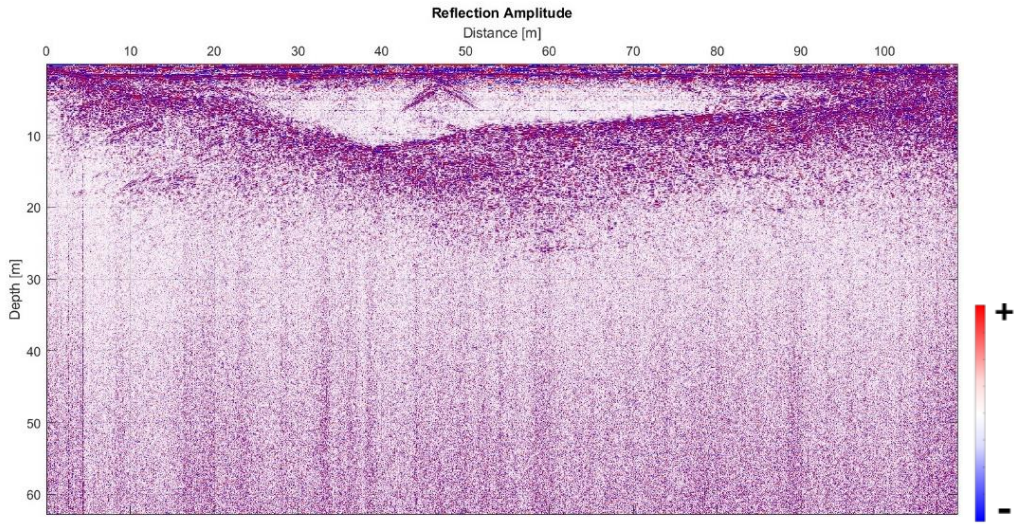

Figure 38 – Reflection amplitude - Profile 10 (Indren)

Particularly evident in this GPR profile display are the hyperbola in the middle, the sharp and shallow bottom interface, and certain artifacts below the bedrock.

The snowpack seems of homogeneous thickness and the spectral response results disturbed at the beginning and at the end of the radargram.

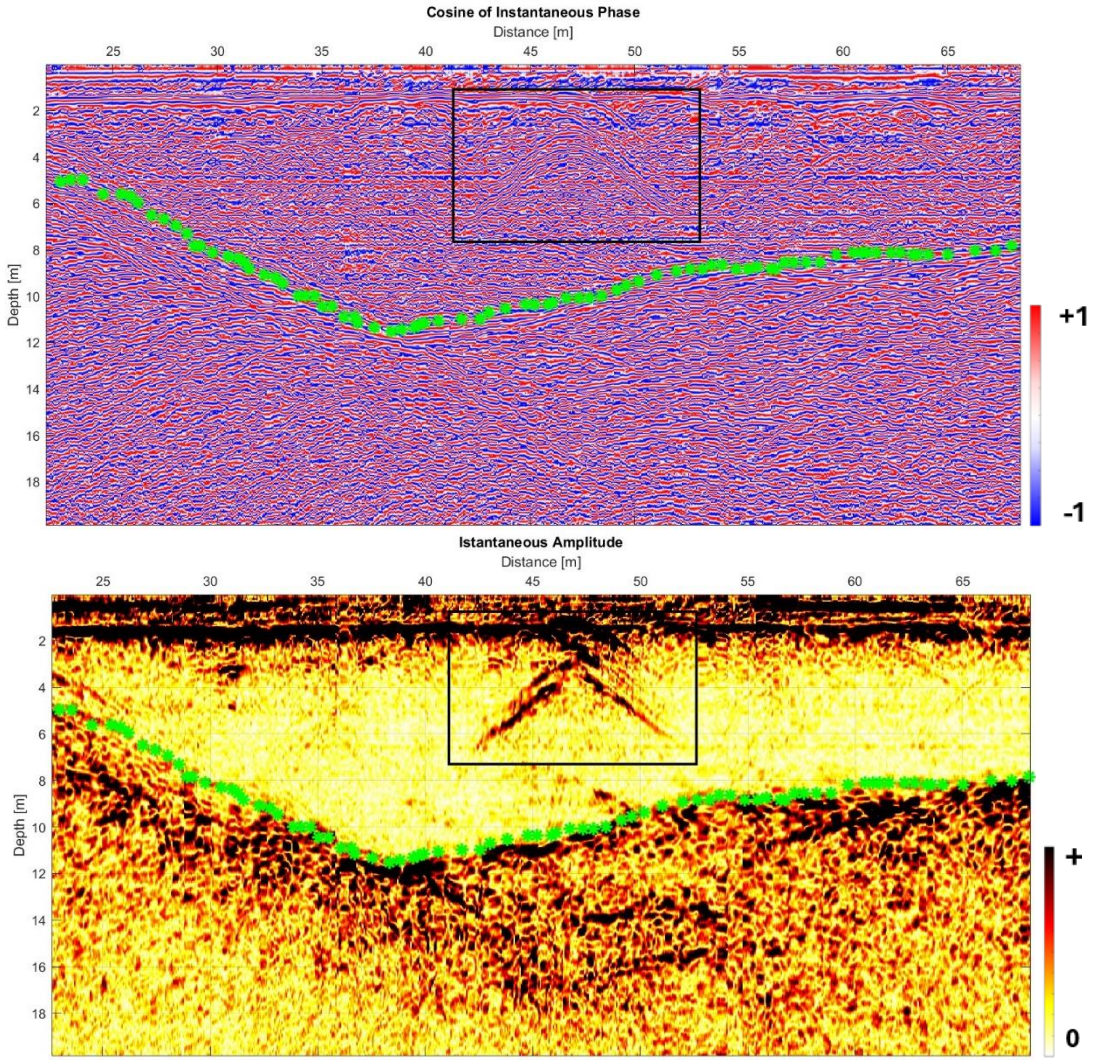

Figure 39 - Cosine of instantaneous phase and corresponding instantaneous amplitude section, close ups - Profile 10 (Indren)

The instantaneous amplitude already provides us an undeniable response concerning the vertical set of diffraction hyperbolas: a crevasse about 6-meter-deep opens up from the top layer of the glacier. The hyperbolas show the same amplitude and are perfectly displayed in a vertical shape.

This feature is well-depicted in the cosine of instantaneous phase and emerges the most when compared to the other curved patterns, less marked, probably representing other small fractures opening at the top of the ice.

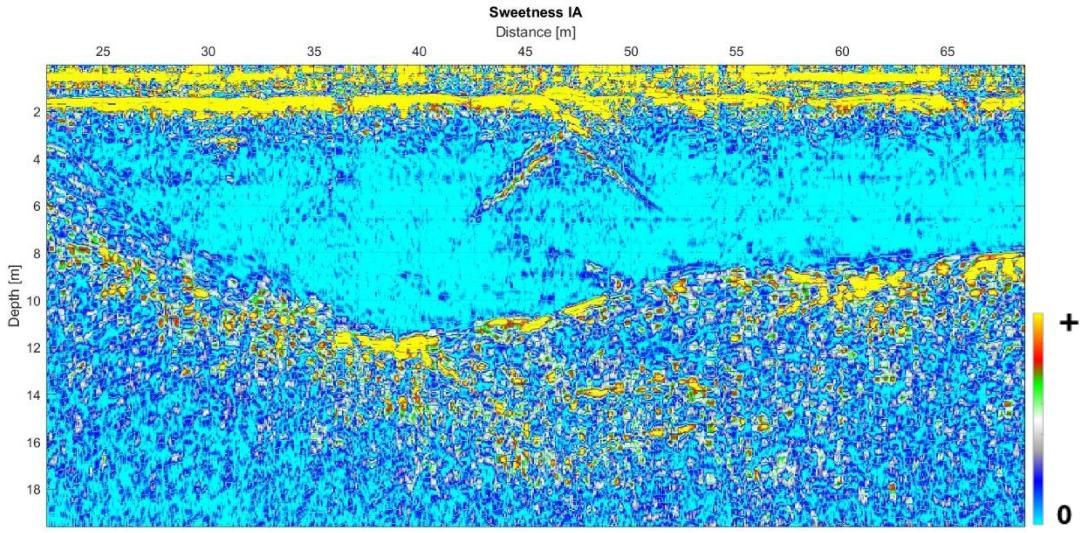

Figure 40 - Sweetness display, close-up - Profile 10 (Indren)

The amount of moisture inside the crevasse is moderate: the water coming from the snow cover percolates inside the fracture and leads to a raise in sweetness.

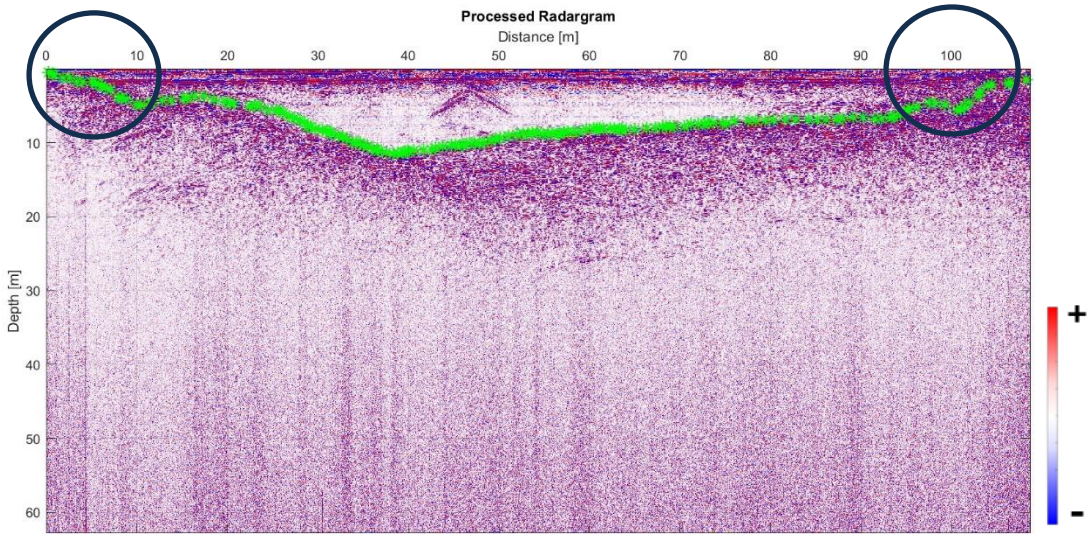

Figure 41 - Bedrock picking - Profile 10 (Indren)

The bedrock is easily manually picked as it appears with a sharp interface. The scattering at the beginning and at the end of the image is due to a certain water quantity freely moving and probably given by the melting of the upper layer of the glacier.

The instantaneous bandwidth, correlated with the dominant frequency, decreases in correspondence of the disturbed spectrum, whereas the sweetness correctly increases.

The glacier bed is mainly made of pebbles and rocks with few water flowing.

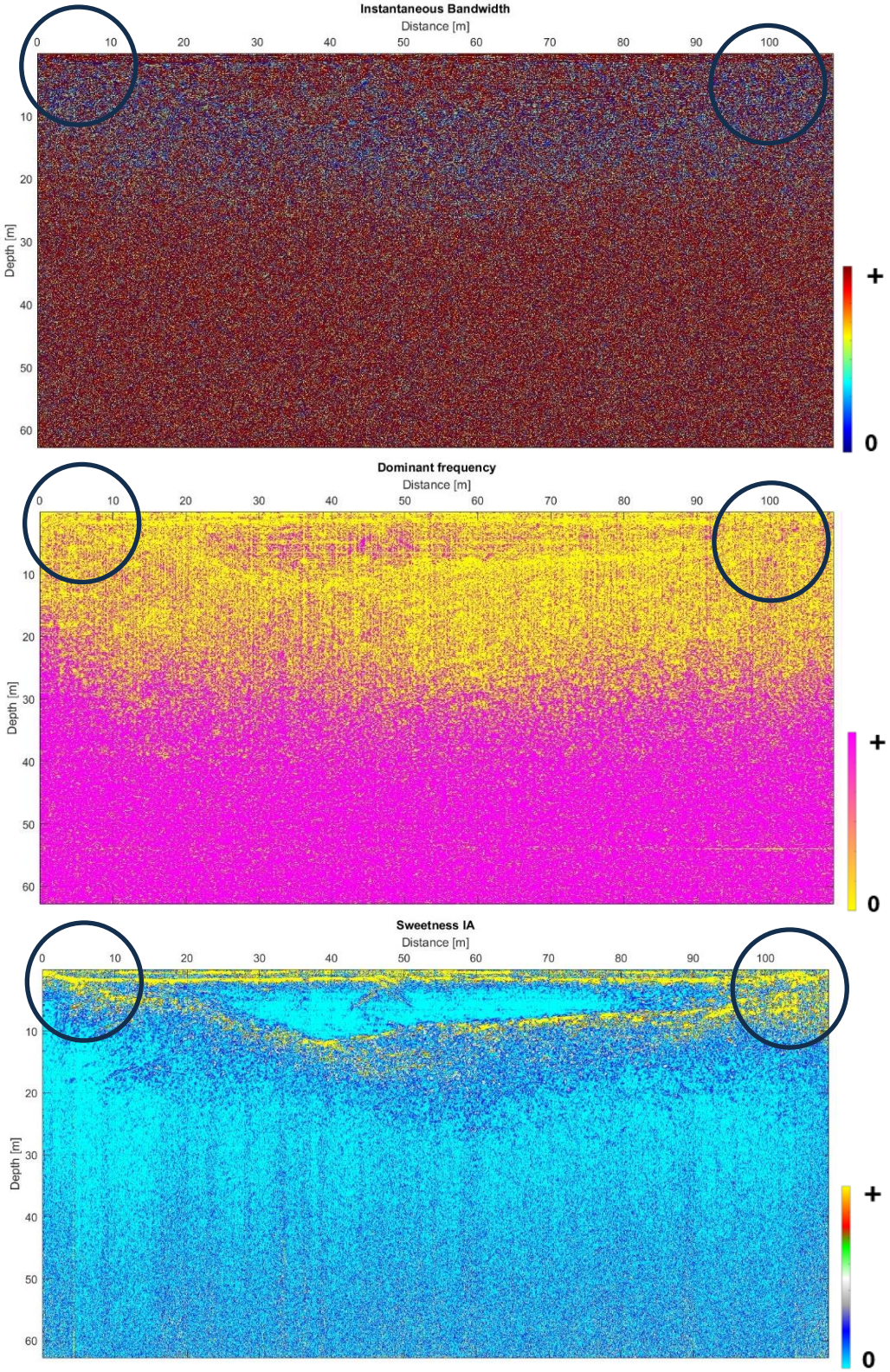

Figure 42 - Instantaneous bandwidth (top), dominant frequency (middle), and sweetness attributes (bottom) - Profile 10 (Indren)

5.2.5 Profile 11

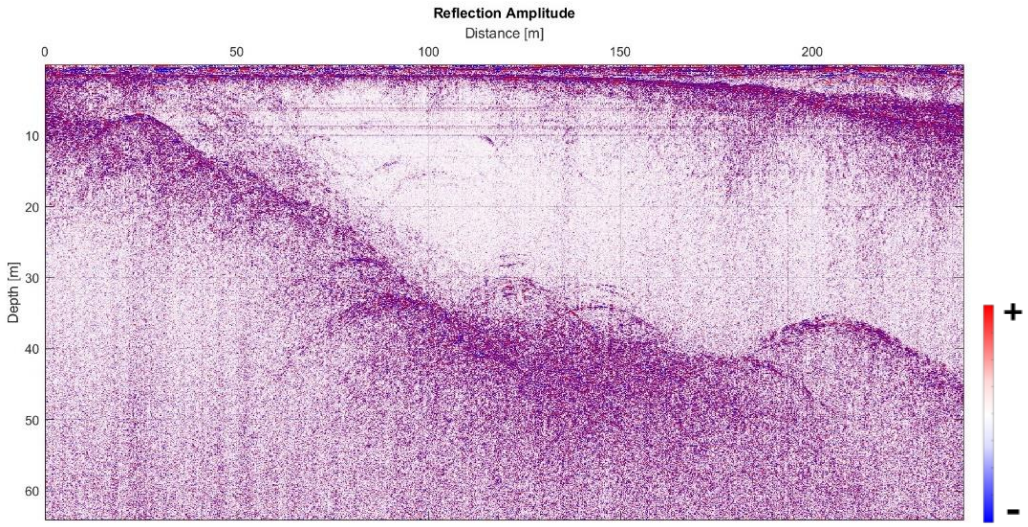

Figure 43 – Reflection amplitude - Profile 11 (Indren)

Starting from the top of the radargram, section 11 shows snow accumulations on the right side and several subtle hyperbolas close to the surface.
Moving down, the bedrock with rocks creating the usual artifacts is, on the other hand, sharply depicted and the presence of some cavities may explain the hyperbolas close to the bottom.
A certain diffuse scattering is present on the top-left of the display and along the bedrock. The attribute analysis will aim once again to better define the patterns.

The snow deposition is particularly clear from the interface visible on the time derivative of instantaneous amplitude radargram.

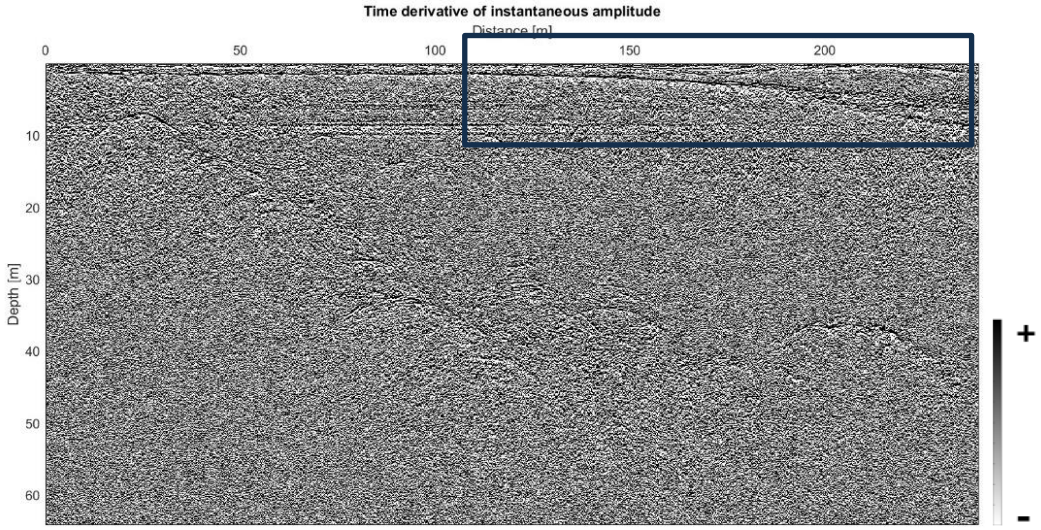

Figure 44 - Time derivative of instantaneous amplitude focused on the snow - Profile 11 (Indren)

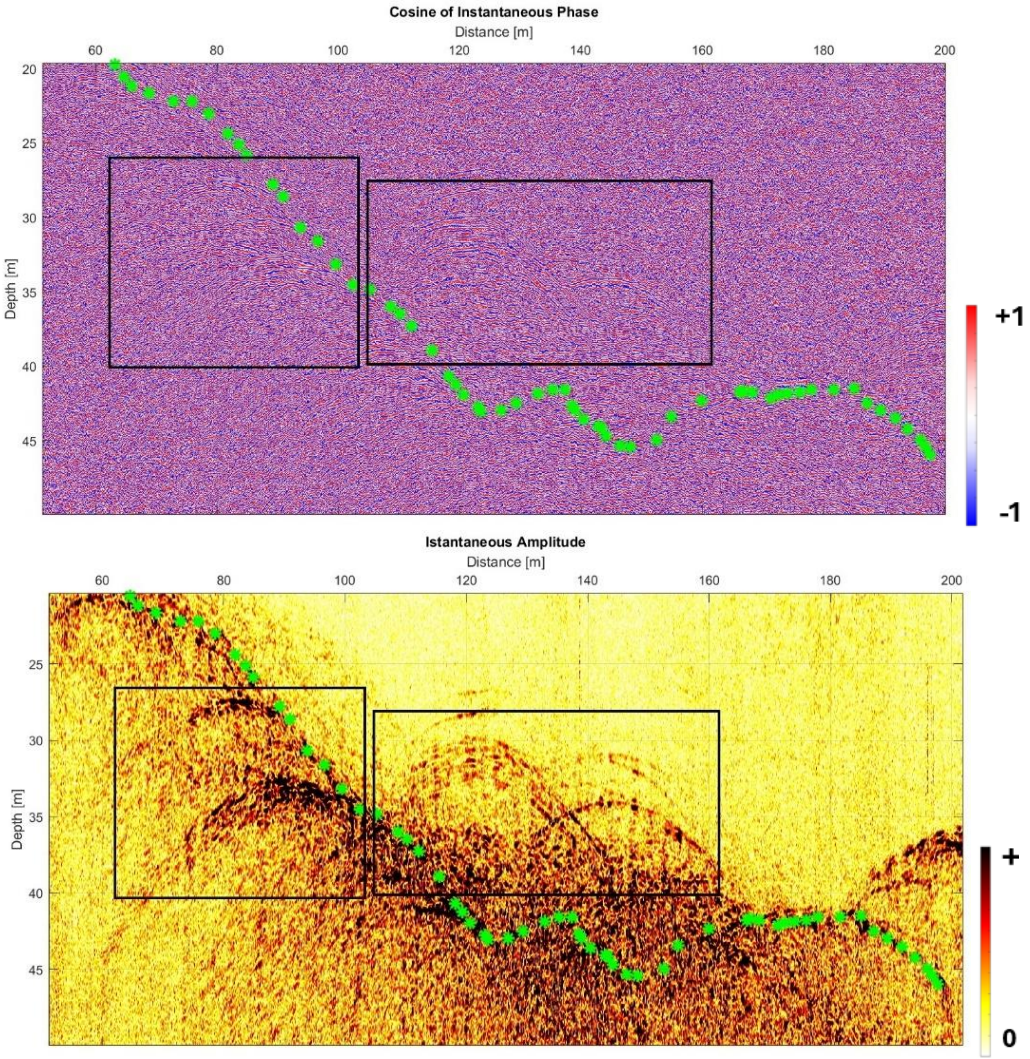

Figure 45 - Cosine of instantaneous phase and corresponding section on the instantaneous amplitude radargram – Profile 11 (Indren)

On the cosine of instantaneous phase section, it is evident once again the contrast between what is supposed to be clean ice and the bedrock medium: the instantaneous amplitude section is helpful to spot the areas where no great scattering is present, being very likely cold and clean ice, characterized by the transparent facies appearance typical of a frozen material with no high level of liquid water or impurities in it. In fact, it is possible to notice a different behavior in the signal pattern above and below the green line representing the picking of the bottom: above the line, the signal has a less chaotic appearance, i.e. ice, whereas below, the pattern results in a more disturbed trend, more likely representative of the bedrock.

The hyperbolas strongly visible in the instantaneous amplitude radargram can find a correlation in the cosine of instantaneous phase section; more precisely, the features are highlighted inside the black rectangles. The fact of being

evident signifies that the signal encounters a different type of material while travelling inside the glacier.
When focusing on the most evident hyperbolas, they are located close to the bedrock: it appears that they form as the result of the presence of englacial conduits created by water. Actually, from the instantaneous bandwidth display we can see that some water is probably flowing on the bedrock and inside the cavity, considering the decrease in frequencies.
At the same time, water can also explain the scattering on the top-left and top-right sides of the display: as a matter of fact, it is very likely that the meltwater from the first layers near the surface create a disturbance for the signal travelling downwards.
The dominant frequency is, as expected, in agreement with the instantaneous bandwidth: both shrink in the presence of the liquid. The behavior is then confirmed by the sweetness attribute which shows an anticorrelation with the other two, increasing with free water (Figure 47).

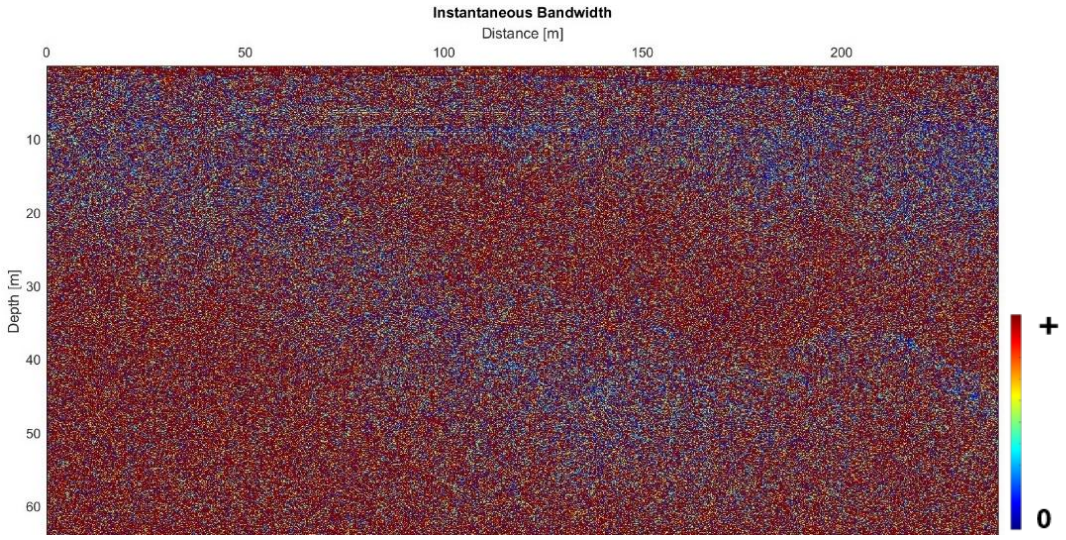

Figure 46 - Instantaneous bandwidth – Profile 11 (Indren)

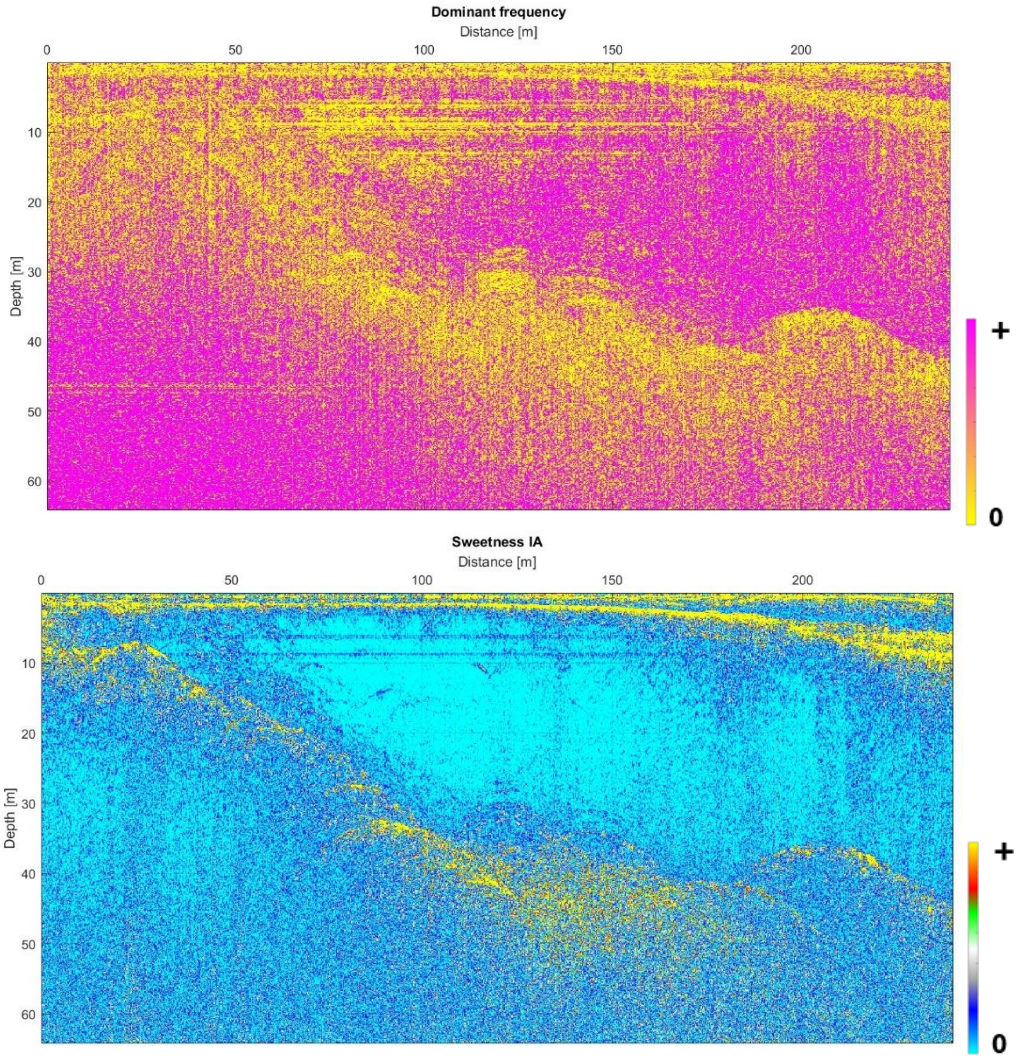

Figure 47 - Dominant frequency (top) and sweetness attributes (bottom) – Profile 11 (Indren)

5.2.6 Profile 12

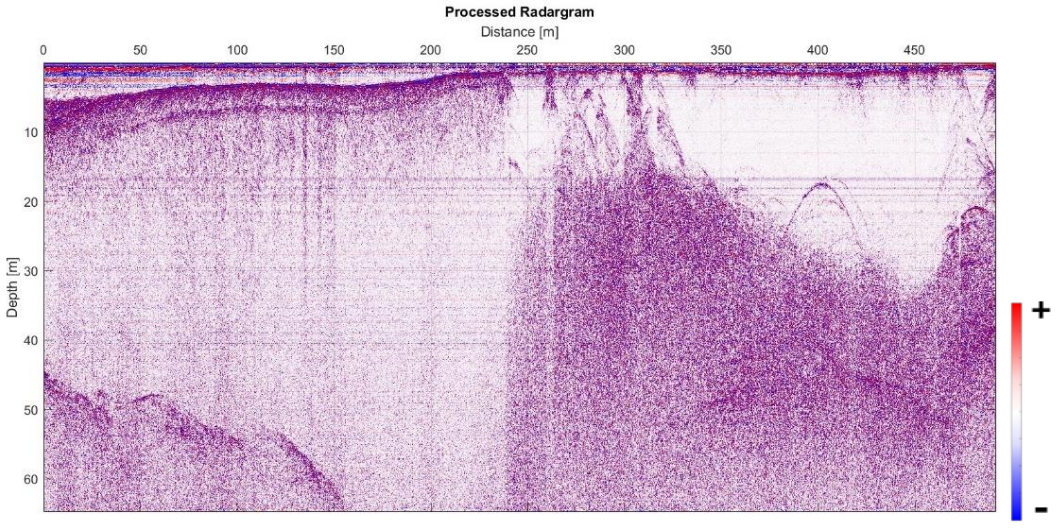

Figure 48 – Reflection amplitude - Profile 12 (Indren)

Profile 12 is characterized by a high level of disturbance on the right side of the radargram; moreover, a sharp vertical disruption line appears at a distance of about 250 meters, which may be related to a sudden movement of the antenna.
Nevertheless, some interesting artifacts can still be recognizable: snow deposition on the left, vertical sets of crevasses in the proximity of the surface, isolated hyperbolas close to where the bedrock should be located.

It is likely that some fractures on the glacier top were the cause of the abrupt antenna displacement and the water infiltration causing the scattering on the right. To support the hypothesis, the attributes are now studied.

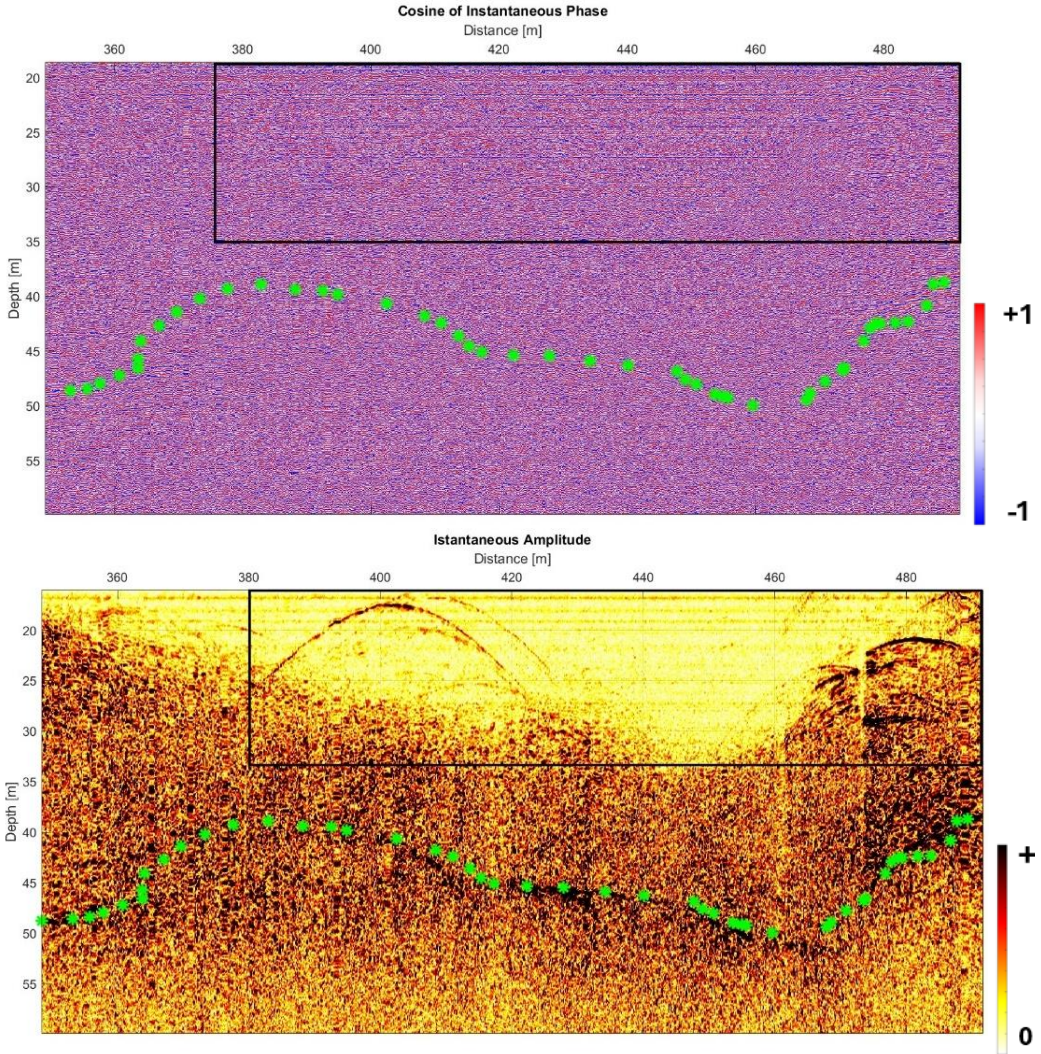

Figure 49 - Cosine of instantaneous phase and corresponding instantaneous amplitude section, right side close-ups - Profile 12 (Indren)

Starting from the isolated hyperbolas, large ones are identified at a depth of about 10 meters, close to the bedrock (highlighted in green): from the signature they present, it is believed that the first one, characterized by no scattering

phenomena, is related once again to an englacial cavity. In this case, the disturbed signal below is probably free water excavating the ice while flowing on the bottom of the glacier.
Concerning the artifacts at the end of the section reported in Figure 49, they are most likely chambers filled with a discrete amount of water.

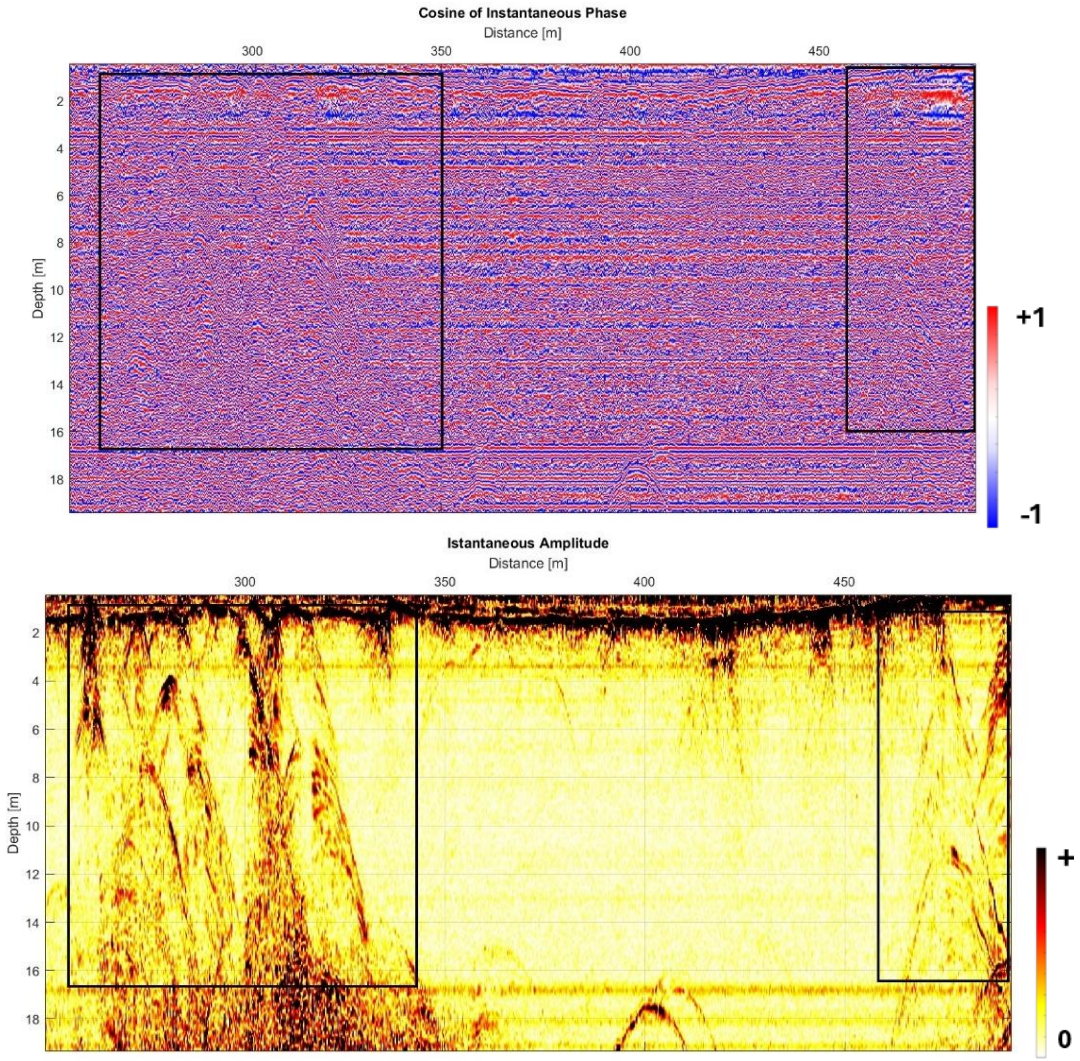

Figure 50 - Cosine of instantaneous phase and corresponding instantaneous amplitude section, top close-ups - Profile 12 (Indren)

The other vertical columns of diffraction hyperbolas are affirmed to be most certainly crevasses, due to their location just below the snow layer and to the same amplitude of the curves. The scattering suggests that meltwater is infiltrating inside the fractures, although in moderate quantities (it is particularly evident on the sweetness radargram in Figure 53).

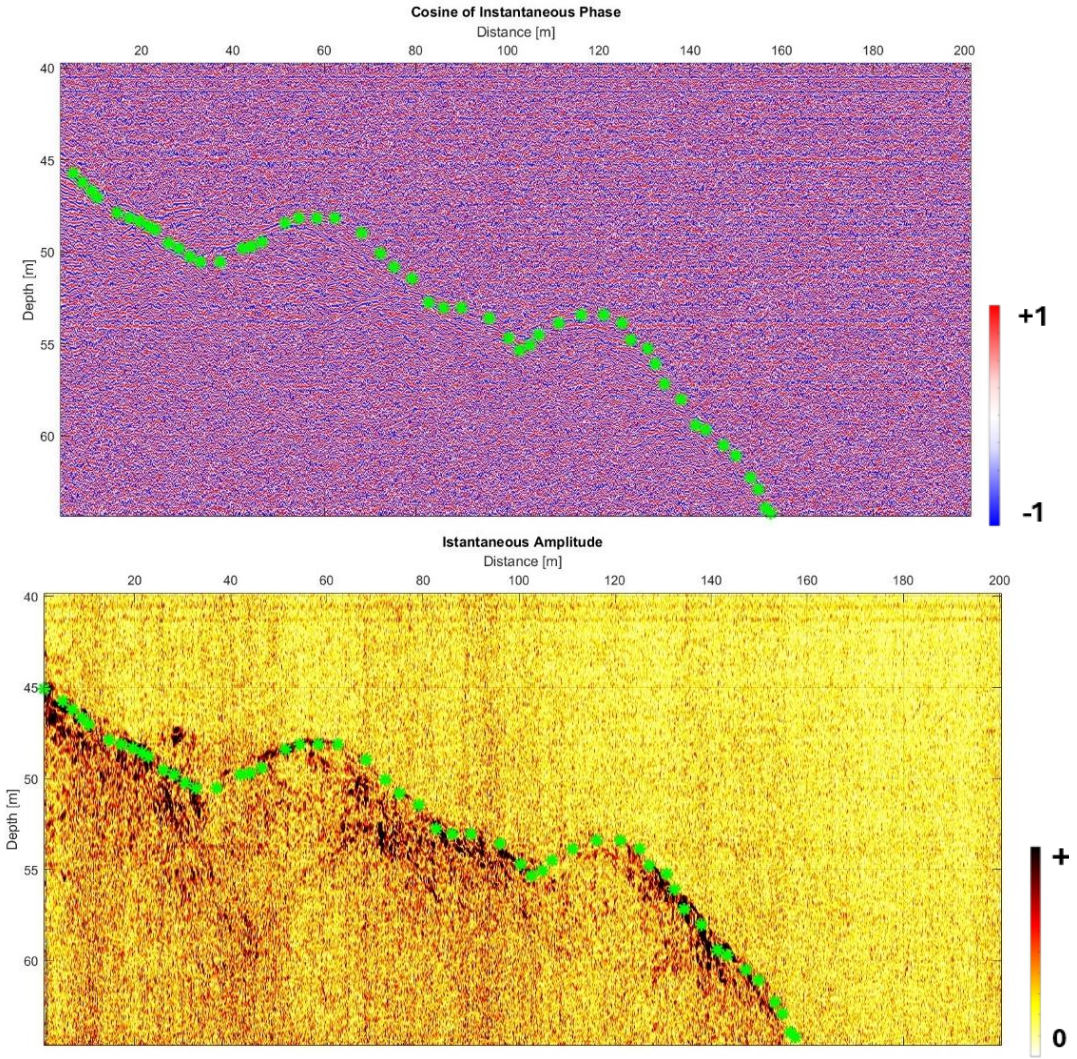

Figure 51 - Cosine of instantaneous phase and corresponding instantaneous amplitude section, left side close-ups - Profile 12 (Indren)

The bedrock is identified with the same picking technique used throughout the whole survey. It is clearly visible on the left side of the GPR radargram and rather hidden on the right.

The cosine of instantaneous phase did not help pick the concealed parts: in this regard, the time derivative of instantaneous amplitude has been analyzed. However, the central zone is not depicted correctly (Figure 52). One hypothesis is that the signal failed in penetrating downward and did not manage to reach the glacier bed due to the high level of disturbance of the electromagnetic wave given by the amount of water or for impurities in the glacier.

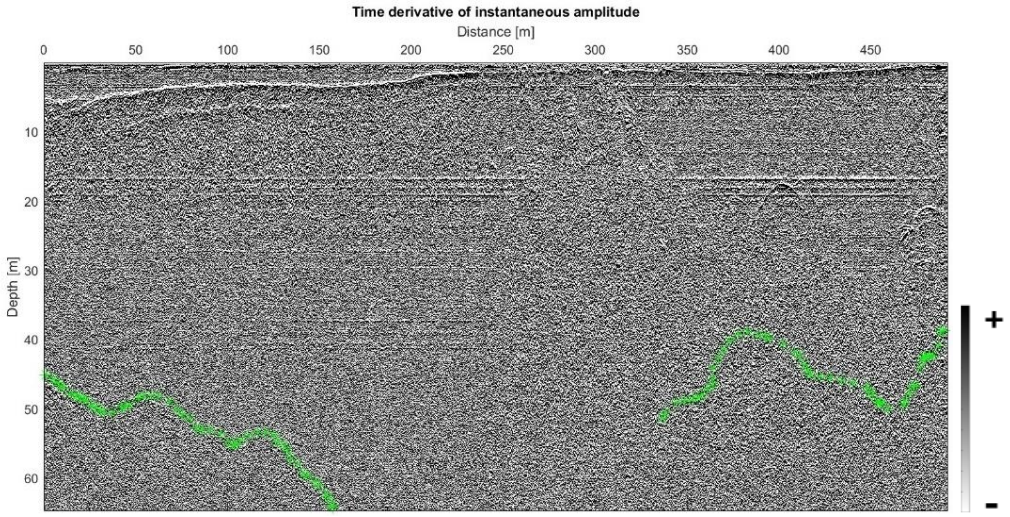

Figure 52 - Time derivative of instantaneous amplitude with bottom picking - Profile 12 (Indren)

The instantaneous bandwidth gives us an idea concerning the amount of noise in the section as the wet parts are probably the areas with increased sweetness.

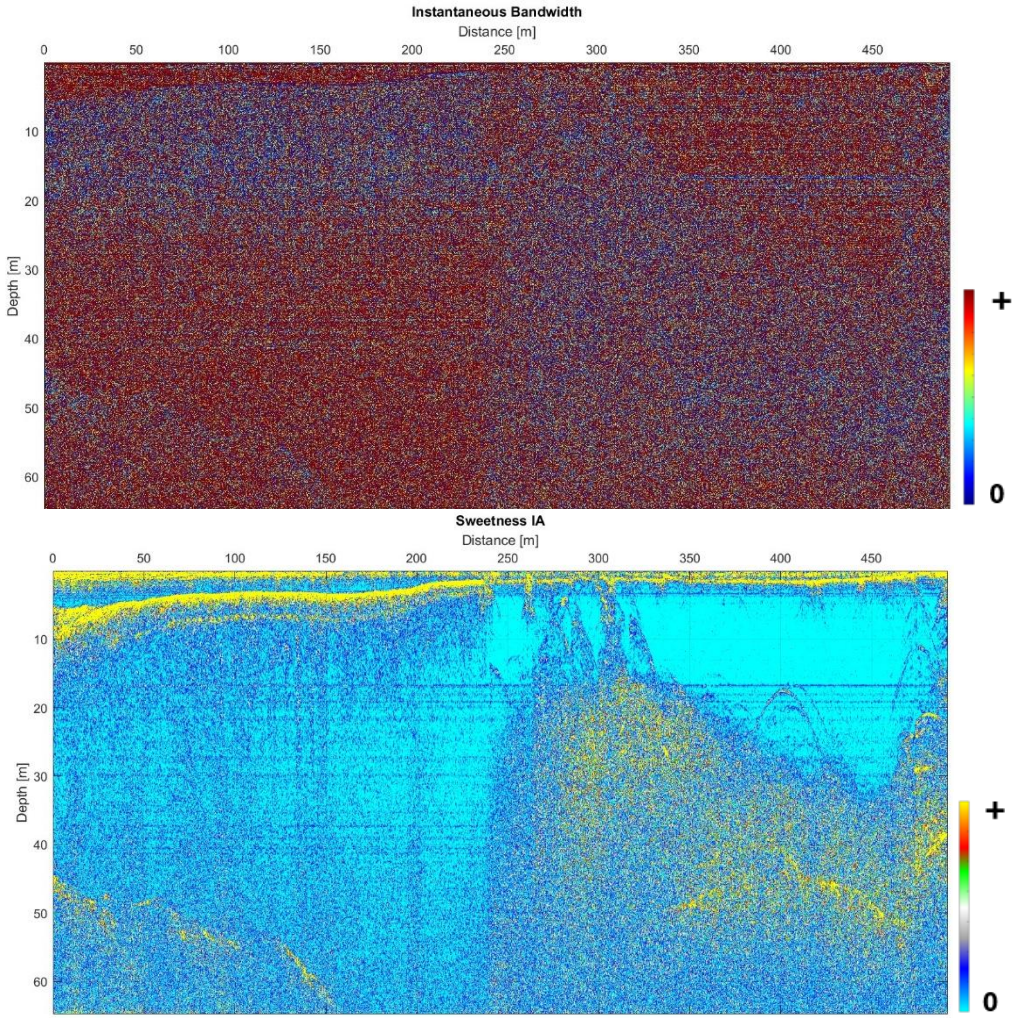

Figure 53 - Instantaneous bandwidth (top) and sweetness attributes (bottom) - Profile 12 (Indren)

5.3 Attribute analysis results – Rutor Glacier

A map reporting the orientation of the processed six lines of the 200 MHz survey is presented in Figure 54. However, profiles 2 and 4 coordinates were not correctly recorded within the GPR data files; for this reason, the two lines are not reported in the scheme. For a better understanding, the reader should refer to Figure 16.

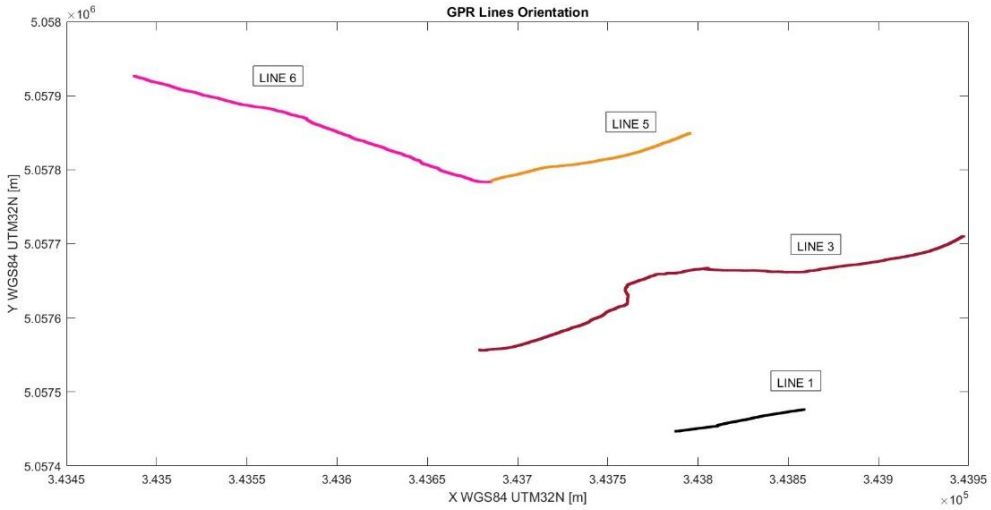

Figure 54 - GPR profiles orientation, 200 MHz antenna

Table 9 - Profiles orientation (Rutor Glacier)

Profile	Orientation
Rut_24_Lid_1_200	Northeast - Southwest
Rut_24_Lid_2_200	Southwest - Northeast
Rut_24_Lid_3_200	Northeast - Southwest
Rut_24_Lid_4_200	Southwest - Northeast
Rut_24_Lid_5_200	Northeast - Southwest
Rut_24_Lid_6_200	Southeast - Northwest

It is essential to analyze the profiles unfolding the most interesting information, to understand the exact position of the moraine: it could be either above the ice, fully underneath or half buried in the glacier.

A moraine is mainly constituted by rock debris and sediments carried and then deposited by the motion of a glacier. Therefore, according to what we learnt through the assessment of the GPR results, in case of a fully submerged moraine, the response on the radargram would be characterized by intense scattering phenomena and possibly hyperbolas given by the rocky debris; on the other hand, if the moraine is located on top of the ice, the image of the internal layers should probably exhibit the typical features of pure ice, i.e.

transparent facies, as the moraine might behave as a sort of “cap” and insulate the cold ice below.
However, it is still important to remind the reader of the temperate nature of the glacier and the resulting amount of meltwater flowing through the ice mass, which causes an increase in the scattering response on the radargram.
In the next chapters, we will evaluate the lines of interest to then reach in conclusion a satisfying assessment of the internal features of the Rutor Glacier and the position of the moraine.

The results obtained after the processing of the data with Matlab were still marked by evident signal noise. We proceeded to perform a band-pass filtering on the data using a reduced interval of frequencies: from the original range of 50-600 MHz, we moved to 120 to 340 MHz.
Despite the ongoing presence of a disturbing effect, in the second case the radargram appears slightly cleaner.
In the figure below, the comparison between the two different filters is shown on the same profile (less noise on the top-center area).

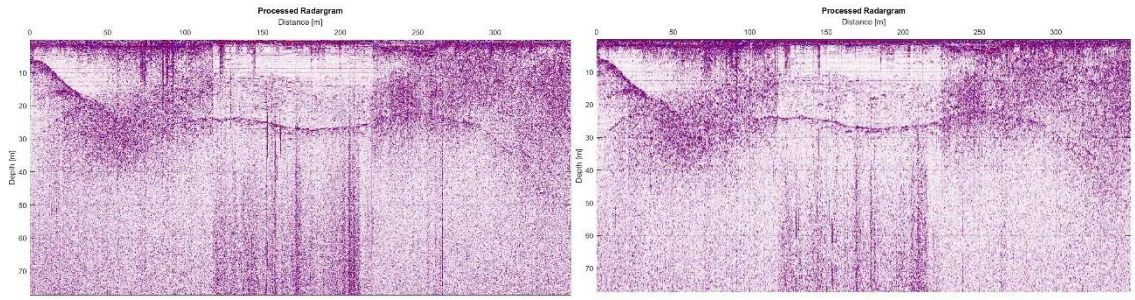

Figure 55 - Comparison between two different band-pass filters on the same profile (profile 2): 50 to 600 MHz on the left, 120 to 340 MHz on the right

For a better visualization of the radargrams, the results processed with a narrower filter are used.
Also, for the sake of simplicity, the lines will be referred to as simply “profile 1”, “profile 2”, etc.

5.3.1 Profile 1

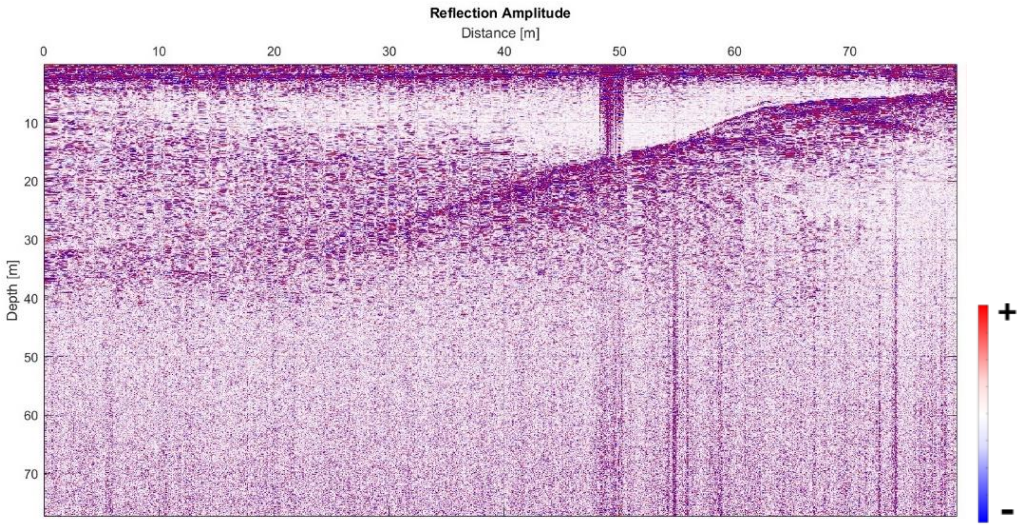

Figure 56 – Reflection amplitude - Profile 1 (Rutor)

Profile 1 does not show any hyperbola in the ice which could possibly indicate the presence of crevasses or cavities; the vertical scattering at a distance of 50 m is clearly random noise which did not disappear with data filtering. Although, what is interesting to notice is the scattering on the left side of the image, limiting the identification of the bedrock.
Therefore, the following attribute analysis will try to offer an interpretation of the disturbing phenomena.
Nevertheless, the picking of the bottom has been performed where possible.

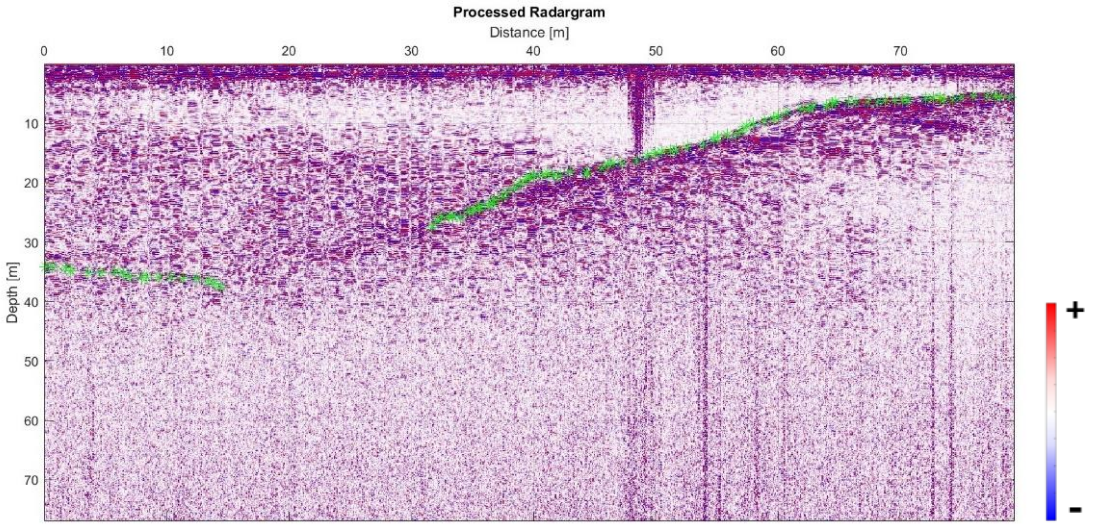

Figure 57 - Bedrock picking - Profile 1 (Rutor)

From the close-up of the time derivative of instantaneous amplitude, some features reminiscent of a possible prolongation of the bedrock are slightly visible and marked in red.

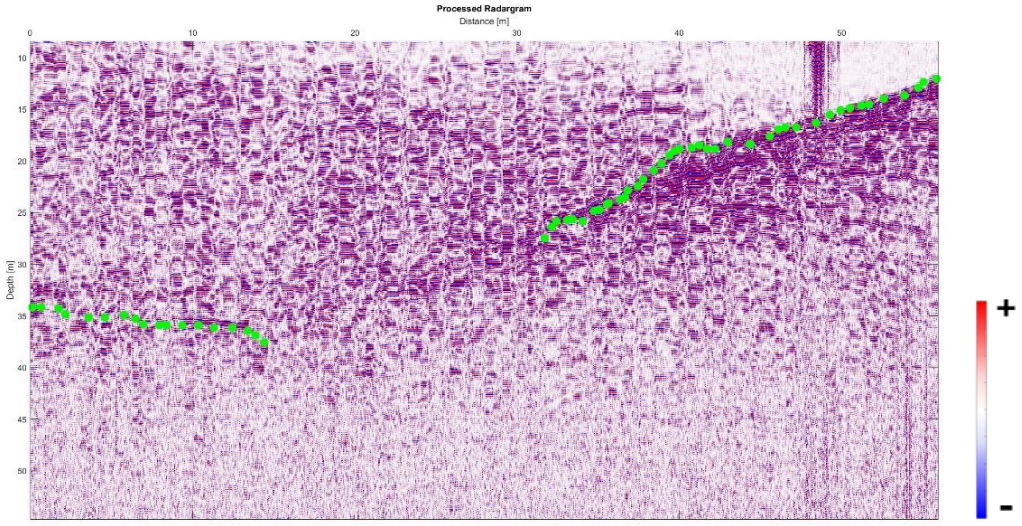

Figure 58 - Close-up on the bedrock picking – Profile 1 (Rutor)

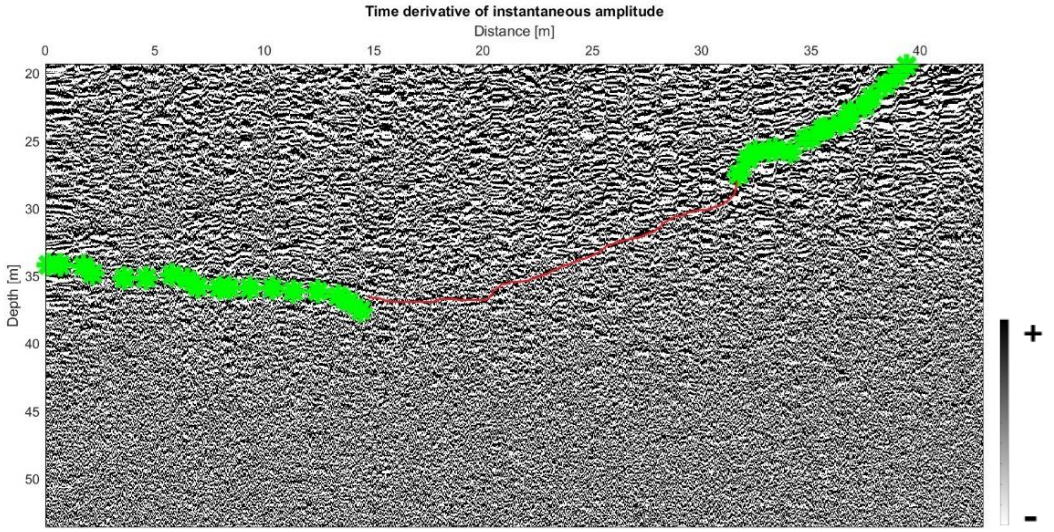

Figure 59 - Reflection amplitude close up and corresponding time derivative of instantaneous amplitude close up on the bedrock – Profile 1 (Rutor)

In order to define the nature of the scattering phenomenon on the left of the radargram, instantaneous bandwidth and sweetness come to help for this profile, whereas the dominant frequency did not provide any useful information being characterized by extreme noise.

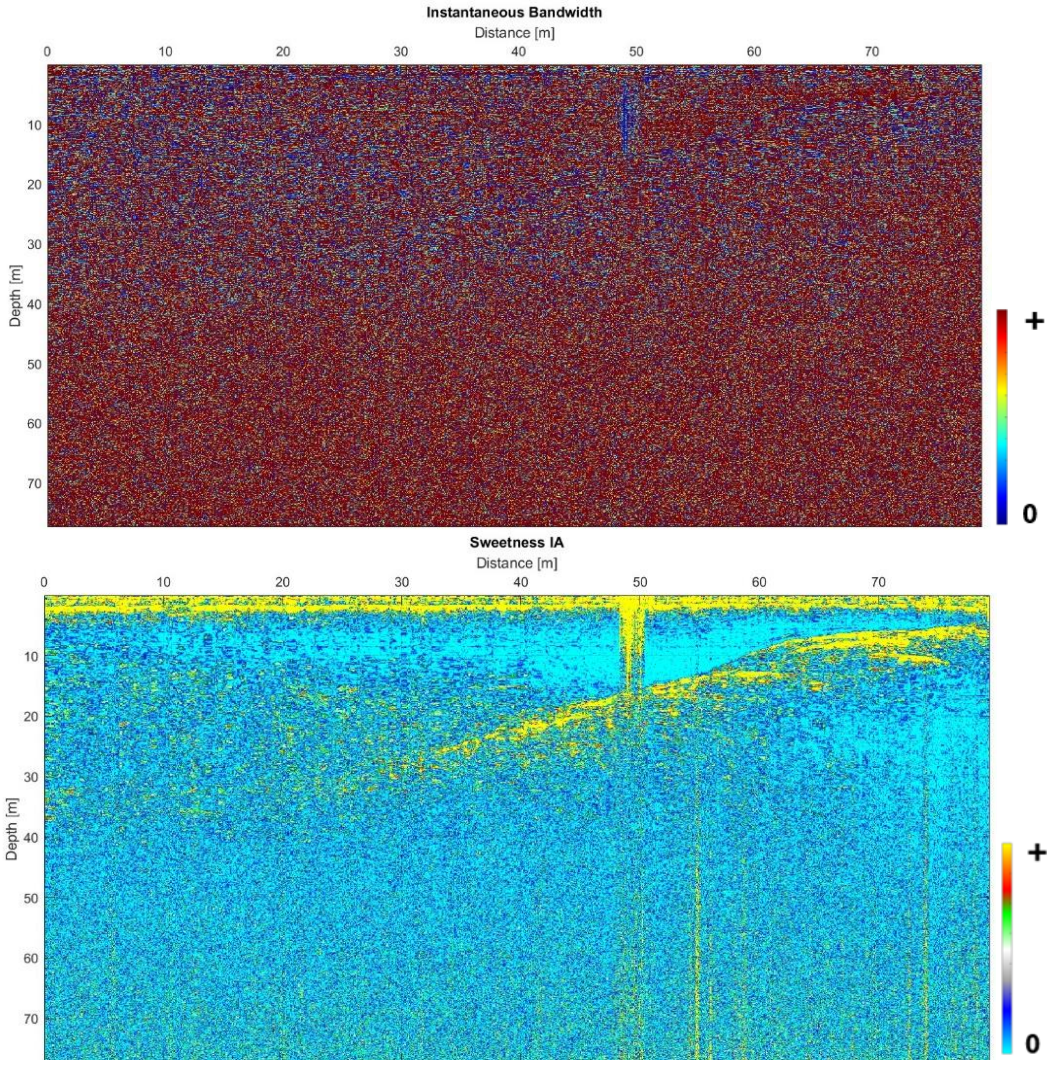

Figure 60 - Instantaneous bandwidth (top) and sweetness (bottom) – Profile 1 (Rutor)

Once again, it is necessary to disregard the "column" representing the disturbing effect already mentioned.

When focusing on the scattering affecting the radargram up to around a 40 meter-distance, it appears to show low values of instantaneous bandwidth which find an anticorrelation with the behavior observed in the sweetness display. We may assess the nature of the phenomenon can be attributed to a small quantity of water or warm ice disturbing the radar signal: as we already mentioned for Indren, the values of sweetness tend to increase in the presence of water, showing an opposite trend with respect to instantaneous bandwidth.

5.3.2 Profile 2, 3 and 4

Profiles 2, 3, and 4 cross the moraine: therefore, they are going to be analyzed together in order to better understand the position of the glacial drift through the study of any similar behavior of the electromagnetic wave when encountering the moraine material.

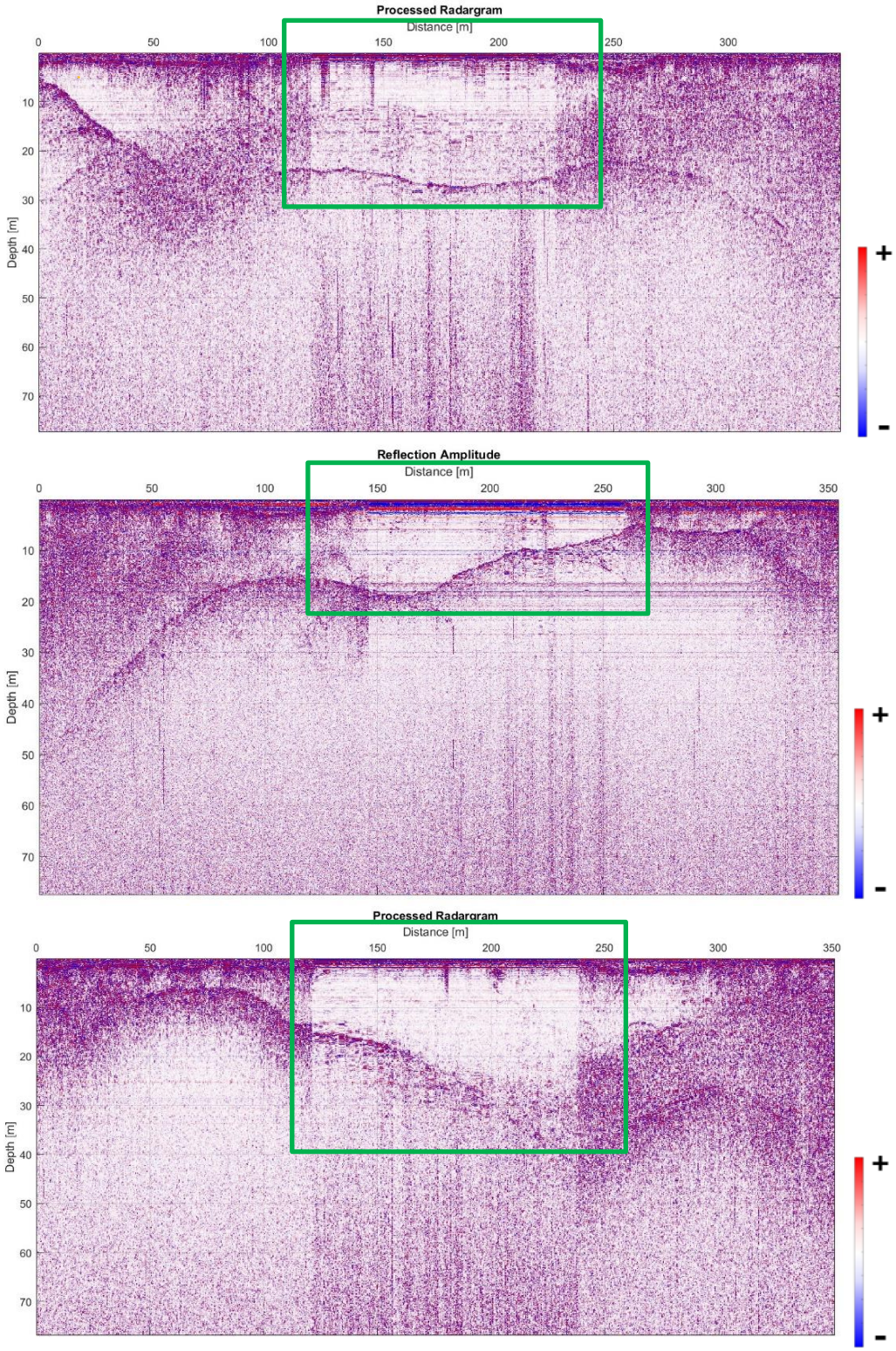

Figure 61 - Reflection amplitude of profile 2 (top), 3 (middle), 4 (bottom) - Rutor

Inside the rectangles is highlighted a zone exhibiting the same features in all three profiles: an abrupt jump in the signal both on the left and on the right of the rectangle is clearly evident, especially in profiles 2 and 4. This sudden

response is to be attributed to the operator behavior: the antenna has probably been raised to avoid obstacles, most likely the moraine itself.
Afterwards, it is worth noting that the GPR survey has been conducted in the summer period, which can be a valid explanation for the large amount of diffuse scattering at the beginning of profiles 3 (from 0 to a distance of about 150 m) and 4 (from 0 to about 125 m). When comparing the radargrams with the line orientations in Figure 16, it is evident that these distances correspond to what is supposed to be the snow layer covering the glacier, which, due to the relatively warmer period of the year, will likely contain meltwater.
It is also worth mentioning that the different water contents are linked to various thermal regimes (Gutgesell & Forte, 2024) which can explain the widely spread scattering. Moreover, we already know that whenever the "warm" ice is not clean and includes some debris material embedded in it, the result will be a more disturbed signal when the EM wave hits the different media with contrasting properties.
The attribute analysis is in this specific case essential for a better interpretation of the GPR display and will aim to define what hypothesis concerning the moraine fits more efficiently the radargrams obtained.

From the study of the time derivative of instantaneous amplitude for the three profiles, the interface between the snow pack on top and the material below is highlighted:

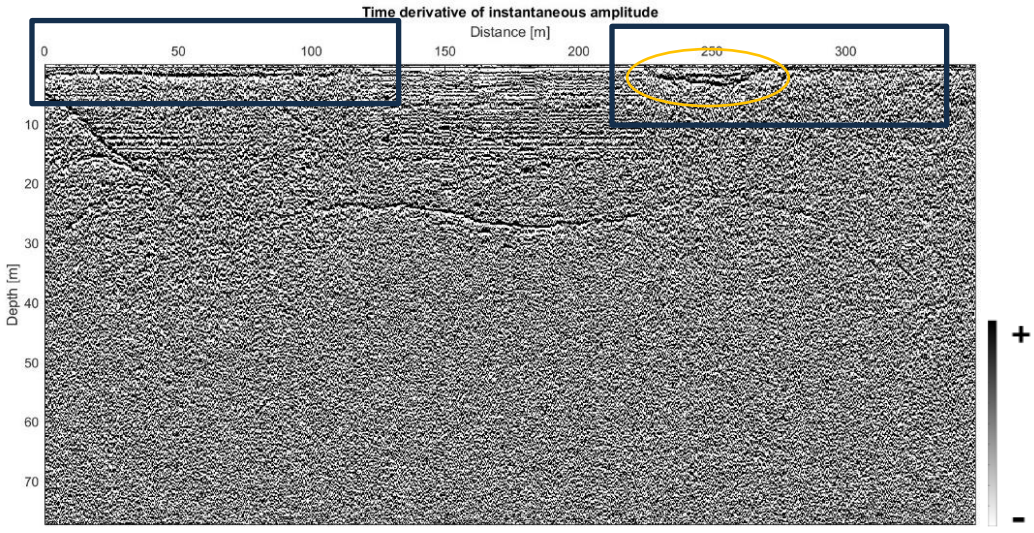

Figure 62 - - Time derivative of instantaneous amplitude for profiles 2 (Rutor)

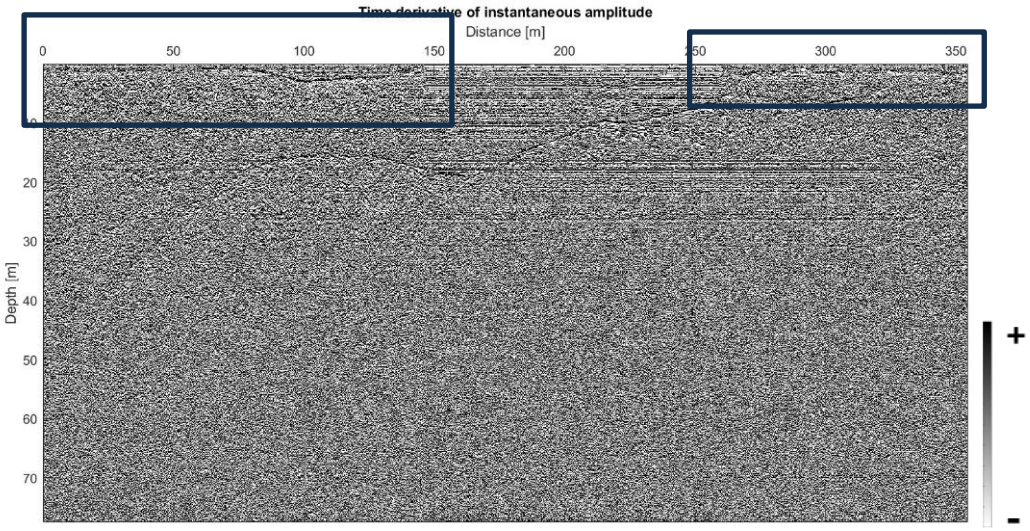

Figure 63 - - Time derivative of instantaneous amplitude for profiles 3 (Rutor)

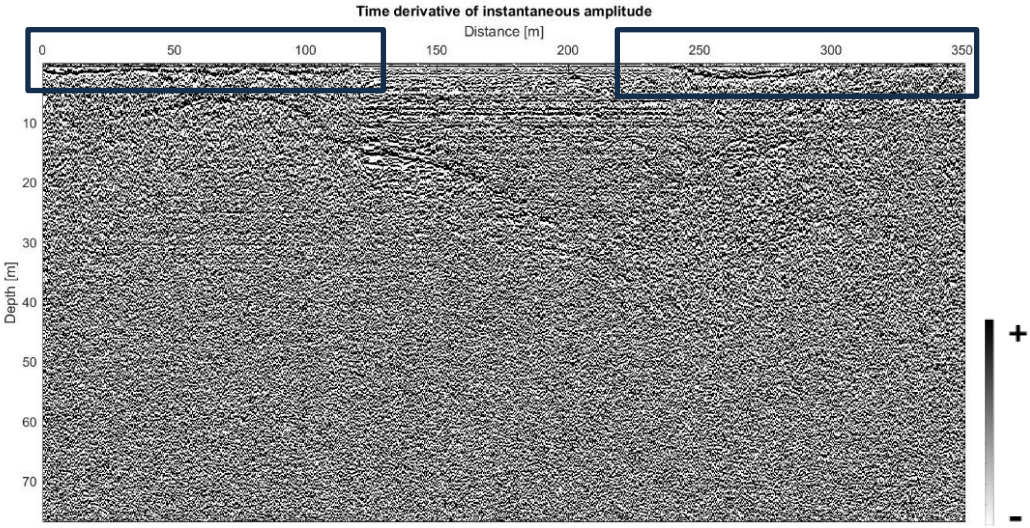

Figure 64 - Time derivative of instantaneous amplitude for profiles 4 (Rutor)

Some useful information is already provided to us: it appears that the interface between snow and ice is heavily marked in the time derivative of instantaneous amplitude display. Probably, accumulations of snow are the concave profiles in the circle.

Considering the response of the signal in the different zones of the radargram, it can be noted that the material in the central part, i.e. where the moraine was encountered during the GPR survey, appears as a transparent facies, typical of pure cold ice. If the moraine was located below the surface of the glacier, the image would be disturbed by the scattering caused by the debris; since this feature is not found, we can state that it actually "sits" on top of the glacier, acting as a "cap" insulating the underlying material and delaying the melting. This feature results in a warmer ice full of free water on the sides and a colder type below the strip of glacial debris, which, according to the reflection

amplitude profiles and the time derivative of instantaneous amplitude, is very shallow (around 1 meter).

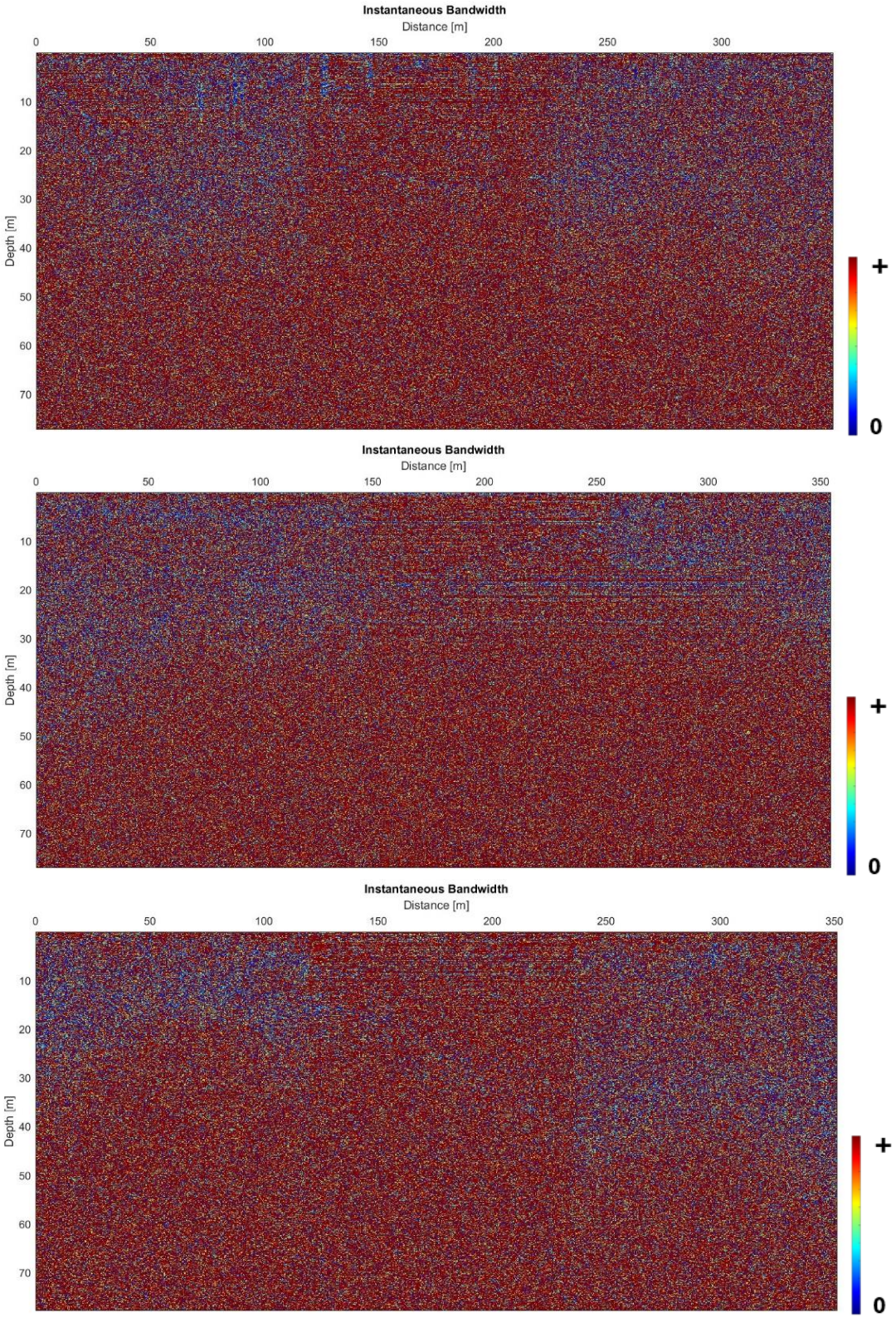

Figure 65 - Instantaneous bandwidth of profile 2 (top), 3 (middle), 4 (bottom) - Rutor

According to the information found in the literature and as already stated, when the instantaneous bandwidth values shrink, it means a certain amount of water is present. This hypothesis could stand and agree with what was stated previously: the temperate glacier contains meltwaters; moreover, the summer period certainly contributes in the fusion of the ice as the top layer is no longer frozen and does not insulate properly the layers below. This will lead to a further fusion process.
Such explanation can support the theory of warm ice on the sides of the moraine.

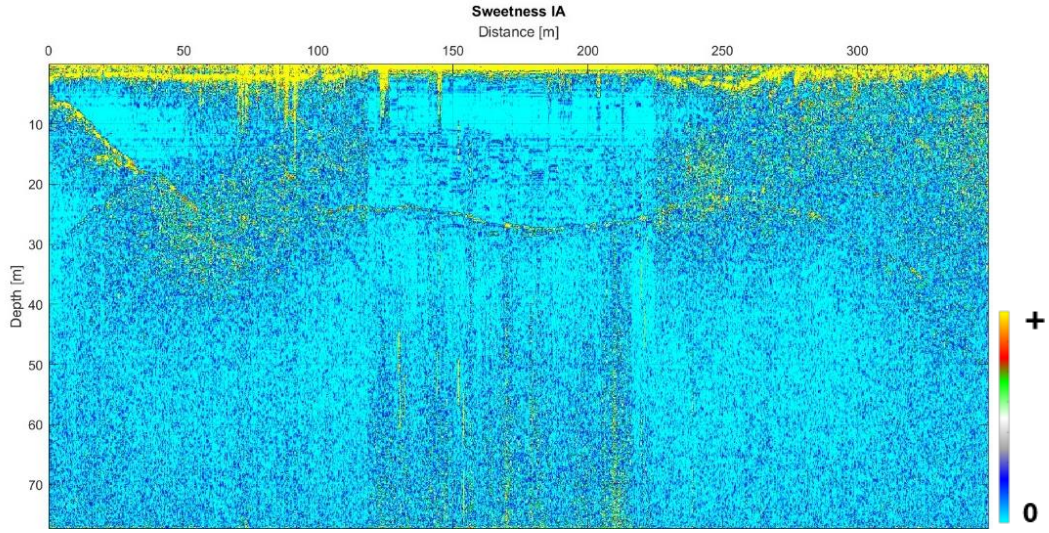

Figure 66 - Sweetness of profile 2 (Rutor)

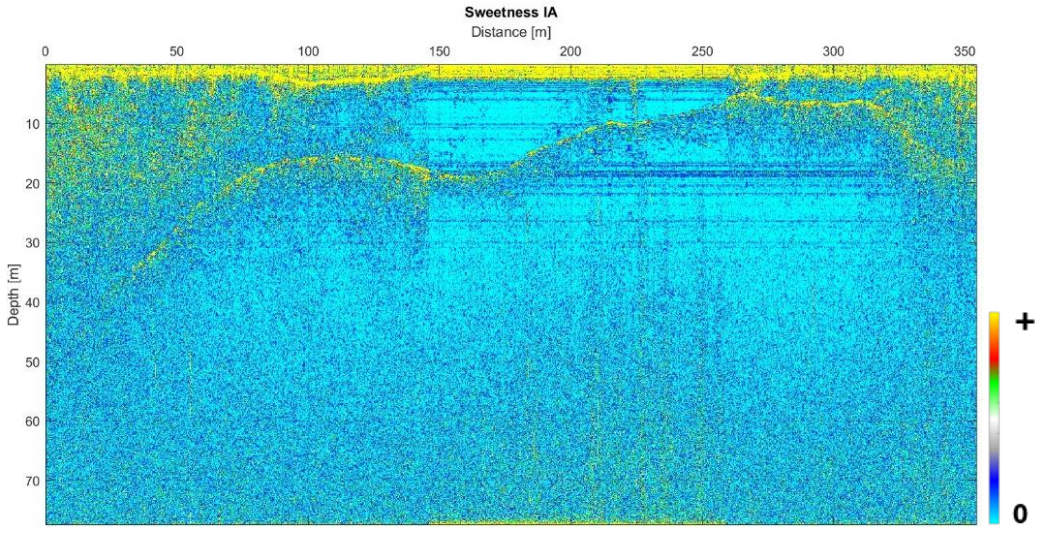

Figure 67 - Sweetness of profile 3 (Rutor)

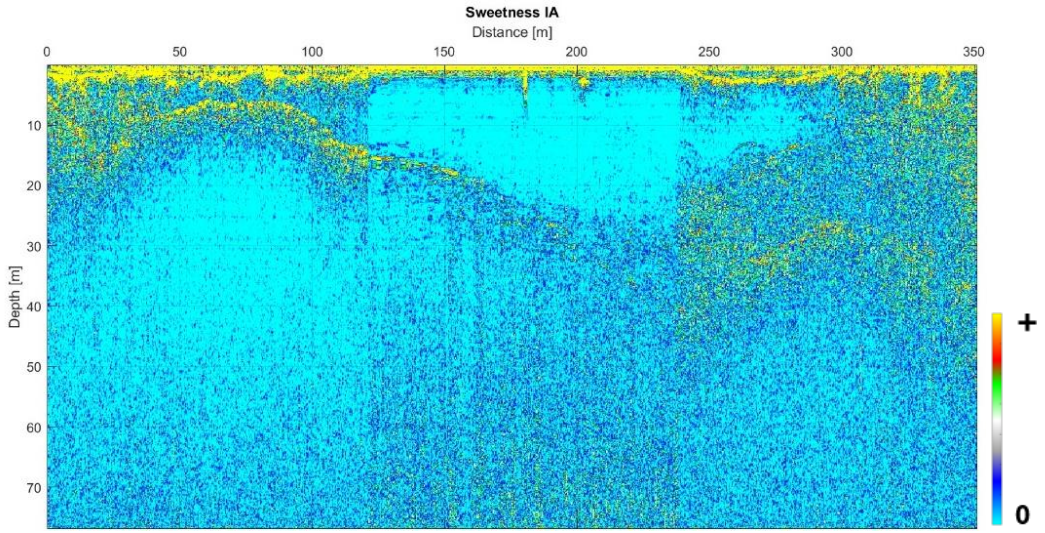

Figure 68 - Sweetness of profile 4 (Rutor)

The sweetness displays show higher values in the zones assumed as warm ice, thus confirming the original assumption of a discrete amount of meltwater accumulated in the ice.

The layers of snow on top of the radargram are correctly characterized by fairly elevated values, validated also by the warmer period of the year making snow more liquid. The sweetness attribute is able to depict the moraine on top, characterized, as we already mentioned, by sediments with a different structure when compared to the cold ice below, showing in turn very low values.

As already mentioned for other displays, the high sweetness near the bottom gives the impression of being the outcome of a difference in temperature between the bedrock and the medium above: the stress-strain rate resulting from the interplay between the two materials leads to a heat effect (Gutgesell & Forte, 2024) which is the cause of the diffuse scattering and possibly brings to a further and more rapid melting of the layer of ice at the interface. In fact, a clear example is profile 2 where the cold ice at the center (below the moraine) is characterized by a strip of mild disturbance in the proximity of the bedrock. We translate this behavior as the heat coming from the bottom which progressively melts the ice.

Concerning the bedrock, it is visibly delineated in the reflection amplitude displays and confirmed in the time derivative of reflection amplitude.

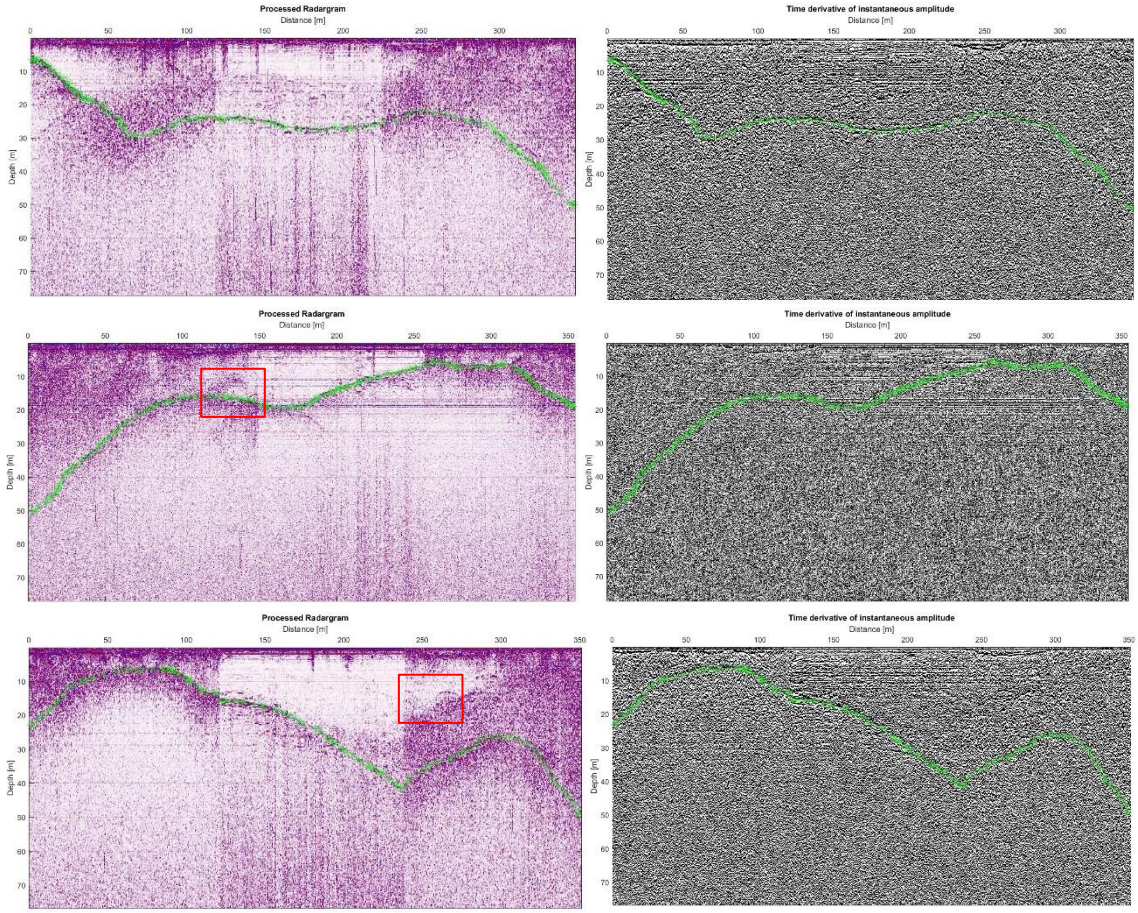

Figure 69 – Bedrock marked in green and hyperbolas identification (red rectangle): profile 2 (top), profile 3 (middle), Profile 4 (bottom) - Rutor

Lastly, hyperbolas are outlined in profile 3 and 4.
In the first case, it concerns an englacial cavity due to its location near the bedrock, most likely the result of the undercutting process caused by englacial water; the second case is more peculiar: according to the location, they may be related to the presence of pebbles and debris of rather large size embedded in the warm ice, or they could be internal fractures.

5.3.3 Profiles 5 and 6

Profiles 5 and 6 are rather perpendicular lines and do not cross the moraine. We are going to analyze them together for the similarities they illustrate: rather shallow depth and significant amount of scattering.

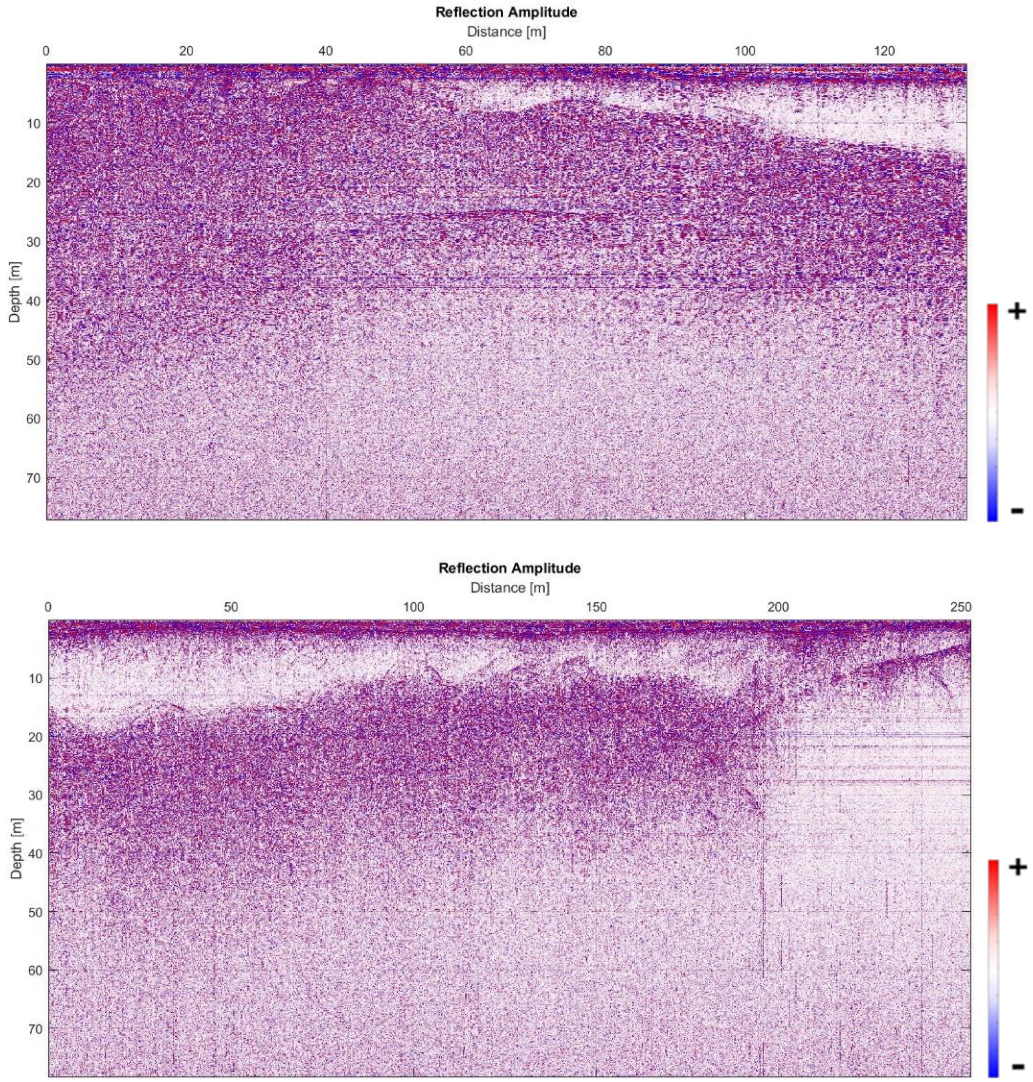

Figure 70 - Reflection amplitude- Profiles 5 (top) and 6 (bottom) - Rutor

They are characterized by a homogenous snow cover on top, cold ice zones of varying thickness, and high scattering preventing a correct and complete detection of the bedrock.
Profile 6 also presents diffraction hyperbolas already visible in the reflection amplitude image, which are going to be addressed further on in the chapter.

Starting the attribute analysis from the time derivative of instantaneous amplitude, the upper layer of profile 5 shows several patterns such as snow accumulations and hyperbolas, which were not immediately evident in the reflection amplitude.

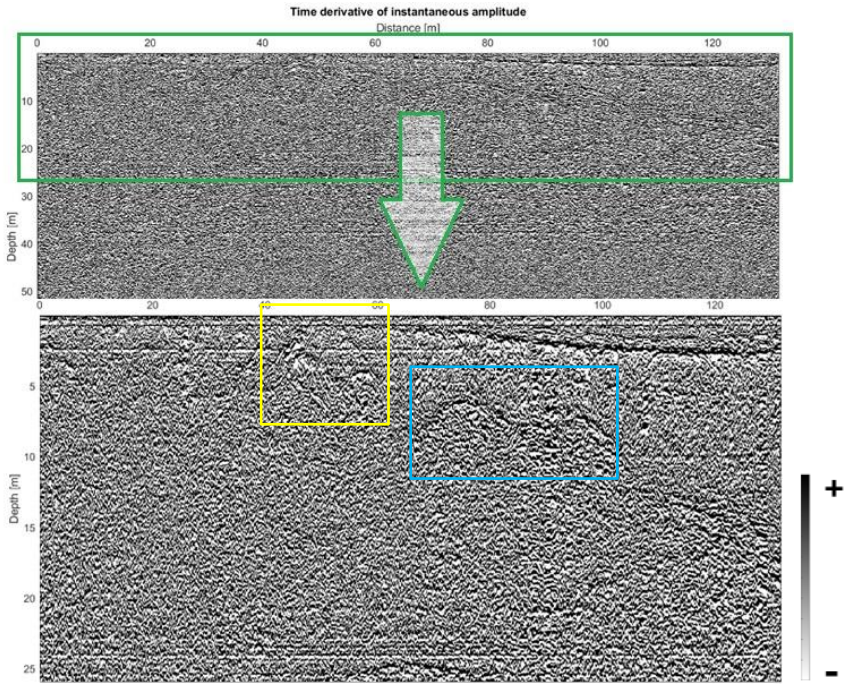

Figure 71 - Time derivative of instantaneous amplitude with close up on the top of the section – Profile 5 (Rutor)

The layer of snow on top of the glacier is mostly evident at the end of the line, with an accumulation zone between the distances of 80 and 130 meters. Moreover, several hyperbolas emerge: inside the yellow rectangle, crevasses are most likely highlighted, due to their vertical shape perpendicular to the extension of the line.

Inside the blue rectangle are probably cavities; whether they are filled with water or empty is what is going to be assessed in the sweetness profile, even if the high scattering in that area already gives a suggestion of meltwater infiltrating inside the fractures.

These hyperbolas, especially those related to the crevasses, were also detected to a certain extent by the cosine of instantaneous phase:

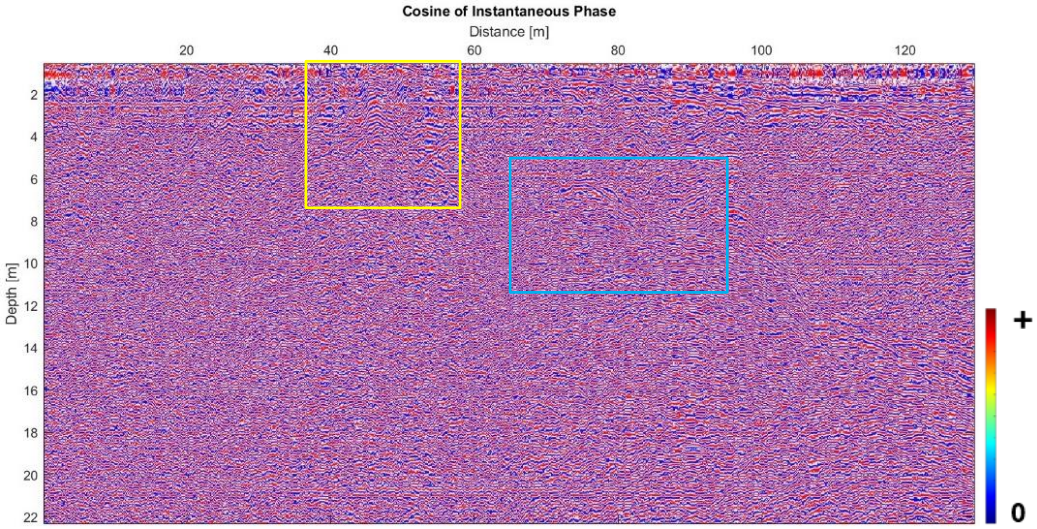

Figure 72 - cosine of instantaneous phase close up to the hyperbolas – Profile 5 (Rutor)

Once again the sweetness attribute confirms that we are investigating a section with very melted ice conditions at the beginning of the GPR section and a rather cold but shallow area starting from the middle.

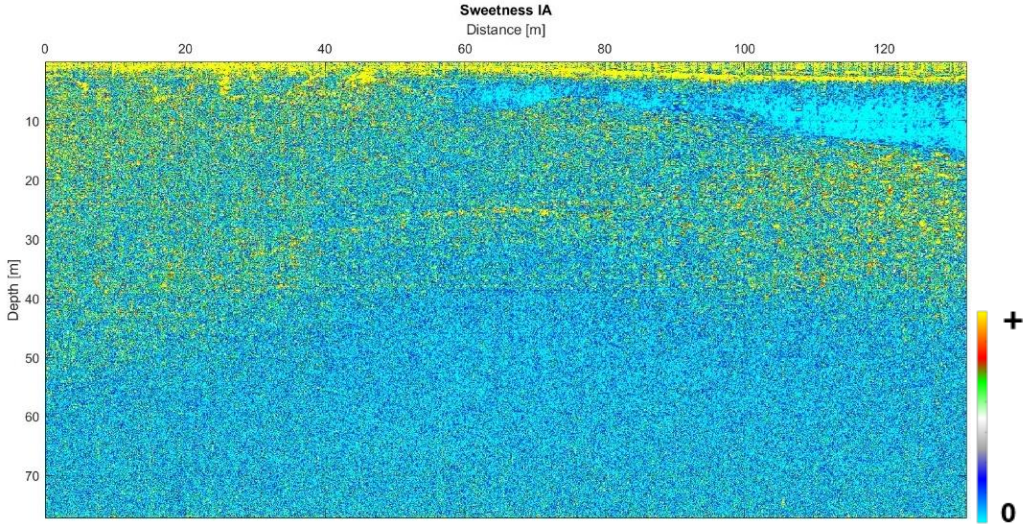

Figure 73 – Sweeness – Profile 5 (Rutor)

The hyperbolas in profile 6 are not evident in the time derivative of instantaneous amplitude, although they are clearly visible in the instantaneous amplitude:

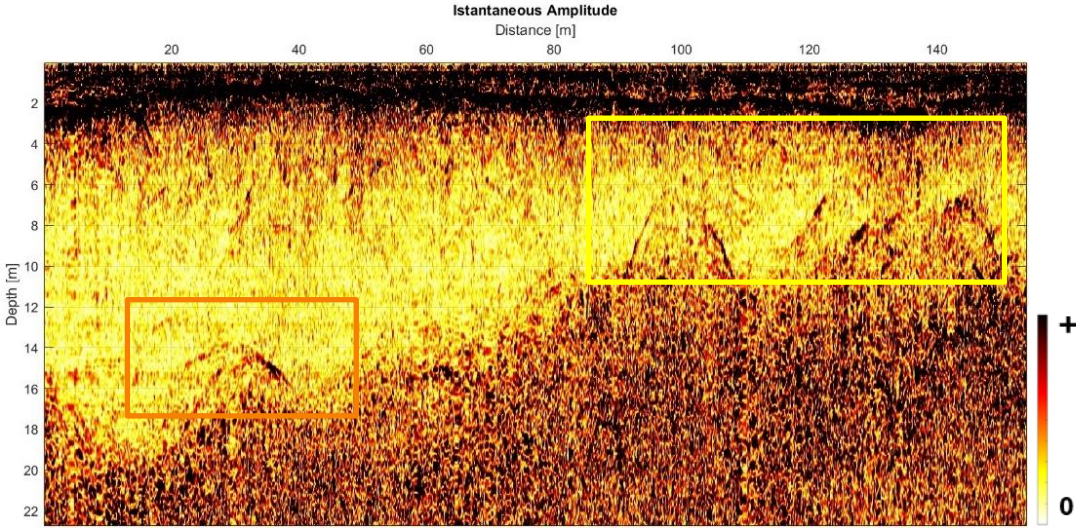

Figure 74 - Instantaneous amplitude, close-up on the diffraction hyperbolas – Profile 6 (Rutor)

Inside the orange rectangle is a cavity with a certain free water content; the yellow rectangle highlights on the other hand a series of fractures close to the surface in which water from the top flows down toward the bedrock.

According to Godio and Franco (2024), the velocity associated to the hyperbolas is 0.17 m/ns, i.e. the speed of the EM wave in ice, thus supporting the assumption of fractures in the frozen material.

Once again the presence of holes in the glacier explains the high level of disturbance in the signal as it is attenuated by the high conductivity of water.

The sweetness display confirms the theory.

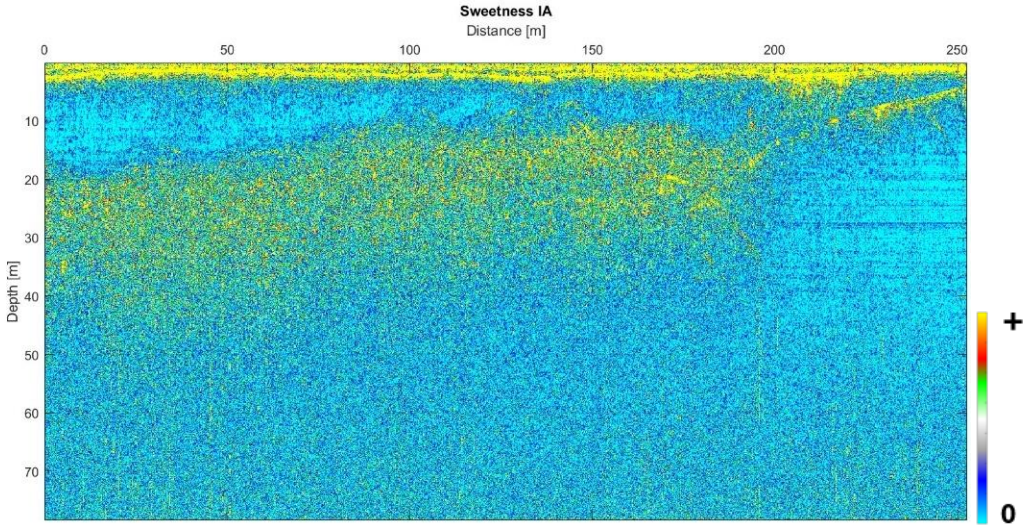

Figure 75 - Sweeness – Profile 6 (Rutor)

Same as profile 5, a cold ice pattern appears from the radargrams. Probably, considering the orientation of the two lines, some sediments from the moraine lie underneath the layer of snow visible on the satellite image (Figure 16) and contribute in insulating the ice below.

Unfortunately, no attribute was capable to pick the interface between bedrock and ice properly: in profile 5, a small part emerges at a depth of 30 meters, but no other portion is detected, whereas the end of the bedrock is quite evident in n° 6.

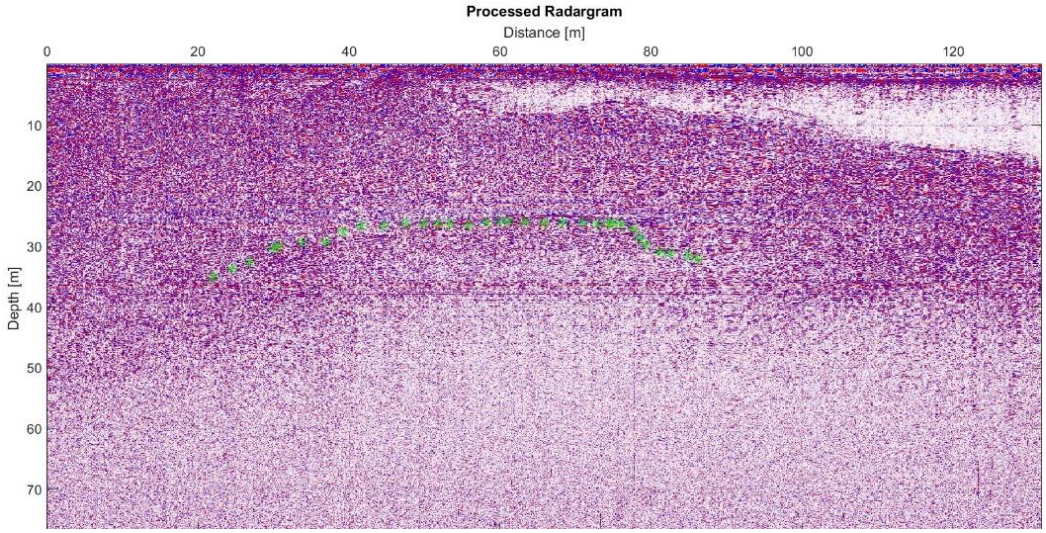

Figure 76 - Bedrock picking – Profile 5 (Rutor)

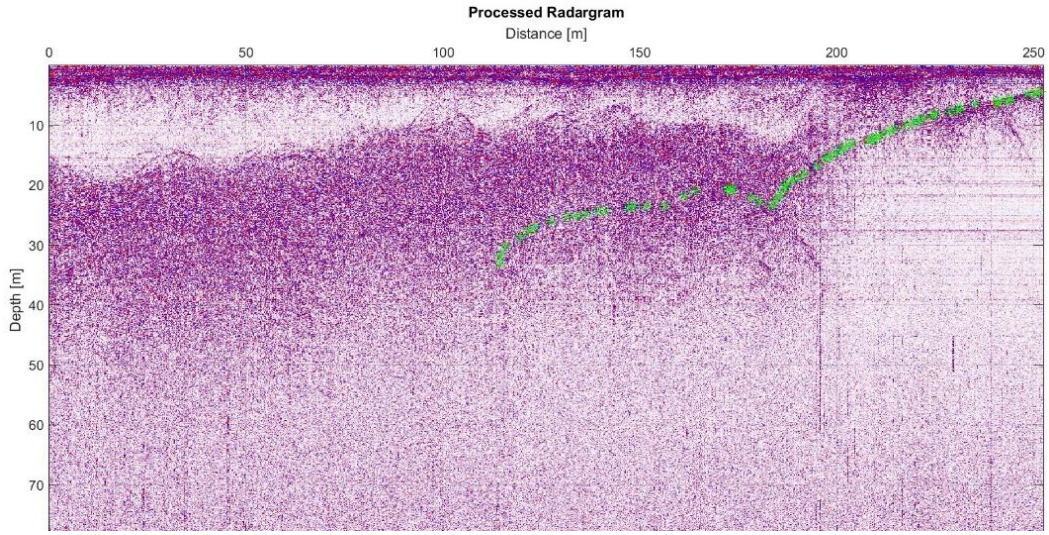

Figure 77 – Bedrock picking – Profile 6 (Rutor)

5.4 Statistical analysis

Following the example of Gutgesell and Forte (2024), a statistical analysis was carried out for both Indren and Rutor glaciers, aimed at more accurately and quantitatively classifying the different zones inside a radargram.

For the sake of simplicity, the mean and standard deviation of four areas were calculated on one single profile per glacier in the results of instantaneous amplitude, instantaneous bandwidth, and sweetness.

The parameters were calculated inside certain polygons properly drawn according to the hypothesis formulated in the attribute analysis.

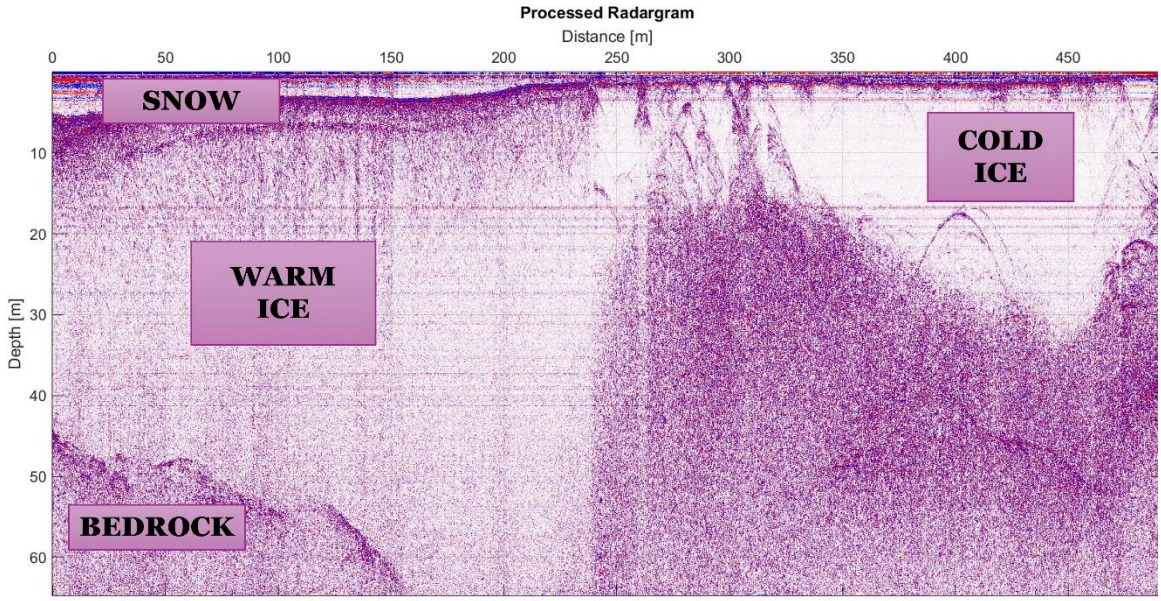

Figure 78 - Different zones where the statistical parameters have been computed. The figure represents profile 12 on the Indren glacier

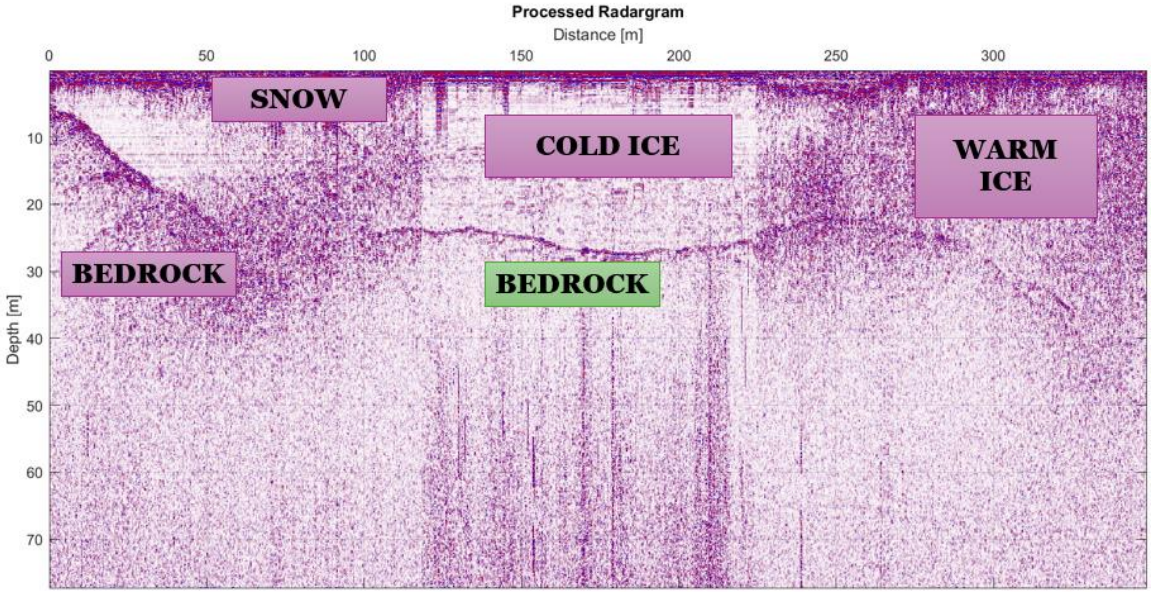

Figure 79 - Different zones where the statistical parameters have been computed. The figure represents profile 2 on the Rutor glacier.

The zones of interest were analyzed on the following Indren and Rutor displays.

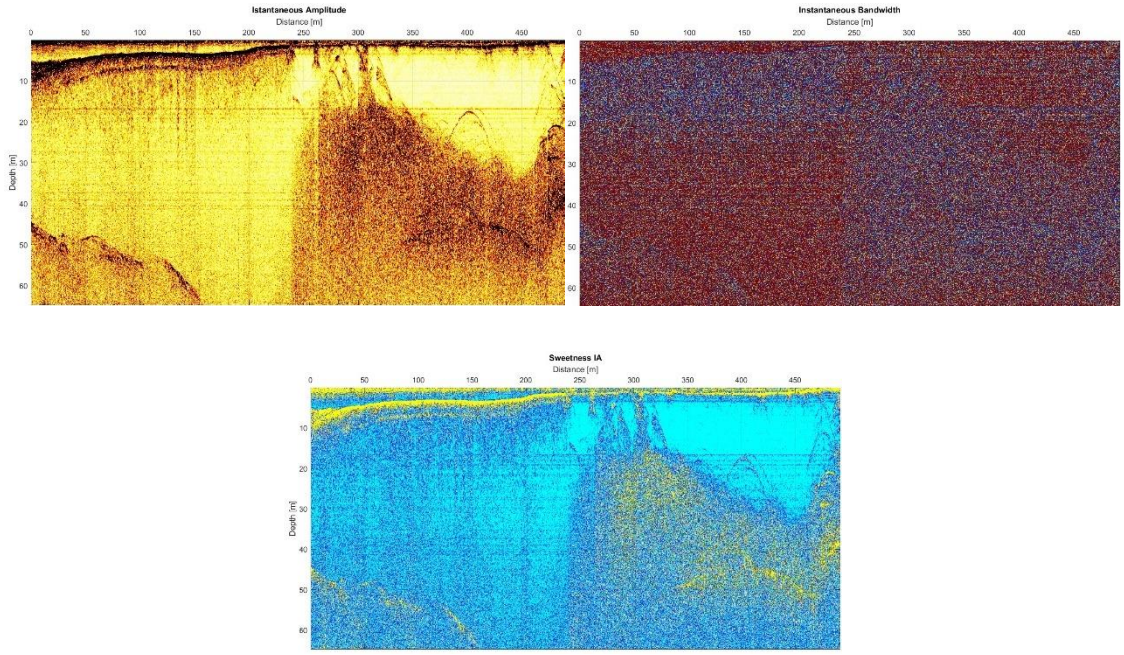

Figure 80 - Indren glacier, profile 12. Instantaneous amplitude (top-left), instantaneous bandwidth (top-right), sweetness (bottom)

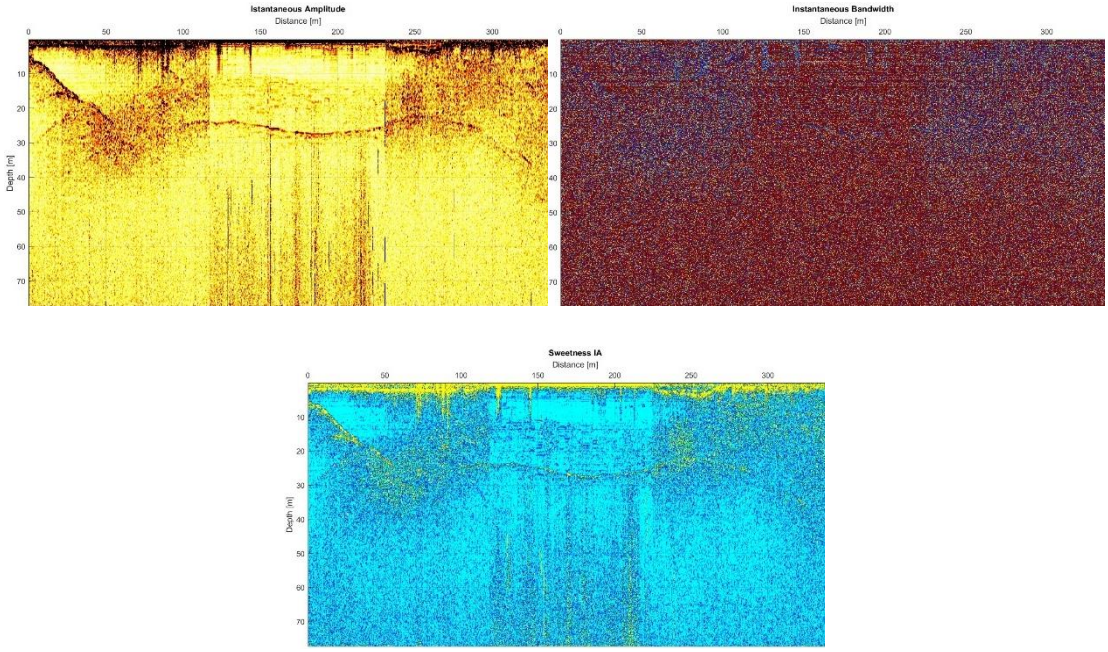

Figure 81 - Rutor glacier, profile 2. Instantaneous amplitude (top-left), instantaneous bandwidth (top-right), sweetness (bottom)

The results obtained are reported in the tables below.

Table 10 - Mean and standard deviation of four zones inside the glacier based on the features identified in profile 12 – Indren glacier

INDREN			
MEAN			
	Instantaneous Amplitude [-]	Instantaneous Bandwidth [Hz]	Sweetness [$Hz^{-1/2}$]
Cold ice	0.081	1.653e18	4.858e-06
Warm ice	0.288	1.555e18	1.676e-05
Bedrock	0.393	1.589e18	2.503e-05
Snow	2.081	1.650e18	1.173e-04

INDREN			
STANDARD DEVIATION			
	Instantaneous Amplitude [-]	Instantaneous Bandwidth [Hz]	Sweetness [$Hz^{-1/2}$]
Cold ice	0.046	2.702e+18	4.289e-06
Warm ice	0.170	2.689e+18	1.253e-05
Bedrock	0.230	2.646e+18	3.619e-05
Snow	1.976	2.754e+18	1.618e-04

The results follow a certain trend; moreover, the values of instantaneous amplitude and sweetness regarding the cold ice zone are compliant with those obtained by Gutgesell and Forte: the mean is the lowest; however, in contrast to what reported in the paper, in our case the second lowest mean value is obtained for warm ice, followed by the rocky material of the bedrock. From the figure we can tell that the area marked as a warm ice zone does contain a certain amount of melted ice given the higher scattering if compared to the cold ice area, nevertheless relatively transparent frozen regions are still found. We have no way to compare the results of the instantaneous bandwidth and of snow in general. Nonetheless, we can observe that snow is the medium giving the highest results in terms of both amplitude and sweetness.
Instantaneous bandwidth presents values too similar between the different materials and does not seem to provide any remarkable information for discrimination.

Table 11 - Mean and standard deviation of four zones inside the glacier based on the features identified in profile 2 – Rutor glacier

RUTOR			
MEAN			
	Instantaneous Amplitude [-]	Instantaneous Bandwidth [Hz]	Sweetness [$Hz^{-1/2}$]
Cold ice	0.198	1.054e+18	1.203e-05
Warm ice	0.455	1.058e+18	2.606e-05
Bedrock	0.540	1.058e+18	3.065e-05
Snow	1.616	1.026e+18	9.241e-05

RUTOR			
STANDARD DEVIATION			
	Instantaneous Amplitude [-]	Instantaneous Bandwidth [Hz]	Sweetness [$Hz^{-1/2}$]
Cold ice	0.120	1.323e+18	1.076e-05
Warm ice	0.260	1.336e+18	3.326e-05
Bedrock	0.353	1.336e+18	2.446e-05
Snow	1.440	1.329e+18	8.824e-05

For the Rutor glacier two different computations were made. As a matter of fact, the mean value of the bedrock (in purple) results higher than that of the warm ice. This can be explained if considering the area where the polygon was drawn: it is evident that a certain amount of water disturbs the signal both on the left and right side of the cold ice below the moraine. When calculating the

mean value on the bedrock (in green) below the transparent ice insulated by the moraine on top (Table 12), the result suggests a material similar to the ice itself: we can state that this behavior is probably related to frozen debris.

Table 12 - Mean and standard deviation of profile 2, Rutor glacier, calculated below the layer of cold ice covered by the moraine

MEAN			
	Instantaneous Amplitude [-]	Instantaneous Bandwidth [Hz]	Sweetness [$Hz^{-1/2}$]
Bedrock	0.246	1.001e+18	1.670e-05

STANDARD DEVIATION			
	Instantaneous Amplitude [-]	Instantaneous Bandwidth [Hz]	Sweetness [$Hz^{-1/2}$]
Bedrock	0.309	1.290e+18	3.105e-05

Nevertheless, the values of standard deviation are significantly high in all cases, suggesting the presence of a large variability in the behavior of the attributes and the absence of areas characterized by a high degree of homogeneity where it is possible to perform a good estimation.

A deeper analysis of other statistical parameters involving more profiles and the detection of potential outliers is suggested for a better comprehension of the results.

6 Discussion and conclusions

The aim of the current chapter is to provide a summary of the results obtained on the different profiles of Indren and Rutor glaciers, through a classification that considers the features extracted from the attribute analysis.

Overall, the instantaneous- and frequency-related attributes were able to return additional information which helped the interpretation of the GPR survey. The instantaneous amplitude was able to highlight and emphasize strata between different media characterized by a varying lithology, water content or impurities embedded in the ice, and identify the presence of fractures, as well as cavities, and crevasses. Evident representations are given by:

- Indren - profile 9, where snow accumulations returned higher amplitude values in contrast with the cold underlying ice facies; all cavities and pebbles were significantly marked by diffraction hyperbolas.
- Indren – profile 10, with evident bedrock morphology and fractures highlighted by the diffraction hyperbola.
- Indren – profile 12, in which crevasses are clearly identifiable via high amplitude series of hyperbolas.

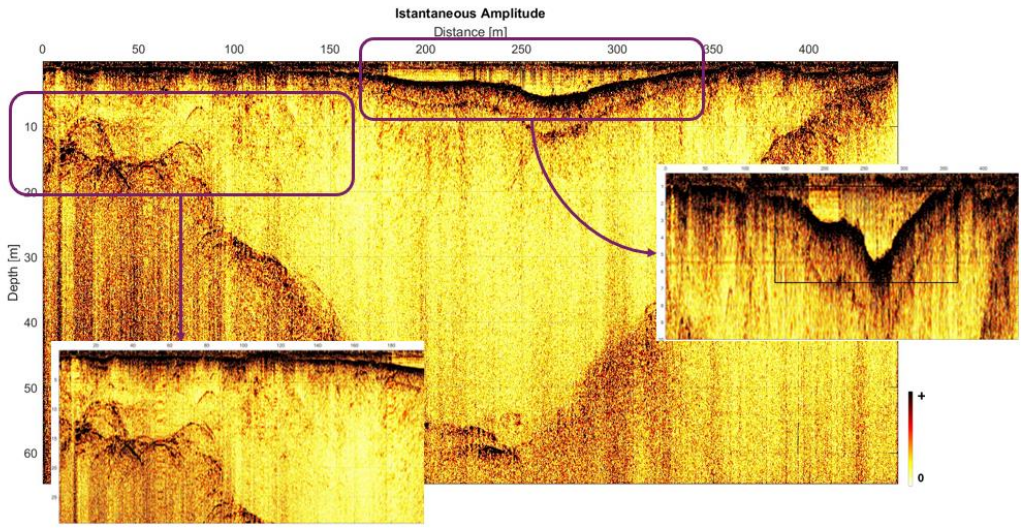

Figure 82 - - Instantaneous amplitude – Indren: profile 9. Close-ups on the features highlighted by the attribute response

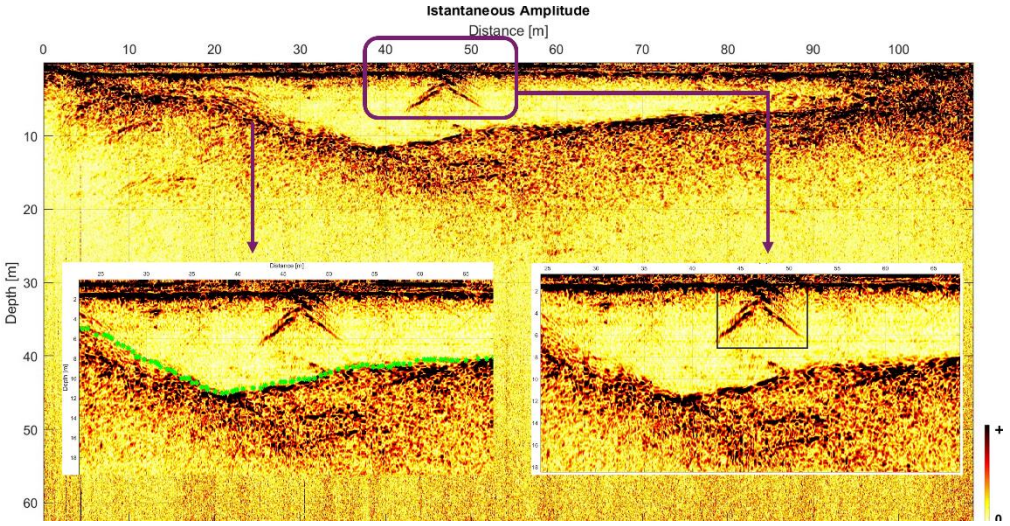

Figure 83 - Instantaneous amplitude – Indren: profile 10. Close-ups on the features highlighted by the attribute response

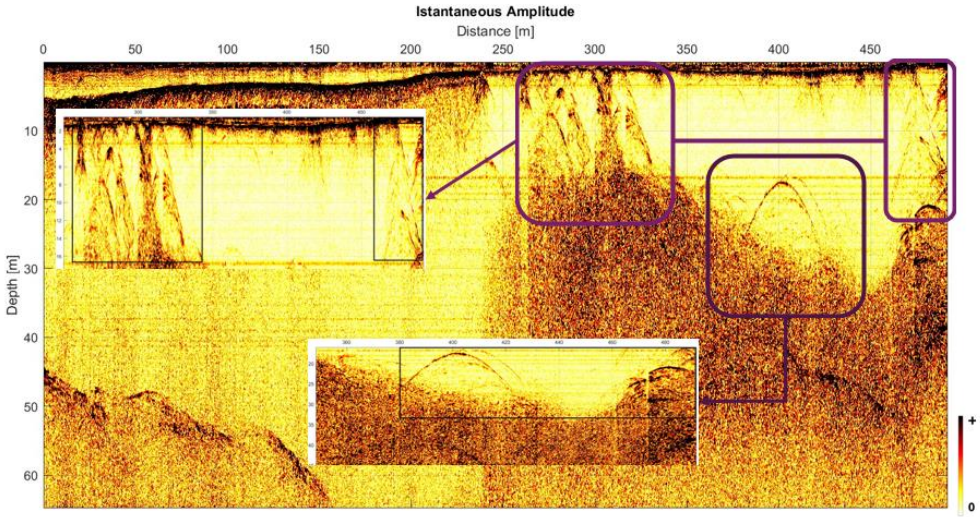

Figure 84 - Instantaneous amplitude – Indren: profile 12. Close-ups on the features highlighted by the attribute response

- Rutor, profile 6 has several hyperbolas identifying fractures and crevasses inside the glacier. Moreover, the bedrock interface is evident on the right, together with a feature that might be due to a rather large rock on the bottom for its shape connected to the curve of the bedrock.

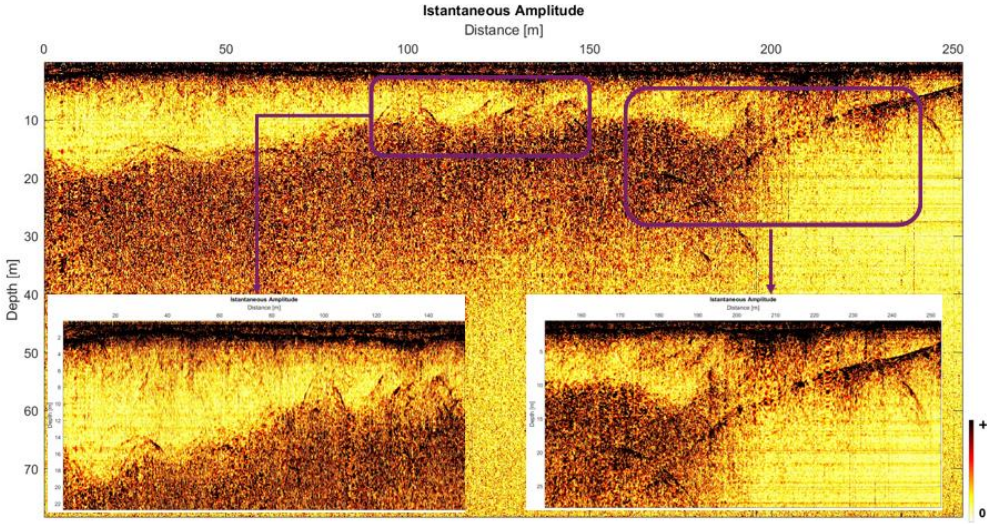

Figure 85 - Instantaneous amplitude – Rutor: profile 6. Close-ups on the features highlighted by the attribute response

The interfaces between snow and ice/ice and bedrock, mounds of snow, and all fracture or cavity inside the ice body are often depicted by two other attributes: cosine of instantaneous phase and time derivative of instantaneous amplitude.

- Indren – profile 9 and 12 show several artifacts, such as snow accumulations and hyperbolas which are well depicted by the cosine of instantaneous phase.
- Rutor – profile 2, where the time derivative of instantaneous amplitude emphasizes the snow layer on top of the section and the bedrock outline.

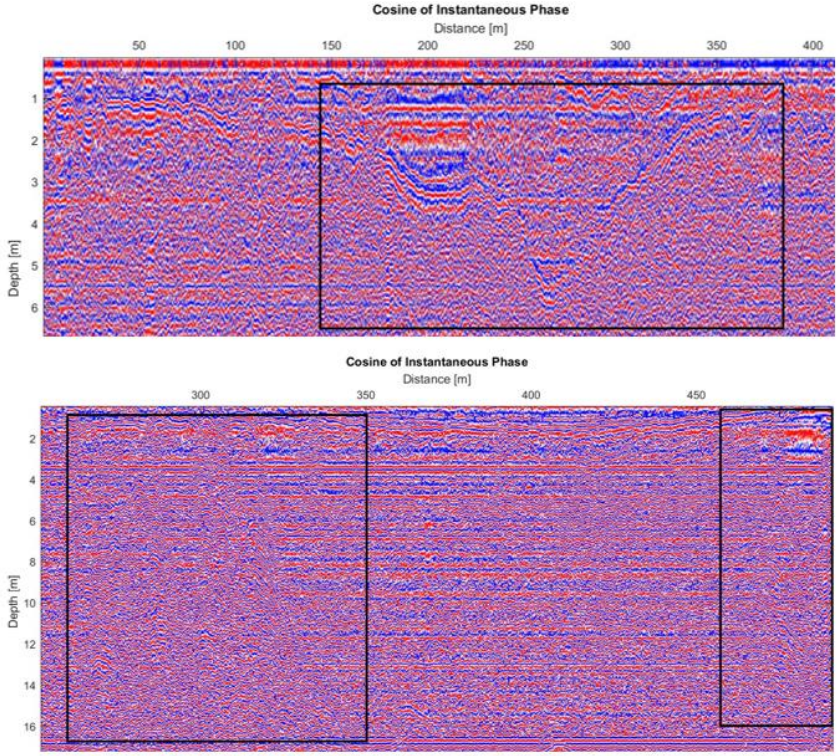

Figure 86 – Close-ups of the cosine of instantaneous phase, profiles 9 above and 12 below (Indren): artifacts highlights

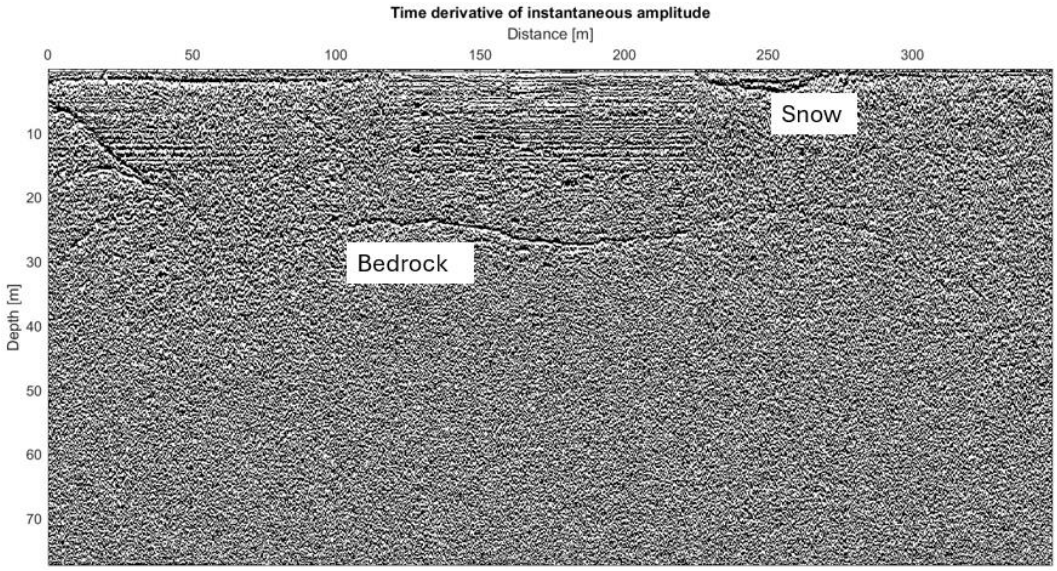

Figure 87 - Time derivative of instantaneous amplitude of profile 2 (Rutor)

Lastly, about the characterization of the water content, three attributes were found to be effective in this regard: instantaneous bandwidth, often coupled with dominant frequency for an overall visualization of the possible areas filled with a certain amount of water, and sweetness for a deeper understanding of the quantity.

- Indren - profile 1, where an intense scattering is visible in the instantaneous bandwidth display along the whole profile, suggesting the presence of warm ice and a high water content. The sweetness profile confirms the wet nature of the glacier bed and emphasizes the thermal anomaly characterizing the bedrock.
- Indren – profile 9 is a line where the dominant frequency was plotted successfully without showing an excessive level of noise. In this case, both instantaneous bandwidth and dominant frequency showed a sharp variation in the frequencies linked once again to the free water layer in the proximity of the bedrock and to the superficial snow cover; hypothesis confirmed by the sweetness display, despite portraying also a strong disturbance in the bottom-left zone.
- Indren – profile 12, where the water infiltrating from the fractures and crevasses near the surface is correctly depicted in both displays, although the sweetness is also capable of capturing the difference in temperature of the small part of bedrock Figure 88 c.

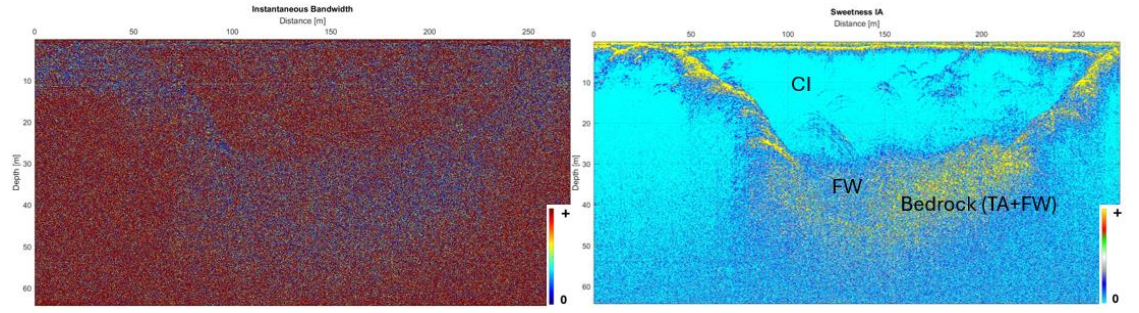

a)

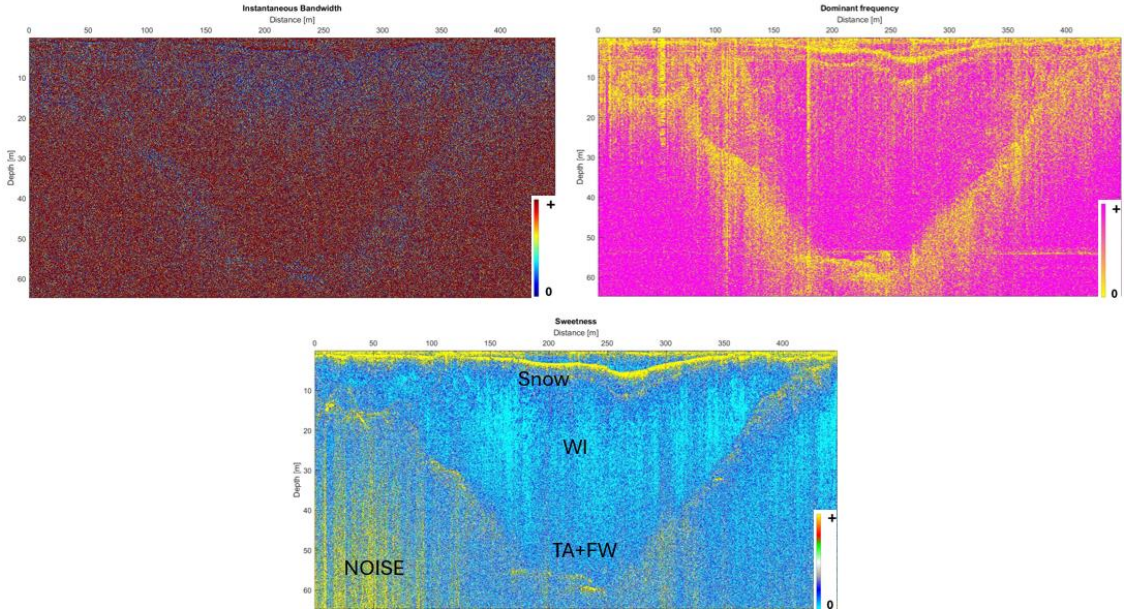

b)

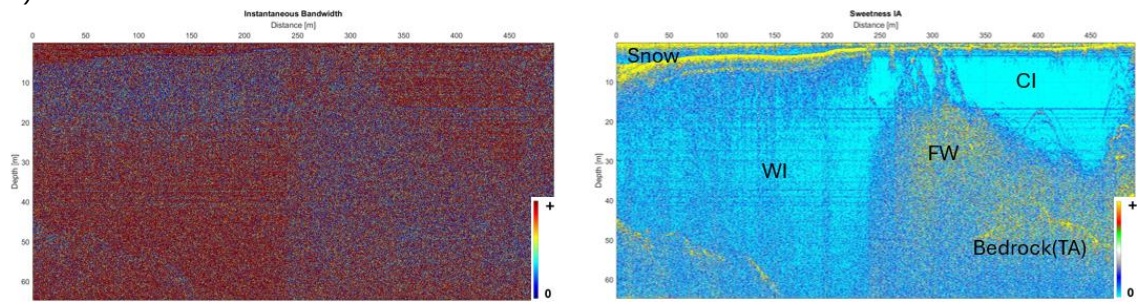

c)

Figure 88 - Instantaneous bandwidth, dominant frequency (profile 9), and sweetness for profile 1 (a),9 (b),12 (c) – Indren glacier. CI: cold ice, WI: warm ice, FW: free water, TA: thermal anomaly

- Rutor – profile 2, where on the instantaneous bandwidth display, the cold ice below the moraine is clearly shown in red (higher frequencies), whereas the areas of warm ice (therefore including free water) have lower values. The same results are translated into the sweetness section with more details: the bedrock is occasionally portrayed by higher values of sweetness accounted for the temperature difference with respect to ice (TA) and free water contents; the wet snow cover is emphasized at

the top and the cold ice below the moraine is represented with the lowest values.

- Rutor – profile 6 is another example of bedrock with water causing a rather high scattering phenomenon; once again the heat of the bottom is visible, together with cold and warm ice zones.

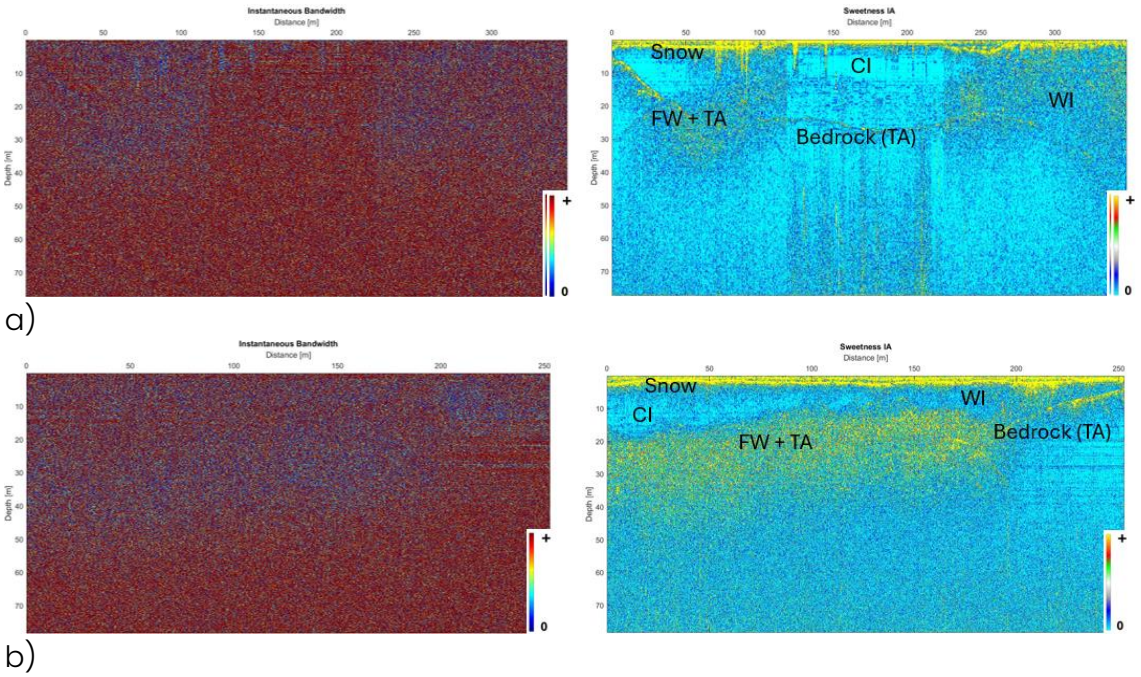

Figure 89 - Instantaneous bandwidth and sweetness for profile 2 (a), and 6 (b) – Rutor glacier. CI: cold ice, WI: warm ice, FW: free water, TA: thermal anomaly

Overall, we can state that both instantaneous bandwidth and dominant frequency managed correctly to depict the difference in water content and temperature of the media intersected by the signal; however, the sweetness display will then provide a clearer vision of what could be water and what is more likely a thermal anomaly.

We can assess that the attribute analysis was overall successful in emphasizing features that are not readily apparent on the processed GPR results in terms of amplitude of reflection only. Moreover, they helped identify artifacts, different media, and the varying temperatures characterizing both ice and bedrock.

It is possible to state that the amount of water inside both glaciers is significantly high, especially for the Rutor glacier, where the difference between the warm ice around the moraine and the cold ice below the capping debris is strongly marked.

This water content can surely be related to the summer season with the meltwater infiltrating in the fractures (profile 12 is an example); however, the

snow cover should work as an insulating layer delaying the process below and, with its brightness, it increases the albedo working as a thermal barrier. On the other hand, the raise in temperatures and a reduced snow cover will speed up the mass loss [8].
It is therefore important and essential to carry out GPR surveys supported by the attribute analysis to monitor the health of the glaciers and prevent any possible dangerous situations resulting from a changing environment.

7 Further investigation

GPR attribute analysis in glaciology has proven to be efficient to a good extent. However, further research is necessary to fully assess the validity of the results and provide additional information.

Firstly, surveys involving more consecutive profiles could be useful to visualize the continuity of certain patterns for a more complete investigation: these lines could help identify whether the peculiar features represented on the radargrams stem from a common artifact inside the glacier (fracture, cavity, sediments, thermal anomalies, etc.), if they are the result of a disturbed signal due to the presence of meltwater and other conductive media or if they are simply random noise.

Another option to increase the accuracy of the results obtained is to couple the use of specific software to the processed data on Matlab for further support to the analysis. For instance, with ReflexW it is possible to compute the slope of diffraction hyperbolas and find the velocity to confirm or refute the assumptions made.

Furthermore, other attributes can be implemented to improve the research: textural attributes, such as entropy, homogeneity, chaos, contrast, and cluster, offer a finer result concerning the imaging of discontinuities and the definition of the different materials according to mutually connected entities (Zhao et al., 2016).

The statistical analysis can be refined and enhanced by computing the selected parameters on a larger number of zones of interest, for wider areas, involving more profiles and attributes for a more precise investigation.

Moreover, in case of obstacles difficult to overcome or areas not easily accessible, like moraines, drone-mounted GPR surveys are an option. Although other issues such as the attenuation of the signal in air, the decreased resolution and investigation depth, drone stability arise.

Finally, photogrammetric surveys are another way of improving the interpretation of glaciers behavior by monitoring their movement, retreat processes, and through the use of thermal infrared cameras, which manage to measure important parameters such as the temperature of the snow cover, of the glacier surface, and the thickness of the layer of sediments (Messmer & Groos, 2024).

From the perspective of climate change, this research can be a good starting point to assess the internal conditions of glaciers, the transition from cold or temperate ice to a warmer type and, if integrated with the aforementioned techniques, the whole characterization of the ice body can be reached.

References

Abdulrazzaq, Z., Thabit, J., & Al- Khafaji, A. (2021). Performance of GPR attribute analysis to detect and characterise buried archaeological targets near Ukhaidir palace, Iraq. *Bollettino di Geofisica Teorica ed Applicata*, *62*, 159–172. https://doi.org/10.4430/bgta0338

Baker, G., Jordan, T., & Pardy, J. (2007). An introduction to ground penetrating radar (GPR). In *Special Paper of the Geological Society of America* (Vol. 432, pp. 1–18). https://doi.org/10.1130/2007.2432(01)

Barnes, A. E. (1993). Instantaneous spectral bandwidth and dominant frequency with applications to seismic reflection data. *GEOPHYSICS 58*, 419–428.

Björnsson, H., Gjessing, Y., Hamran, S.-E., Hagen, J. O., LiestøL, O., Pálsson, F., & Erlingsson, B. (1996). The thermal regime of sub-polar glaciers mapped by multi-frequency radio-echo sounding. *Journal of Glaciology*, *42*(140), 23–32. Cambridge Core. https://doi.org/10.3189/S0022143000030495

Calmanti, S., Motta, L., Turco, M., & Provenzale, A. (2007). Impact of climate variability on Alpine glaciers in northwestern Italy. *International Journal of Climatology*, *27*, 2041–2053. https://doi.org/10.1002/joc.1500

Church, G., Bauder, A., Grab, M., & Maurer, H. (2021). *Ground-penetrating radar imaging reveals glacier's drainage network in 3D*. https://doi.org/10.5194/tc-2021-82

Cohen, L., & Lee, C. (1990). Instantaneous bandwidth for signals and spectrogram. *International Conference on Acoustics, Speech, and Signal Processing*, 2451–2454 vol.5. https://doi.org/10.1109/ICASSP.1990.116086

Colombo, N., Bocchiola, D., Martin, M., Confortola, G., Salerno, F., Godone, D., D'Amico, M. E., & Freppaz, M. (2019). High export of nitrogen and dissolved organic carbon from an Alpine glacier (Indren Glacier, NW Italian Alps). *Aquatic Sciences*, *81*(4), 74. https://doi.org/10.1007/s00027-019-0670-z

Colombo, N., Bocchiola, D., Said-Pullicino, D., Martin, M., Salerno, F., Confortola, G., Godone, D., D'Amico, M. E., & Vione, D. (2020). The Indren Glacier and the hydrochemical characteristics of its meltwater. *GHIACCI catalogo interno monte rosa bard*, *9*.

Fedele, P. (s.d.). Ghiacciaio. In *Grande Dizionario Enciclopedico: Vol. VIII* (Terza). UTET.

Fediuk, A., Wunderlich, T., Wilken, D., & Rabbel, W. (2022). Ground Penetrating Radar Measurements in Shallow Water Environments—A Case Study. *Remote Sensing*, *14*(15). https://doi.org/10.3390/rs14153659

Feng, X., Sato, M., Zhang, Y., Liu, C., Shi, F., & Zhao, Y. (2009). CMP Antenna Array GPR and Signal-to-Clutter Ratio Improvement. *Geoscience and Remote Sensing Letters, IEEE*, *6*, 23–27. https://doi.org/10.1109/LGRS.2008.2006634

Forte, E., Pipan, M., Casabianca, D., Di Cuia, R., & Riva, A. (2012). Imaging and characterization of a carbonate hydrocarbon reservoir analogue using GPR attributes. *Recent, Relevant and Advanced GPR Studies in Applied Geophysics*, *81*, 76–87. https://doi.org/10.1016/j.jappgeo.2011.09.009

Forte, E., Santin, I., Colucci, R., Dossi, M., Guglielmin, M., Pipan, M., Roncoroni, G., & Žebre, M. (2020). *GPR data analysis for cold and warm ice detection and characterization in polythermal glaciers*. https://doi.org/10.1190/gpr2020-019.1

Forte, E., Santin, I., Ponti, S., Colucci, R. R., Gutgesell, P., & Guglielmin, M. (2021). New insights in glaciers characterization by differential diagnosis integrating GPR and remote sensing techniques: A case study for the Eastern Gran Zebrù glacier (Central Alps). *Remote Sensing of Environment*, *267*, 112715. https://doi.org/10.1016/j.rse.2021.112715

Godio, A. (2017). Crio-Geofisica. *Gruppo Nazionale di Geofisica della Terra Solida*, *Lectiones Magistrales*.

Godio, A., & Franco, D. (2024, luglio). *Indagini georadar ghiacciaio Rutor*. Politecnico di Torino -DIATI.

Gutgesell & Forte. (2024). Integrated GPR attribute analysis for improved thermal structure characterisation of polythermal glaciers. *Bulletin of Geophysics and Oceanography*, *65–2*, 257–270. https://doi.org/10.4430/bgo00439

Maggioni, M., Freppaz, M., Piccini, P., Williams, M. W., & Zanini, E. (2009). Snow Cover Effects on Glacier Ice Surface Temperature. *Arctic, Antarctic, and Alpine Research*, *41*(3), 323–329. https://doi.org/10.1657/1938-4246-41.3.323

Messmer, J., & Groos, A. R. (2024). A low-cost and open-source approach for supraglacial debris thickness mapping using UAV-based infrared thermography. *The Cryosphere*, *18*(2), 719–746. https://doi.org/10.5194/tc-18-719-2024

Molron, J., Linde, N., Ludovic, B., Selroos, J.-O., Darcel, C., & Davy, P. (2020). Which fractures are imaged with Ground Penetrating Radar? Results from an experiment in the

Äspö Hardrock Laboratory, Sweden. *Engineering Geology*, *273*, 105674. https://doi.org/10.1016/j.enggeo.2020.105674

Orombelli, G. (2005). Il ghiacciaio del Ruitor (Valle d'Aosta) nella piccola Età Glaciale. *Geogr. Fis. Dinam. Quat.*, *Suppl. 7*, 239–251.

Pettersson, R. (2005). Frequency dependence of scattering from the cold-temperate transition surface in a polythermal glacier. *Radio Science*, *40*(3). https://doi.org/10.1029/2004RS003090

Santin, I., Forte, E., Nicora, M., Ponti, S., & Guglielmin, M. (2023). Where does a glacier end? Integrated geophysical, geomorphological and photogrammetric measurements to image geometry and ice facies distribution. *CATENA*, *225*, 107016. https://doi.org/10.1016/j.catena.2023.107016

Smiraglia, C., Azzoni, R. S., D'Agata, C., Maragno, D., Fugazza, D., & Diolaiuti, G. A. (2015). The evolution of the Italian glaciers from the previous data base to the New Italian Inventory. Preliminary considerations and results. *Geografia Fisica e Dinamica Quaternaria*, *38 No. 1*, 79–87. https://doi.org/10.4461/GFDQ.2015.38.08

Subrahmanyam, D., & Rao, P. H. (s.d.). *Seismic Attributes-A Review*. https://api.semanticscholar.org/CorpusID:520208

Tabbagh, A., Camerlynck, C., & Cosenza, P. (2013). Numerical modeling for investigating the physical meaning of the relationship between relative dielectric permittivity and water content of soils. *Water Resources Research*, *36*, 2771–2776. https://doi.org/10.1029/2000WR900181

Tognetto, F., Perotti, L., Viani, C., Colombo, N., & Giardino, M. (2021). Geomorphology and geosystem services of the Indren-Cimalegna area (Monte Rosa massif—Western Italian Alps). *Journal of maps*, *17*(2), 161–172.

Topp, G. C., Davis, J. L., & Annan, A. P. (1980). Electromagnetic determination of soil water content: Measurements in coaxial transmission lines. *Water Resources Research*, *16*(3), 574–582. https://doi.org/10.1029/WR016i003p00574

Vergnano, A., Oggeri, C., & Godio, A. (2023). Geophysical-geotechnical methodology for assessing the spatial distribution of glacio-lacustrine sediments: The case history of Lake Seracchi. *Earth surface processes and landforms*, *48.7*, 1374–1397. https://doi.org/10.1002/esp.5555

Viani, C., Machguth, H., Huggel, C., Godio, A., Franco, D., Perotti, L., & Giardino, M. (2020). Potential future lakes from continued glacier shrinkage in the Aosta Valley Region (Western Alps, Italy). *Geomorphology*, *355*. https://doi.org/10.1016/j.geomorph.2020.107068

Zhao, W., Forte, E., Colucci, R. R., & Pipan, M. (2016). High-resolution glacier imaging and characterization by means of GPR attribute analysis. *Geophysical Journal International*, *206*(2), 1366–1374. https://doi.org/10.1093/gji/ggw208

Zhao, W., Forte, E., Pipan, M., & Tian, G. (2013). Ground Penetrating Radar (GPR) attribute analysis for archaeological prospection. *Journal of Applied Geophysics*, *97*, 107–117. https://doi.org/10.1016/j.jappgeo.2013.04.010

Online References

[1] [Online]. Available: https://www.usgs.gov/faqs/what-glacier?qt-news_science_products=0&page=1 [Accessed 2025].

[2] [Online]. Available: https://m3.ti.ch/DFE/DR/USTAT/allegati/articolo/1301dss_2006-2_2.pdf [Accessed 2025].

[3] [Online]. Available: https://nsidc.org/data/glacier_inventory/ [Accessed 2025].

[4] [Online]. Available: https://www.lwpetersen.com/definitions/glaciers/crevasse-glacier/ [Accessed 2025].

[5] [Online]. Available: https://www.antarcticglaciers.org/glacier-processes/mass-balance/ [Accessed 2025].

[6] [Online]. Available: https://academistan.com/glacier-definition-types-and-glaciated-areas/ [Accessed 2025].

[7] [Online]. Available: https://climate.copernicus.eu/climate-indicators/glaciers [Accessed 2025].

[8] [Online]. Available: https://climate.copernicus.eu/esotc/2023/snow-and-glaciers [Accessed 2025].

[9] [Online]. Available: https://archive.ipcc.ch/ipccreports/tar/wg2/index.php?idp=174 [Accessed 2025].

[10] [Online]. Available: http://catastoghiacciai.partout.it/progetto [Accessed 2025].

[11] [Online]. Available: https://www.regione.vda.it/gestione/riviweb/templates/aspx/environnement.aspx?pkArt=1017 [Accessed 2025].

[12] [Online]. Available: http://catastoghiacciai.partout.it/ghiacciai [Accessed 2025].

[13] [Online]. Available: http://catastoghiacciai.partout.it/GeoGhiacciai [Accessed 2025].

[14] [Online]. Available: http://catastoghiacciai.partout.it/ice/bd_attuale [Accessed 2024].

[15] [Online]. Available: https://www.snpambiente.it/snpa/arpa-valle-daosta/ghiacciai-valdostani-ancora-bilancio-di-massa-negativo-per-timorion-e-rutor-al-termine-dellanno-idrologico-2022-23/ [Accessed 2024].

[16] [Online]. Available: https://www.sciencedirect.com/topics/materials-science/ground-penetrating-radar [Accessed 2025].

[17] [Online]. Available: https://www.sensoft.ca/ground-penetrating-radar/military-and-security/ [Accessed 2025].

[18] [Online]. Available: https://www.sciencedirect.com/science/article/abs/pii/S0012825204000054 [Accessed 2025].

[19] S. Burba. [Online]. Available: https://aineva.it/wp-content/uploads/Pubblicazioni/Rivista68/nv68_6.pdf [Accessed 2025].

[20] [Online]. Available: https://www.epa.gov/environmental-geophysics/waterborne-ground-penetrating-radar [Accessed 2024].

[21] [Online]. Available: https://wiki.aapg.org/Seismic_attributes [Accessed 2024].

[22] [Online]. Available: https://www.sciencedirect.com/topics/computer-science/instantaneous-frequency [Accessed 2024].

[23] [Online]. Available: https://wiki.seg.org/wiki/Dictionary:Instantaneous_frequency [Accessed 2024].

[24] [Online]. Available: https://www.sottozerovda.it/glossario/ [Accessed 2024].

[25] [Online]. Available: https://nsidc.org/learn/cryosphere-glossary/dead-ice [Accessed 2024].

[26] [Online]. Available: https://archive.ipcc.ch/ipccreports/tar/wg2/index.php?idp=174 [Accessed 2025].

[27] [Online]. Available: https://link.springer.com/referenceworkentry/10.1007/978-90-481-2642-2_140 [Accessed 2025].

8 Appendix

Codes implemented in the Matlab environment for the attributes assessment.

```
clear all
close all
clc

[filename, pathname]=uigetfile('*.mat'); % processed file selection
cd(pathname)

load(filename)
savename=[filename(1:end-4)];   %to save the results

% Load colorscale for radargram visualization
load('GPRcmap.mat')

%% Plot the processed radargram on which you want to perform the
compututation of the attributes

%Input data after processing:
% xnew = distances along the profile (m);
% z = depth (m);
% rdrg = reflection amplitude matrix, obtained after processing

figure (1)
imagesc(xnew,z,rdrg);
hold on
title('Reflection Amplitude');
xlabel('Distance [m]')
ylabel('Depth [m]')
set(gca,'XAxisLocation','top')
grid
S=size(rdrg);
m=mean(reshape(rdrg,S(1,1)*S(1,2),1));
sd=std(reshape(rdrg,S(1)*S(2),1));
colormap(cmap);
caxis([m-sd m+sd])

%% ATTRIBUTE ANALYSIS
rdrg=rdrg-mean(rdrg); %demean the matrix of reflection amplitudes

%% INSTANTANEOUS AMPLITUDE
rdrgh=hilbert(rdrg);
inst_A=abs(rdrgh); %demean (for instant phase)

figure (2)
imagesc(xnew,z,inst_A);
title('Istantaneous Amplitude');
xlabel('Distance [m]')
ylabel('Depth [m]')
set(gca,'XAxisLocation','top')
colormap(flipud(hot));
caxis([0 1])
grid
saveas(gcf,[savename '_istA.fig'])
```

```
saveas(gcf,[savename '_istA.jpg'])

%% INSTANTANEOUS PHASE

%Preliminary step before computing the cosine of instantaneous phase
attribute

for i=1:length(rdrgh(1,:))
inst_phase(:,i)=(angle(rdrgh(:,i)));
end

figure (3)
imagesc(xnew,z,inst_phase);
title('Instantaneous Phase');
xlabel('Distance [m]')
ylabel('Depth [m]')
set(gca,'XAxisLocation','top')
load('GPRcmap.mat')
colormap(cmap);
grid
saveas(gcf,[savename '_istPhi.fig'])
saveas(gcf,[savename '_istPhi.jpg'])

%% COSINE OF INSTANTANEOUS PHASE
cos_inst_phase=cos(inst_phase);

figure (4)
imagesc(xnew,z,cos_inst_phase);
title('Cosine of Instantaneous Phase');
xlabel('Distance [m]')
ylabel('Depth [m]')
set(gca,'XAxisLocation','top')
colormap(cmap);
caxis([-1 1])
grid
saveas(gcf,[savename '_cosistPhi.fig'])
saveas(gcf,[savename '_cosistPhi.jpg'])

%% INSTANTANEOUS FREQUENCY

%Preliminary step before computing the instantaneous bandwidth attribute
(option 1)

% derivative of the instantaneous phase with respect to time
inst_frequency = diff(inst_phase,1,1) / (2 * pi * dt);
inst_frequency(end+1,:)=inst_frequency(end,:);
%inst_frequency_n=inst_frequency/max(inst_frequency); % for visualization [-1
1]

figure (5)
imagesc(xnew,z,inst_frequency);
title('Instantaneous Frequency');
xlabel('Distance [m]')
ylabel('Depth [m]')
set(gca,'XAxisLocation','top')

colormap(jet);
```

```
caxis([1.5E8 3.5E8])
grid
saveas(gcf,[savename '_instFreq.fig'])
saveas(gcf,[savename '_instFreq.jpg'])

%% INSTANTANEOUS BANDWIDTH

% formula with instantaneous amplitude
dinst_A=(diff(inst_A)/dt);
dinst_A = [dinst_A; zeros(1, size(dinst_A, 2))];
inst_bandwidthA= abs(dinst_A)./inst_A;

figure (6)
imagesc(xnew,z,inst_bandwidthA);
title('Instantaneous Bandwidth');
xlabel('Distance [m]')
ylabel('Depth [m]')
set(gca,'XAxisLocation','top')
grid
colormap((jet));
caxis([0 3E8])
saveas(gcf,[savename '_instBandwA.fig'])
saveas(gcf,[savename '_instBandwA.jpg'])

% formula with instantaneous frequency
inst_bandwidth = abs(diff(inst_frequency,1,1)/dt);
inst_bandwidth = [inst_bandwidth; inst_bandwidth(end,:)]; %padding to match
the size of the other matrices

figure (7)
imagesc(xnew,z,inst_bandwidth);
title('Instantaneous Bandwidth');
xlabel('Distance [m]')
ylabel('Depth [m]')
set(gca,'XAxisLocation','top')
grid
colormap((jet));
caxis([0 1E17])
saveas(gcf,[savename '_instBandw.fig'])
saveas(gcf,[savename '_instBandw.jpg'])

%% SWEETNESS
sweetness_ia=inst_A./sqrt(abs(inst_frequency));

figure (8)
imagesc(xnew,z,sweetness_ia);
title('Sweetness IA');
xlabel('Distance [m]')
ylabel('Depth [m]')
set(gca,'XAxisLocation','top')
colormap(cmap);
grid
caxis([0.00001 0.00008])
saveas(gcf,[savename '_SweetIA.fig'])
saveas(gcf,[savename '_SweetIA.jpg'])
```

```
%% DOMINANT FREQUENCY

[n_traces, n_time] = size(rdrg); % dim del radargram

%Moving window
length_window = 18;
window_step = 1;

% Sampling
Fs = 1/dt; % Sampling frequency (Hz)
freq = (0:length_window/2) * (Fs / length_window); % Frequency axis

dominant_frequency = zeros(n_traces, floor((n_time - length_window) /
window_step) + 1);

for trace = 1:n_traces
    index = 1; % Number of moving windows
    % On each window:
    for start = 1:window_step:(n_time - length_window)
        % Current window
        section = rdrg(trace, start:start + length_window - 1);

        % FFT
        spectrum = fft(section);
        spectrum = abs(spectrum(1:length_window/2+1)); % Half-positive
spectrum

        % Dominant frequency:
        [~, max_i] = max(spectrum); % Index with maximum value
        dominant_frequency(trace, index) = freq(max_i); % Dominant frequency
allocation

        index = index + 1;
    end
end

figure (9)
imagesc(xnew,z,dominant_frequency);
title('Dominant frequency');
xlabel('Distance [m]')
ylabel('Depth [m]')
set(gca,'XAxisLocation','top')
colormap(flipud(spring));
caxis([0 1200000])
grid

saveas(gcf,[savename '_dominant_frequency.fig'])
saveas(gcf,[savename '_dominant_frequency.jpg'])

%% TIME DERIVATIVE OF INSTANTANEOUS AMPLITUDE
time_derIA=diff(inst_A)/(1/Fs); %1/Fs=dt

figure (10)
imagesc(xnew,z,time_derIA);
title('Time derivative of instantaneous amplitude');
xlabel('Distance [m]')
ylabel('Depth [m]')
```

```
set(gca,'XAxisLocation','top')
colormap(flipud(gray));
caxis([0 1])
grid

saveas(gcf,[savename '_time_derIA.fig'])
saveas(gcf,[savename '_time_derIA.jpg'])
```